UNIVERSITY OF CALIFORNIA

Santa Barbara

The Structural and Physical Components Affecting the Mechanics of Composite Mussel Byssus Fibers

A dissertation submitted in partial satisfaction of the

requirements for the degree Doctor of Philosophy

in Mechanical Engineering

by

Marcela Areyano

Committee in charge:

Professor Robert M. McMeeking, Co-Chair

Professor J. Herbert Waite, Co-Chair

Professor Samantha Daly

Professor Beth Pruitt

December 2021

The dissertation of Marcela Areyano is approved

_____

Samantha Daly

_____

Beth Pruitt

_____

J. Herbert Waite, Committee Co-Chair

_____

Robert M. McMeeking, Committee Chair

November 2021

The Structural and Physical Components Affecting the Mechanics of Composite Mussel Byssus Fibers

Marcela Areyano

Para

Mi mama por todo su amor y su apoyo,

Mi hermana por su fe en mi,

La familia Lopez por creer en mi,

and my ancestors who guided me and paved the way for me to get here.

ACKNOWLEDGEMENTS

They say it takes a village to raise a child, and I think the same can be said for getting someone through a PhD program. I want to express my most sincere gratitude to all those who helped me get to where I am today. Words can't express how thankful I am to my advisers Robert (Bob) M. McMeeking, and J. Herbert (Herb) Waite for taking me on as a graduate student so late in my PhD. I was extremely lucky to take all my mechanics courses from Bob, and to have countless meetings in which we discussed mechanics and filled pages of legal pads dissecting my research projects. I am also grateful for all the meetings I had with Herb in which he taught me about the beauty in fundamental science. It was through these two mentors that I was able to find my love for science, something I once thought I lost.

I want to acknowledge several programs that propelled me at various stages in my career and in one way or another helped me obtain my PhD. EAOP was essential to getting me into college, a special shout out to Rosa Martinez for always encouraging me. During my undergraduate and even through my PhD I had unconditional support from the UCSB MESA program. I am especially thankful to Phyllis Brady for being a great mentor and an even better friend. I also thank Mario Castellanos for always pushing me to not give up. I want to thank CSEP and all the CSEP ladies especially Ofi Aguirre-Paden, Stephanie Mendes & Arica Lubin. They supported me in my darkest hours when I was nearly ready to drop out of graduate school and provided me with resources, I need to be successful. I also thank Professor Javier Read De Alaniz, for being a role model for students like myself. I also gratefully acknowledge the funding of the LSAMP Bridge to the Doctorate Fellowship.

This research would not have been possible without the outstanding support of UCSB engineering, staff, and technical assistance. Thank you, Professor Frederic Gibou for seeing something in me as an undergraduate and writing me endless letters of recommendations, you were truly essential for my journey. I also want to thank Assistant Dean Glenn Beltz. Thank you, Dave Bothman and Kirk Fields for the technical support you provided over the years. Thank you, Laura Reynolds for guiding me through this process and all the endless paperwork.

Thank you to the Waite lab for all your support I had a great time being part of this team. Special thanks to Eric Valois for mentoring me, Ismael Carbajal for being an amazing undergraduate researcher. I also want to thank Billy Wonderly and Dariya Ignatenko for their support during the last year. I also want to thank Professor Jamie A. Booth for being a great colleague and mentor. I also thank Professor Attila Kossa for being a great collaborator.

I would like to thank my office mates (aka the finer things club) Julia Zuo , Azi Jackson, and Evan Plunkett for supporting me through the years. Thank you, Julia for all the long walks and all the food you have fed me. Thank you Azi for spending time with me outside the office and listening to me when I needed to vent. Evan, thank you so much for the tips and recommendations on how to write my dissertation.

I want to thank my SACNAS familia for their support and community. I am extremely lucky to have been a part of the founding group for this organization. Carlos Gomez thank you for always having my back and being supportive no matter the circumstances. Thank you to: Mayela Aldaz Cervantes, Simone Steaward Zack Rengart, Jin Kim, Toby Macias, Roman Aguilera, Lena Capece, Lili Sierra Castillo, Janine Chamorro, Braulio Castillo Villasenor, and

Steven Gomez. Isabella Ramirez, thank you for being part of my journey it has been so fun knowing you and going through part of the process together.

I also want to mention Los Ingenieros, si se pudo y'all! Thank you to all the alumni and current students for cheering me on and mentoring me. I especially want to thank Armando Veloz and Rosi Veloz for always being there for me. Thank you, Raymond Valdes for always believing in me and mentoring me.

I want to thank my friends the Gills for letting me join them on fun adventures. Juanita thank you for being so supportive and being a great role model. Peter Verlangieri thank you for all the dinners and supporting me. Erica, amiga! I'm so happy I got to meet you during graduate school and that we have been able to share this experience together. Thank you to Lupita Davila and Sean Finney for helping me throughout at the years and hosting me in their home during fire season. Pallavi, thank you for always listening to me and traveling with me. Gissela Rosiles, thank you for supporting me from across the world and teaching me about mental health. Aimal Khankhel, thank you for our long walks and pushing me to stay in graduate school and find a new lab. Ricardo Robles (Spam), thank you for being part of the last stretch of my PhD and always feeding me. Ruben, you were my first friend at UCSB, and I am so happy that you were here to witness me complete my PhD (look at how far we have come!). Thank you for always being down to go on adventures with me and providing me with moral support. Daniela thank you to you and your family. It has always been nice to know that I have a family in town that I can run to when things get rough, los quiero mucho. Enrique, I can't thank you enough for being my roommate and truly supporting me through everything. I

am so lucky to have you in my life and I'm grateful for everything you have done for me and my family.

Lastly, but most importantly, I want to thank my family. Quiero agredecerle a mi mama (Josefina Lopez), por su apoyo incondicional. I want to thank my sister, Maria Jose Lopez, for always being there for me. I want to thank my godparents, Rosa Lopez and Juan Luis Lopez. I want to thank my tia Luisa y mis primas Mayra Leon y Veronica Leon. I also want to thank my tio Carlos and tio Arturo. Finally, quiero agadecerle a mi tio Jesus que en paz descanse.

VITA OF MARCELA AREYANO

EDUCATION

Bachelor of Science in Mechanical Engineering, University of California, Santa Barbara, December 2012

Doctor of Philosophy in Mechanical Engineering, University of California, Santa Barbara, December 2021

PROFESSIONAL EMPLOYMENT

2015-2020: **Graduate Teaching Assistant**, Department of Mechanical Engineering, University of California, Santa Barbara

201202016: **Multidiscipline Engineer**, Raytheon, Goleta

PUBLICATIONS

M. Areyano, J. A. Booth, D. Brouwer, L. Gockowski, M. T. Valentine, R. M. McMeeking, "Suction-controlled detachment of mushroom-shaped adhesive structures", ASME Journal of Applied Mechanics, 2020

M. Areyano, Luke Gockowski, Megan T. Valentine, "Geometric control of adhesion inspired by mussel plaque/thread structures", Proceedings Adhesion Society Annual Meeting, San Diego, CA 2018

AWARDS

University of California, Santa Barbara University Award of Distinction, 2021

University of California, Santa Barbara Womxn in Science and Engineering & Karl Storz Imaging Scholarship, 2021

National Science Foundation Bridge to Doctorate Fellowship, 2017-2019

Dixon-Levy Graduate Student Association Service Award, 2016

Society of Hispanics Professional Engineers UCSB Student Chapter Alumna of the Year Award, 2016

FIELDS OF STUDY

Major Field: Solid Mechanics and Material Science, Computational Science and Engineering

Studies in Material Science with Professors Robert M. McMeeking and J. Herbert Waite

PRESENTATIONS

Oral Presentation: "Understanding stress relaxation in marine mussel byssal threads", *Society for Advancement of Chicanos/Hispanics in Science National Conference,* Honolulu, Hawaii, October 2019

Poster Presentation: "Understanding stress relaxation in marine mussel byssal threads", *Gordon Research Conference Science of Adhesion,* South Hadley, Massachusetts**,** July 2019

Oral Presentation: "Investigating the role of geometry on the adhesive strength of mussel inspired structures", *American Physical Society Annual Meeting*, Los Angeles, March 2018

Poster Presentation: "Geometric control of adhesion inspired by mussel plaque/thread structures", *Science of Adhesion Conference,* San Diego, February 2018

Poster Presentation: "Bio-inspiration to Bio-prediction: Understanding mussel/plaque structures", *Gordon Research Conference Science of Adhesion,* South Hadley, Massachusetts**,** July 2017

ABSTRACT

The structural and physical components affecting the mechanics of composite mussel byssus

by

Marcela Areyano

Materials found in nature exhibit remarkable properties allowing natural living systems to survive. An outstanding example of this is the byssus of marine mussels. Mussels utilize byssal threads in the byssus to anchor themselves onto a variety of surfaces and endure the harsh intertidal environment. Byssal threads display a composite microstructure as well as intricate macro-scale architectures. This dissertation presents four studies that address questions regarding byssal thread geometry, physical parameters affecting adhesion, and the relationship between the thread microstructure and mechanical properties.

Mussels utilize a mushroom-shaped geometry for their byssal threads: the threads consist of a distal thread (stalk) terminating in a plaque (mushroom-tip). Previous studies on adhesion associated with the mushroom-shaped geometry have focused on the effects of geometrical parameters such as tip thickness and the ratio of the stalk to tip radius. Mussels deposit byssal threads radially, which are loaded at various angles during wave motion. This introduces a more complex geometry than previously studied in regard to adhesion and detachment. Due to these differences, we focused on the effects of casting angle and loading angle on adhesive strength utilizing synthetic mimics. We find that the optimal configuration for adhesive strength is when the loading angle and casting angle are equivalent.

Evidence suggests that suction may play a role in the adhesive strength of mushroom shaped structures. Using byssal threads as inspiration, we utilized synthetic mimics to study the effects of suction at the macroscopic scale. To determine the critical stress necessary for defect propagation and detachment a fracture mechanics-based model is introduced, and compared with experimental results. The findings indicate that there is a greater increase in adhesive strength due to suction at the macro-scale, which is length-scale dependent.

Lastly, we assess the relationship between the thread microstructure and mechanical properties. Different protein domains in the collagenous core were targeted with chemical treatments and stress relaxation measurements were conducted to determine which energy dissipative mechanisms are present during the relaxation process. This complements previous studies which largely focused on elastic properties, by concentrating on the viscoelastic properties of the threads. Results show that the silk-like domains are largely responsible for energy dissipation via protein unfolding and/or rearrangement during the relaxation process.

Under cyclic loading, distal threads exhibit a stress-strain behavior reminiscent of shapememory and superelastic effects observed in some metal alloys. Previous studies have revealed that distal threads undergo phase transitions in their microstructure as they are loaded. A hyperelastic Neo-Hookean-based model is introduced that incorporates the mechanical properties from two distinct phases in the microstructure to address the contributions from the collagen core. In addition, a Mullins-based model is used to fit the composite cyclic data and provide insight into the mechanical response of the composite thread.

Table of Contents

Chapter 1. Introduction

1.1 A Note on Bioinspiration

Bioinspiration is the engineering lens through which we attempt to mimic what biology has developed over millions of years. The art of biomimicry rooted in bioinspiration has stood the test of time with civilizations across the world using nature as inspiration for developing things such as devices for basic survival skills all the way to architecture. Within the scientific world bioinspiration has led to the creation of new materials, medical solutions, new chemistry among many other functions. Our intrigue for nature has gone as far as using its biomaterials to heal the human body with civilizations such as Mayans discovering the unique property of nacre to flawlessly heal onto living human bone[1]. Using nature as inspiration other Mesoamerican civilizations such as the Aztecs developed and utilized chinampas, which were artificial islands, used for agriculture[2] . Day to day items created as a result of phenomena observed in nature include Velcro which was developed after Swiss electrical engineer George Mestral noticed burdock seeds clung to his woolen socks [3]. Other technological advances inspired by nature include the Japanese Shinkansen bullet train which was designed based on the Kingfishers bird beak [4]. On a similar vein, birds have created the basis for the world's aviation.

Although tempting, jumping from biology straight to applications one must be cautioned that what nature seems to impeccably accomplish can be a rather intricate process. Going directly to application dismisses what biology has taken millions of years to develop. By conducting fundamental research to understand the origins of the mechanisms employed by nature not only does one develop a deeper understanding which can be translated to

applications, but more importantly pays tribute to our natural world. Paying homage to nature is a tradition within many native communities that has in turn led to a more holistic understanding of the natural world and our relation to it[5]. By engaging in such practices through fundamental research we can continue to create a connection with nature while advancing our scientific understanding of biology that can then be translated to applications.

The work presented in this dissertation was conducted in an effort to understand the underlying strategies used in nature, in particular by marine mussels to permanently adhere and remain attached to surfaces. Experiments and modeling were designed utilizing a material science, biochemical, and mechanical engineering framework. First, the physical origins of the mussel adhesion are interrogated via synthetic mimics. Although the interfacial chemistry of the mussel adhesion has been widely studied it is of much importance to understand the physical components to holistically understand the system. The results presented here aim to unravel the effects of geometry and suction on mussel inspired adhesion. Next, mussel biofibers which are essential for mussel survival were characterized to better understand their mechanics. These fibers have been thoroughly studied due to their astonishing mechanical properties. By building on this work, the goal was to improve the existing knowledge of the fibers tactics for dissipating energy. The hope is that the findings presented in this work can lay the foundation for future applications inspired by mussels. A detailed account of results will be presented in the chapters that follow.

1.2 A structure worth mimicking: the mussel byssus

Figure 1.1: View of a colony of marine mussels, Mytilus Californianus, securely attached to rocks in the intertidal zone at the University of California Santa Barbara campus point. Commonly referred to as ecosystems engineers' mussels can filter 10-20 liters of water per day and create habitat for other organisms.

For mussels to survive the harsh environment of the intertidal zone they must remain securely attached to surfaces such as rocks, despite constant loading from waves and predator encounters (Figure 1.1). To endure such harsh environments mussels' secret bundles of biofibers (threads) with plaques at the ends known as byssus (Figure 1.2) [6,7]. For centuries the mussel byssus has been of great interest due to their tenacious attachments. In the fifteenth century Theodorus Gaza a humanist and translator of Aristotle first translated Aristotle's passage on Pinnna [8]. "On a sandy and muddy sites the Pinna-mussels grow (come forth) upright from the byssus, that is this the hair tuft or Pinna-wool[8]." Thus, first using the term byssus to describe the mussel secreted biofibers. Later work by Heide in the 17th century described the threads to be plants[9]. During the last 7 decades many scientific articles have been published aimed at dissecting the underlying strategies for mussel byssus tenacity[10].

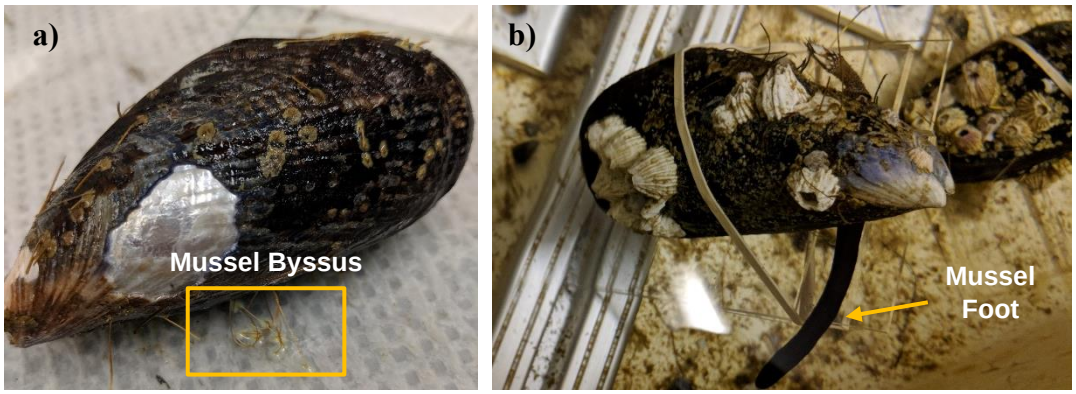

Figure 1.2: Pictures of two different mussels both species Mytilus Californianus. a) Highlighted by the box are byssus used to attach the mussel to the glass substrate, byssus are fabricated and deposited individually radially as to anchor the mussel. b) Highlighted by the arrow is the mussel foot which is used for producing byssus via a process closely resembling injection molding.

The byssus is composed of a bundle of threads with lengths ranging between 2-6cm in adult mussels. Individual threads known as byssal threads are made up of three main components: I) the proximal thread, II) the distal thread, & III) the adhesive plaque. Mussels fabricate these proteinaceous threads in a process closely resembling that of 3D printing. Individual threads are quickly printed with production times of 30 seconds to 8 minutes[11]. To produce a new thread mussels will stick their foot out from their shells, a special organ dedicated to the production of threads, and feel around for an optimal surface to adhere onto (Figure 1.2). Threads are formed via injection molding of liquid collagenous crystals in the ventral groove which runs along the length of the foot among other protein precursors[10,12–14] (Figure 1.3). First, plaque proteins starting with those at the end between the foot tip and the substrate are deposited. Next, the bulk of the plaque and thread core components are deposited[15,16]. Before the proteinaceous structures are released from the groove they are coated by a thin layer (~5 μm in thickness) known as the cuticle that shields the thread from environmental exposure. This outer cuticle is composed of a stiff matrix embedded with soft granules (Figure 1.3)[17,18]. Upon release the threads are immediately recruited into load-bearing.

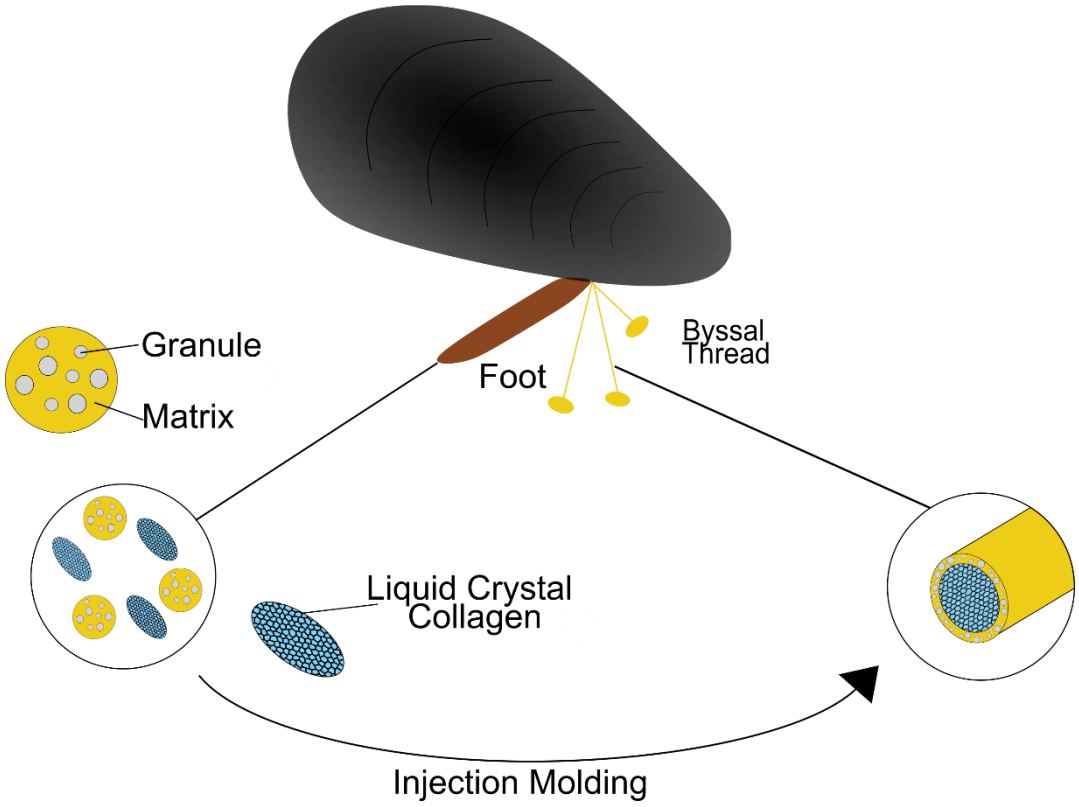

Figure 1.3: Representative diagram showing the production of individual byssal threads. Threads are formed through a process closely resembling that of injection molding. Time of fabrication for individual threads ranges between 30 seconds to 8 minutes. The protein precursors used for producing threads are synthesized and stored in the mussel foot.

Byssal threads have been of great interest in the scientific community due to their superb adhesion and resilience in the presence of constant loading from waves (Figure 1.4)[10,14,19–29]. Mussels can deposit byssal threads and adhere themselves to virtually any solid surface in a turbulent saline environment. It is crucial to recognize that water poses significant challenges to adhesive bonding. For this reason, the plaque in particular has served as inspiration for many adhesives and coatings[25]. Much of this work has focused on replicating or utilizing the 3,4-dihydroxyphenylalanine (DOPA) adhesive protein which is abundant at the plaque-substrate interface[25,30]. Beyond the plaque interfacial chemistry, it is important to recognize the physical components that could contribute to mussel adhesion[19,28,31]. In byssal thread structures a common contact geometry is observed: mushroom-shaped geometry. This geometry consists of a thin stalk terminating in a circular thin plate (mushroom tip), in the mussel structures the thread serves as the stalk while the plaque serves as the mushroom tip (Figure 1.4). It has been well documented that the geometry of contact element is crucial to adhesion, and this type of geometry has shown to be superb. Adhesive systems exploiting the mushroom-shaped geometry can be observed across various organisms and environments[32–34]. These systems range from plants such as the vine plant *Parthenocissus* which use this geometry to permanently adhere its tendrils to surfaces, to reptiles like geckos which use this geometry in their adhesive toe pads to rapidly attach and detach from surfaces[35,36]. The employment of such geometry by mussels suggest that this too could be one of the factors in the tenacious attachment of byssal threads.

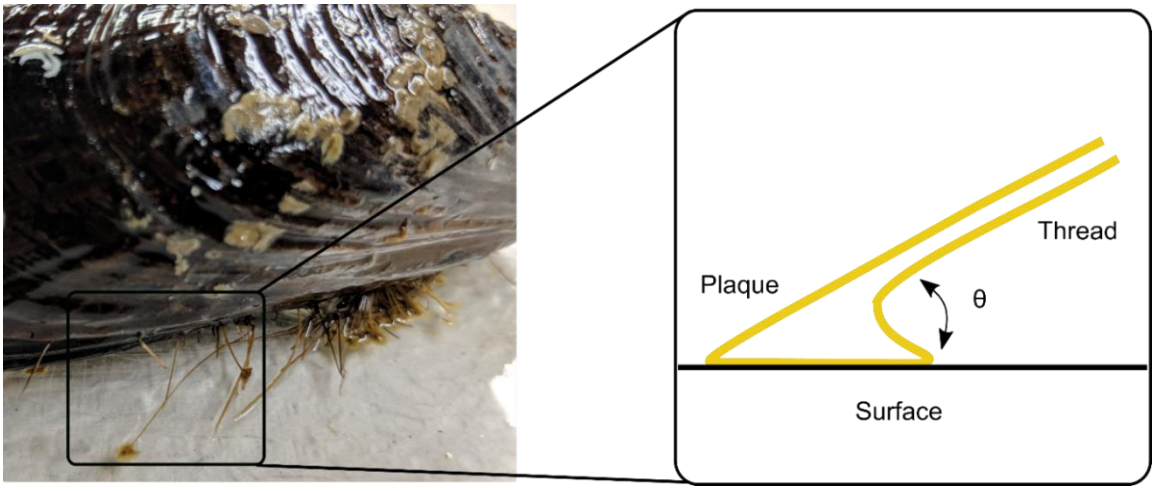

Figure 1.4: Pictured on the left is a byssal thread deposited by a *Mytilus Californianus.* Byssal threads exhibit a mushroom-shaped type adhesion observed across many other biological systems. Byssal threads are deposited radially at various angles.

Following the mussel plaque is the thread itself, a highly extensible fiber that is divided into the proximal and distal regions. The distal region of the thread is furthest from the mussel and terminates in the plaque. The threads are typically 2-5 cm in length with diameters ranging between 100-200 μm, with the distal region making up ~80% of the total thread length[19]. The distal region is known for its high extensibility, high hysteresis (energy dissipation), high stiffness and ability to mechanically heal after undergoing deformation[19,37,38]. When compared to the distal region the proximal regions is less stiff, and twice as extensible[19]. The two thread mechanical properties are displayed in table 1[19].

Table 1.1: Mechanical properties of Mytilus Californianus byssal threads, properties are divided into distal and proximal regions of the thread.

Material	Modulus (GPa)	Strength (GPa)	Extensibility (%)	Hysteresis (%)	Toughness (MJ/m^{-3})
Distal thread (*M. Californianus*)	0.87	0.075	109	72	45
Proximal thread (*M. Californianus*)	0.016	0.035	200	47	35

Encapsulating the byssus is a stiff cuticle with a thickness of roughly 5 µm possessing self -healing properties [39]. The cuticle is composed of a stiff amorphous matrix embedded with soft granules presumably made of condensed mussel foot protein 1 (mfp-1)[17,40–42]. This thin shell serves as a protective layer for the proteinaceous thread from the harsh intertidal zone. This component exhibits a hardness six times greater than that the core in a hydrated state[41]. The large mechanical mismatch between the core and shell is believed to be mitigated via a thiol-rich interlayer[42]. Previous work by Holten-Andersen et. al demonstrated that byssal threads with cuticle possessing granular structures enable breaking strains twice that of cuticles with no granules[18]. Such findings indicate the cuticle plays a big role in both protecting the core and the thread overall mechanics.

With individual byssus components showing such high quality chemical and mechanical properties it is no wonder these structures have been of immense interest for hundreds of years. The curiosity with which the mussel byssus have been studied has led to

many advancements in material science[25,43–49]. Although much has been learned in regards to the biochemistry and mechanics of the byssus much is yet to be understood. For this reason, the mussel byssus continues to be of great interest.

1.3 Mushroom-Shaped Adhesion in Mussel Byssus

Mussels on average will have 50-100 byssal threads that are deposited radially outwards, anchoring the mussel to surfaces[19,31]. In this configuration mussels must withstand upward loading and drag from both wave motion and predator encounters. It has been reported that a *Mytilus californianus* adhered to a rock can experience loads of 300 N in normal loading (lift) and 180 N in shear loading (drag)[31,37] (Figure 1.5). If one assumes the threads count ranges between 50-100 the load experienced by individual threads can range between 6N and 3N in normal loading. It has been observed that the most common point of failure in these field tests occurred at the adhesive plaques. However, it has also been observed that depending on the angle at which individual threads are tested (pulled) the failure mechanisms (i.e. cohesive vs. adhesive) and failure loads can vary drastically[26,50]. Given the discrepancy in previous studies and looking beyond the interfacial chemistry of the plaque it then becomes evident that other physical components such as geometry must play a role in the adhesive properties of byssus. Due to the vast difference from one byssal thread to the next and the contribution from the interfacial chemistry it becomes evident that studying the influences from physical components in natural system can be convoluted[26,27]. For this reason, studying the system in a simpler configuration becomes key. To address this gap the studies presented on this dissertation utilized synthetic mimics inspired mussel byssal threads.

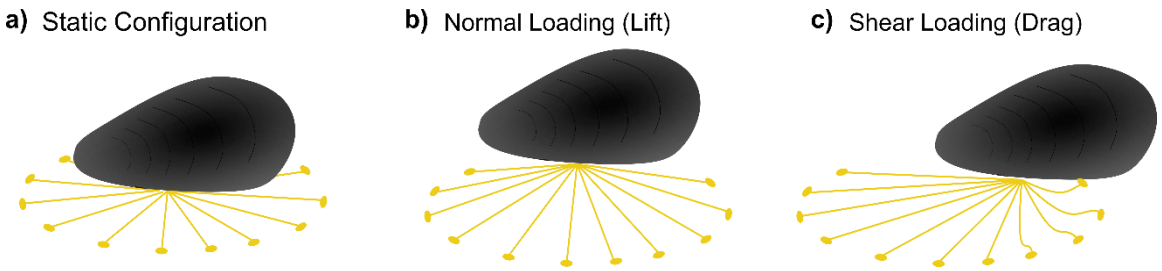

Figure 1.5: Schematics of some of the conditions marine mussels must endure. a) Mussels typically deposit their byssal outward radially in order to adhere onto surfaces, anywhere between 50-100 byssal threads will be deposited by adult mussels. b) Mussels must resist normal loading (lift) while adhered to rocks, during this process byssal threads will be extended. c) Mussels must also withstand shear loading (drag) from being pulled and/or loading from motion waves.

When discussing geometrical effects on mussel inspired adhesion there are several factors that need to be considered. The first component to take into consideration is the mushroom-shaped geometry byssal threads possess. As previously mentioned, this type of geometry is present across many biological systems and has led to many studies. This mushroom-shaped geometry is observed in systems with both permanent and reversible adhesion. A system worth noting which has been widely studied is gecko adhesion[51]. Geckos can rapidly attach and detach from surfaces including vertical and inverted surfaces. This type of adhesion is known as dry adhesion, as it is a transient and doesn't require any kind of surface preparation. Geckos can accomplish this rapid adhesion via the spatula-shaped setae arranged in lamellae on their footpads[36]. The success of this type of adhesion is primarily reliant on

van der Waals interactions[52–54]. Outside of understanding the intermolecular forces at play during adhesion many studies have been dedicated to understanding the mushroom-shaped geometry observed in their setae[36,54–57].

Experimental studies conducted on mushroom-tip bioinspired fibrillar surfaces have revealed that this geometry outperforms other geometries observed in nature including to that of straight punches(cylinder) and spatula tip (Figure 1.6)[58,59]. Additional studies have focused on developing a theoretical framework for understanding the underlying mechanisms for the superiority of mushroom-shaped fibrillar adhesives[55,60,61]. This work has revealed that there is a severe stress concentration at the contact edge of straight punches leading to edge defect propagation causing detachment at low forces. The addition of a mushroom tip reduces the strain energy at the contact edge and creates a turning action producing a compressive contribution to the stress at the edge. Due to this, defect propagation is shifted from the edge to the center leading to higher detachment forces. Through these studies it has become evident that contact geometry plays a crucial role in adhesion whether it be permanent or temporary.

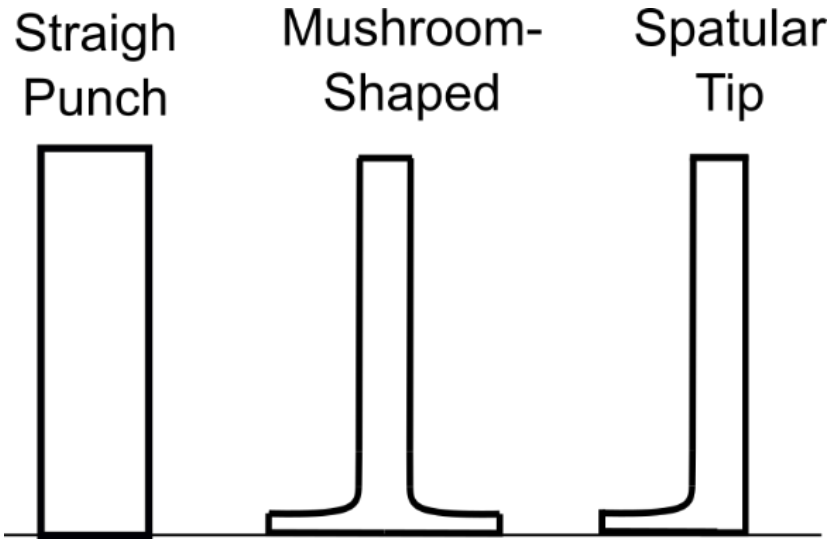

Figure 1.6: Schematic of biologically relevant adhesive structures. These types of geometries are commonly found in many biological systems. Mussels in particular utilize the mushroom-shaped type geometry in their byssus to attach to surfaces. Mushroom-tip geometry outperforms other structures.

The advancements made in this field have led to many bioinspired micropatterned adhesives that have the potential to overcome obstacles encountered by traditional adhesives. In applications where repeatable, reversible and residue free adhesion is required these adhesives show great promise[62]. Micropatterned surfaces using biological relevant geometries have shown to withstand over millions attachment cycles without diminishing the adhesion, as well as the capability to adhere both in air and water[62]. These surfaces have been used in various application including climbing robots and in pick-and-place operations[62–65]. Within the biomedical field adhesives for patching wounded skin have been designed using micropatterned surfaces that are bioinspired and have been successful[66–68] (). Furthermore, engineers at NASA's Jet Propulsion Laboratory in Pasadena, California have designed adhesives inspired by geckos for space applications.

Over the last two decades much has been learned regarding biologically relevant adhesive geometries observed in nature. Despite all these advances there is still much to be learned about the physical origins of mushroom-shaped adhesion. Many of the studies previously mentioned have focused on patterned surfaces, and less on individual structures. Furthermore, these studies have largely been conducted on micron scale pillars. Mussel byssal threads can serve as excellent inspiration for biomimetic structures as they are on the macro scale and are deposited at numerous angles. Byssal threads diameters are on the order of ~ 100 μm and terminate on a plaque with diameters on the order of ~ 1 mm. The distal thread typically terminates near the center of the plaque at angles of ~ 5º - 45º[26] (Desmond). Using mussel byssal threads as inspiration the role of deposit angle (θ) and pull angle (φ) can be explored. Moreover, due to the scale of these biomimetic structures the role of suction can be interrogated

as suction is dependent on volume and area so at larger scales (micron vs. macroscale) suction can be essential for adhesion[69].

1.4 Byssal threads core composition

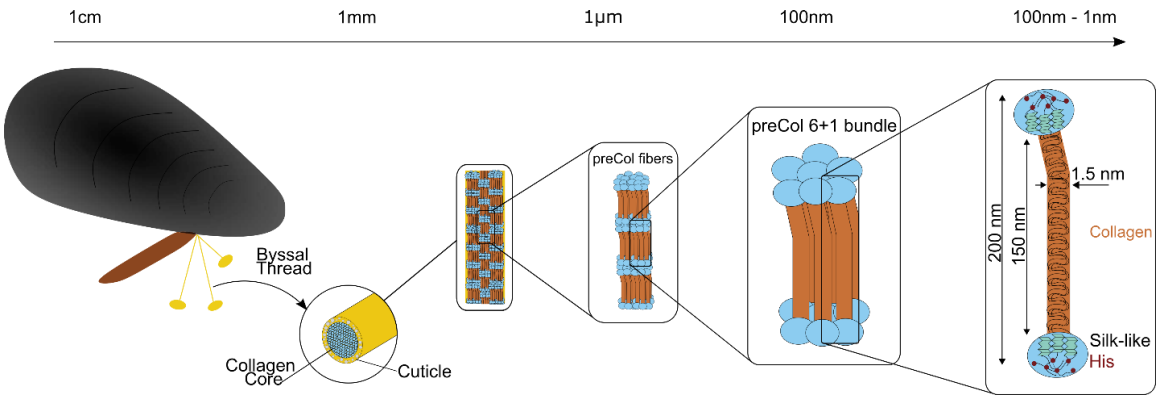

Figure 1.7: The hierarchical assembly of mussel byssal threads spans multiple length scales. Each thread is composed of a collagen core encapsulated by a stiff cuticle. The thread core is comprised of highly ordered collagen fibers made up of preCols arranged in 6+1 bundles. Individual preCols (preCol-D shown here) are composed of a central triple helix collagen, followed by silk-like domains on both ends with His-rich domains terminating the silk-like domains (flanking domains vary for the different preCol's).

Byssal threads are hierarchical structures with their composite structure and function closely related (Figure 1.7). Threads are made up of a collagenous core encapsulated by a stiff cuticle, with the collagen core making up more than 95% of the total composition. To adequately understand the mechanical properties of marine mussel byssal threads one must

first understand their highly ordered central core composition. Individual threads are divided into the proximal and distal regions both exhibiting different mechanical properties[19]. Although possessing different properties both regions of the threads are largely composed of collagen[13,70–72]. Collagens are a large diverse group of proteins with over 25 types identified in vertebrates and additional types appearing in invertebrates[73–75]. Collagen is a structural protein found in all animals serving as a building block for biomaterials such as bone, skin, and tendon[74,75]. The collagen protein structure consists of a triple helix composed of polypeptide chains, called α chains, with Gly-X-Y sequences[76]. The X and Y repeats are frequently proline with the proline in the Y position typically being 4-trans-hydroxylated[77–79]. The α chains form left-handed helices individually, and come together to assemble into a right-handed super helix[76]. The most abundant collagens (I-III) tend to arrange into fibrils that are staggered in bundles serving as load bearing elements for materials such as tendons and ligaments[74]. In a similar manner byssal threads are collagenous fibers with staggered collagen fibrils that serve as load-bearing elements for mussels.

The collagen found in the byssal threads is arranged into bundles known as preCols[13,70–72,80]. There are three distinct preCols that have been identified in *Mytilus edulis* called preCol-D, preCol-NG, and preCol-P with similar preCol variants found in *Mytilus galloprovincialis* and *Mytilus californianus*[70–72,81–83]. Resembling block-copolymers each variant has a central kinked collagen, variable flanking domains and a histidine-rich amino and carboxy termini[13,70–72,81,82] (Figure 1.8). Individual preCols arrange in an ideal hexagonal lattice forming a 6+1 bundle structure (giant bent core, krauss). preCols make up 96% of the total protein content in the distal portion of the thread, and 66% in the proximal

region[71]. Besides having different preCol content the distribution of the preCols varies between the distal and proximal region preCol-D and preCol-P existing in a gradient across both, while preCol-NG is evenly distributed among both regions[80,83].

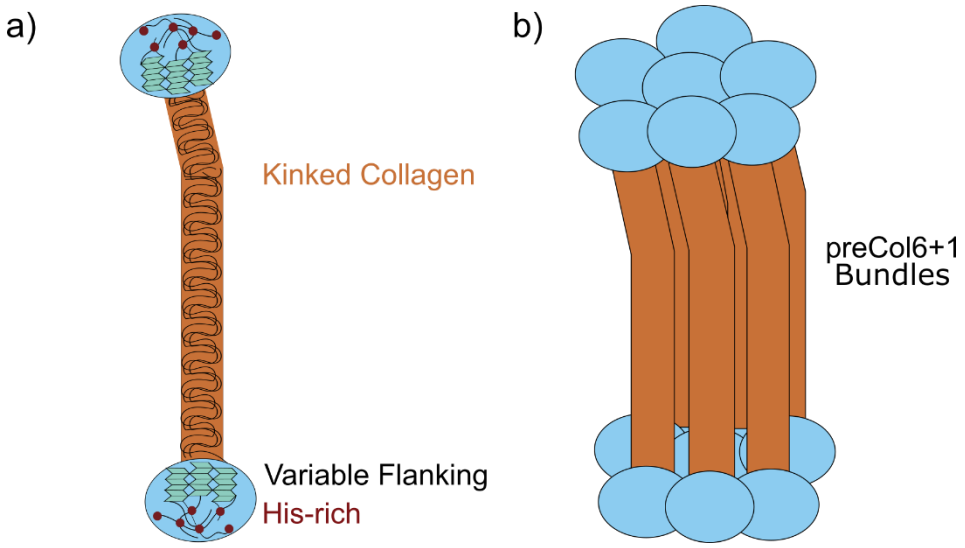

Figure 1.8: Byssal threads are primarily composed of proteins with collagens making up a large portion of the core. a) Individual collagens in the threads are known as preCols and are composed of a central kinked collagen followed by variable flanking region (preCol-D: silk-like, preCol-NG: Gly-rich, preCol-P: elastin-like) and a His-rich domain. b) The preCols are arranged in a 6+1 bundle structure, which staggered throughout the core of the thread.

The kinked collagen domain is the largest domain in the preCols and exhibits 1-5 interruptions in the Gly-X-Y sequence[13,84]. The aberrations in the repeat structure are believed to cause the bend observed in this domain [13,77,84]. Although in many other collagens the proline and hydroxyproline in the X and Y positions serve to stabilize the collagen structure in preCols these residues have been shown to be destabilizing[72,85]. Regardless of this and the alterations to the sequence wide angle X-ray scattering of distal threads show a stable triple helix (Mercer 1952). Adding to this is the byssal threads collagen resistance to pepsin, further indicating the presence of a stable triple helix[80].

Following the collagen domain on both ends are the flanking domains, which vary between the different preCols. preCol-NG, which is evenly distributed between the proximal and distal thread, possesses a Gly-rich flanking domain resembling plant cell wall proteins[82]. preCol-P and preCol-D are distributed in a gradient like manner[83]. preCol-D is abundant in the distal region and decreases axially towards the proximal region, and has a flanking domain that resembles a motif sequence of spider dragline silk[82]. Similarly, preCol-P is abundant in the proximal region and decreases axially as it approaches the distal region and has a flanking region closely resembling elastin[82]. The similarities of the flanking domains to other proteins known for their load-bearing properties leads to the prediction that because of different flanking domains the various preCols have different mechanical properties[84]. Silk proteins are known for their high stiffness suggesting preCol-D would be stiffer than preCol-P as it possess elastin-like motifs which in other systems are known to be highly elastic [77]. preCol-NG is predicted to have properties intermediate to the other preCols.

Terminating the flanking domains are the histidine-rich domains. Histidine residues are characterized by their ability to form reversible coordinate bonds with divalent transition metals such as zinc and copper[86]. Due to this it has been proposed that the histidine-rich termini provide metal binding/cross-linking sites as previous studies have revealed the abundance of Zn, Cu, and Fe in threads[87,88]. Disrupting the his-rich domains via a metal chelator such as EDTA was shown to diminish the mechanical and self-healing properties of byssal threads suggesting that metal dependent crosslinks play an essential role in the mechanical response of threads[38].

The last components observed in the central core are the thread matrix proteins (TMP-1) found in the distal portion and the proximal thread matrix protein (PTMP-1) found in proximal portion of the thread[89,90]. Although the role of these proteins isn't fully understood one proposed hypothesis is that they provide viscoelastic matrix around the collagenous fibers[89] .

As it will be discussed in future chapters the work presented in this thesis is focused on the distal portion of the thread with an emphasis on the effects of the preCols specifically preCol-D on the mechanical properties of byssal threads.

1.5 Byssal Threads Mechanical Properties

Byssal threads are tasked with anchoring and securing mussels to surfaces despite existing in a chaotic environment where wave speed can reach up to 25 m/s[77]. To endure such conditions byssal threads are endowed with extraordinary mechanical properties. Threads can extend more than twice their original length with a strength and modulus comparable with

that of tendon[19,38,91,92]. Accompanied with such a high extensibility is high hysteresis and high toughness suggesting the threads can dissipate large amount of mechanical energy through deformation. Although the distal and proximal threads work together to prevent the mussels from dislodging, they possess mechanically distinct properties. A brief introduction to the proximal thread properties will be presented in this section. However, the focus of the work that will be elaborated on later chapters is on the distal thread.

When discussing mechanical properties of materials, one is often concerned with the materials physical response to being loaded (i.e. pulled, compressed, etc.). Commonly, uniaxial tensile testing is used to characterize the tensile mechanical properties of isotropic materials. During uniaxial testing material samples are extended axially until the material fails. Throughout the process the applied force and elongation of the material are recorded. These data are normalized via the geometry of the material sample. Strain is the normalized extension and is determined using the following equation:

$$\varepsilon = \frac{\Delta L}{L} = \frac{L - L_0}{L} \times 100\% \quad (1)$$

Where L_0 is the original length of the sample, and L is the current length of the specimen. Stress is the normalized form of force and is determined by the following equation:

$$\sigma = \frac{F}{A} \quad (2)$$

Where F is the current tensile force, and A is the nominal cross-section of the sample. Using this normalization, the data can then be graphed into a stress-strain curve. From stress-strain

curves material properties such as elastic modulus, yield strength, toughness, and strength can be determined. A typical stress strain curve for a distal thread is shown in Figure 1.9.

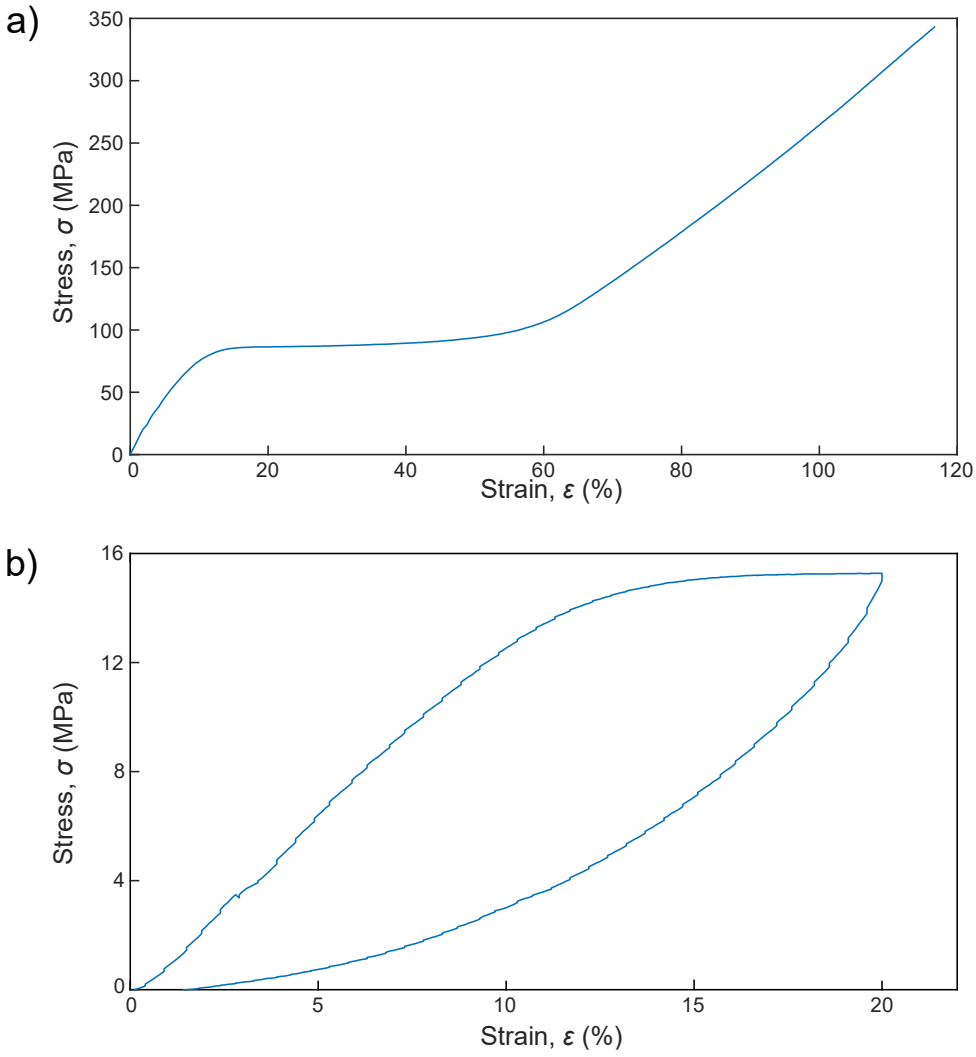

Figure 1.9: Representative curves for mechanical testing of distal threads. a) Typical stress strain curve for a thread that was pulled to failure. b) Hysteresis loop of a thread that was loaded to 20% and unloaded back to a strain of 0%. Results are shown for engineering stress and strain.

Numerous studies have been conducted on the distal threads' mechanical response for various species using stress-strain curves as a tool for characterizing mechanical properties[19,38,92,93]. At low strains ($\varepsilon < 10\%$) the stress-strain relationship is linear and is identified as the elastic regime with the slope of the curve int this regime known as the elastic modulus. In this phase materials behave elastically without any permanent deformation. Distal threads from various specieas have been reported to have elastic modulus ranging between 450 – 850 MPa[37,38,77]. Following this linear regime, where the strain is $10\% < \varepsilon < 20\%$, is a yield like region in which the modulus nearly approaches zero and very little increase in load is necessary to continue extending the thread. At $\varepsilon \sim 50\%$ there is a second linear regime in which the material stiffens, and higher forces are required to increase extension. At $\varepsilon > 100\%$ distal threads will typically fail.

Another tool commonly used to characterize materials is cyclic loading in which materials are loaded to certain strains and unloaded prior to failure, this may be repeated subsequent times up until failure. Using cyclic loading one can capture hysteresis loops and determine how much energy is lost during loading. The yield like region in the stress strain curve reveals that distal threads can dissipate large amounts of energy, likely through deformation and/or internal friction. Hysteresis is a measure of how much energy is lost in a loading and unloading cycle, distal threads have shown a hysteresis of up to 70%, a typical cycle is shown in Figure 1.9[77]. Another indication of distal threads' ability to efficiently deal with energy is their high toughness. Toughness is a measure of the materials ability to absorb energy and permanently deform without fracturing. Distal threads exhibit toughness on the order of ~45 MJ/m^3 which is 7 times higher than that of tendon, another collagen based material

[91,94]. What is more impressive is that these threads can self-heal (recover their mechanical properties) after undergoing permanent deformation despite of entirely being composed of proteins on a time scale of hours[37,38]. For comparison tendon requires cell mediated healing that can take up to months[95].

Although distal threads possess an initial elastic regime, they are highly viscoelastic materials. Viscoelastic materials are materials known to exhibit both viscous (fluid) and elastic (solid) behavior. Viscoelastic materials exhibit hysteresis, stress relaxation, creep, and strain rate dependence. Distal threads exhibit all these properties to varying degrees[37]. Much of the work conducted on threads has lacked a full understanding of the viscoelastic behavior of threads and what viscous processes allow for the efficient energy dissipative mechanism observed. A detailed study of distal threads viscoelastic properties will be presented on, in a later chapter.

Distal threads exhibit a Mullins like behavior, in which upon unloading a softening effect is observed[96–98]. However, the response differs from other Mullins materials in that upon reloading the loading takes place on different curve than the unloading. The reloading modulus is higher than the unloading modulus, indicating there is a recovery in mechanics that occurs on a time scale of seconds. Small Angle X-Ray Scattering have revealed that during mechanical loading the distal thread collagenous core undergoes phase transitions[99,100]. Using these studies as a basis we consider a hyperelastic model which incorporates two distinct phases in the core which contributed to the mechanical response of the thread. A later chapter is dedicated to exploring the phase transitions during cyclic loading and how this explains the Mullins like behavior with a recovery in mechanics that is observed.

Lastly, it is worth noting the contributions from the proximal thread although the focus of later chapters will be on the distal thread. Connecting the distal thread to the mussel is the proximal thread. The proximal region roughly composes 20% of the total thread[19] .This portion of the thread is more extensible than the distal region and exhibits highly elastic properties with no real plateau region[37]. The modulus of the proximal region in *M. Californianus* is ~16 MPa, 50 times less stiff than the distal thread, and can extend up to twice that of distal threads[37]. The proximal and distal region show vastly different mechanical properties and it has been hypothesized that the differences in mechanical properties arise from the difference in flanking domains. The different preCols (NG, D, and P) possess different flanking domains which presumably have distinct mechanical properties leading to the differences in mechanical properties[84]. The distribution of flanking domains is also believed to moderate stress concentration arising from mechanical mismatches between the distal and proximal region[84]. Although both regions possess different properties, together they have excellent properties allowing mussels to survive the hostile intertidal zone.

1.6 References

[1] Westbroek, P., and Marin, F., 1998, "A Marriage of Bone and Nacre," Nature, **392**(6679), pp. 861–862.

[2] Carrasco, D., 2006, "The Oxford Encyclopedia of Mesoamerican Cultures," Digital Resources.

[3] "Who Invented Velcro? | VELCRO® Brand," UK.

[4] Foo, C. T., Omar, B., and Taib, I., 2017, "Shape Optimization of High-Speed Rail by Biomimetic," MATEC Web Conf., **135**, p. 00019.

[5] Kimmerer, R. W., 2015, Braiding Sweetgrass: Indigenous Wisdom, Scientific Knowledge and the Teachings of Plants, Milkweed Editions, Minneapolis, Minn.

[6] Yonge, C. M., 1962, "On The Primitive Significance of the Byssus in the Bivalvia and Its Effects in Evolution," Journal of the Marine Biological Association of the United Kingdom, **42**(1), pp. 113–125.

[7] Denny, M. W., and Gaylord, B., 2010, "Marine Ecomechanics," Annu. Rev. Mar. Sci., **2**(1), pp. 89–114.

[8] Van Der Feen, P. J., 1949, Byssus.

[9] Heide, A. de, 1683, Anatome Mytuli.

[10] Waite, J. H., 2017, "Mussel Adhesion – Essential Footwork," J of Experimental Biology, **220**(4), pp. 517–530.

[11] Rodriguez, N. R. M., Das, S., Kaufman, Y., Israelachvili, J. N., and Waite, J. H., 2015, "Interfacial PH during Mussel Adhesive Plaque Formation," Biofouling, **31**(2), pp. 221–227.

[12] Waite, J. H., 1992, "The Formation of Mussel Byssus: Anatomy of a Natural Manufacturing Process," Structure, Cellular Synthesis and Assembly of Biopolymers, S.T. Case, ed., Springer, Berlin, Heidelberg, pp. 27–54.

[13] Hassenkam, T., Gutsmann, T., Hansma, P., Sagert, J., and Waite, J. H., 2004, "Giant Bent-Core Mesogens in the Thread Forming Process of Marine Mussels," Biomacromolecules, **5**(4), pp. 1351–1355.

[14] Tamarin, A., Lewis, P., and Askey, J., 1976, "The Structure and Formation of the Byssus Attachment Plaque in Mytilus," Journal of Morphology, **149**(2), pp. 199–221.

[15] Yu, J., Wei, W., Danner, E., Ashley, R. K., Israelachvili, J. N., and Waite, J. H., 2011, "Mussel Protein Adhesion Depends on Interprotein Thiol-Mediated Redox Modulation," Nat Chem Biol, **7**(9), pp. 588–590.

[16] Petrone, L., Kumar, A., Sutanto, C. N., Patil, N. J., Kannan, S., Palaniappan, A., Amini, S., Zappone, B., Verma, C., and Miserez, A., 2015, "Mussel Adhesion Is Dictated by Time-Regulated Secretion and Molecular Conformation of Mussel Adhesive Proteins," Nat Commun, **6**(1), p. 8737.

[17] Monnier, C. A., DeMartini, D. G., and Waite, J. H., 2018, "Intertidal Exposure Favors the Soft-Studded Armor of Adaptive Mussel Coatings," Nature Communications, **9**(1), p. 3424.

[18] Holten-Andersen, N., Fantner, G. E., Hohlbauch, S., Waite, J. H., and Zok, F. W., 2007, "Protective Coatings on Extensible Biofibres," Nature Mater, **6**(9), pp. 669–672.

[19] Bell, E., and Gosline, J., 1996, "Mechanical Design of Mussel Byssus: Material Yield Enhances Attachment Strength," Journal of Experimental Biology, **199**(4), pp. 1005–1017.

[20] Waite, J. H., Andersen, N. H., Jewhurst, S., and Sun, C., 2005, "Mussel Adhesion: Finding the Tricks Worth Mimicking," The Journal of Adhesion, **81**(3–4), pp. 297–317.
[21] Silverman, H. G., and Roberto, F. F., 2007, "Understanding Marine Mussel Adhesion," Mar Biotechnol, **9**(6), pp. 661–681.
[22] Aldred, N., Wills, T., Williams, D. n, and Clare, A. s, 2007, "Tensile and Dynamic Mechanical Analysis of the Distal Portion of Mussel (Mytilus Edulis) Byssal Threads," Journal of The Royal Society Interface, **4**(17), pp. 1159–1167.
[23] Zhao, H., and Waite, J. H., 2006, "Linking Adhesive and Structural Proteins in the Attachment Plaque of Mytilus Californianus*," Journal of Biological Chemistry, **281**(36), pp. 26150–26158.
[24] Brown, C. H., 1952, "Some Structural Proteins of Mytilus Edulis," Journal of Cell Science, **s3-93**(24), pp. 487–502.
[25] Lee, B. P., Messersmith, P. B., Israelachvili, J. N., and Waite, J. H., 2011, "Mussel-Inspired Adhesives and Coatings," Annual Review of Materials Research, **41**(1), pp. 99–132.
[26] Desmond, K. W., Zacchia, N. A., Waite, J. H., and Valentine, M. T., 2015, "Dynamics of Mussel Plaque Detachment," Soft Matter, **11**(34), pp. 6832–6839.
[27] Wilhelm, M. H., Filippidi, E., Waite, J. H., and Valentine, M. T., 2017, "Influence of Multi-Cycle Loading on the Structure and Mechanics of Marine Mussel Plaques," Soft Matter, **13**(40), pp. 7381–7388.
[28] Burkett, J. R., Wojtas, J. L., Cloud, J. L., and Wilker, J. J., 2009, "A Method for Measuring the Adhesion Strength of Marine Mussels," The Journal of Adhesion, **85**(9), pp. 601–615.
[29] Crisp, D. J., Walker, G., Young, G. A., and Yule, A. B., 1985, "Adhesion and Substrate Choice in Mussels and Barnacles," Journal of Colloid and Interface Science, **104**(1), pp. 40–50.
[30] Waite, J. H., 2002, "Adhesion à La Moule," Integr Comp Biol, **42**(6), pp. 1172–1180.
[31] Bell, E. C., and Gosline, J. M., 1997, "Strategies for Life in Flow: Tenacity, Morphometry, and Probability of Dislodgment of Two Mytilus Species," Marine Ecology Progress Series, **159**, pp. 197–208.
[32] Varenberg, M., and Gorb, S., 2008, "A Beetle-Inspired Solution for Underwater Adhesion," Journal of The Royal Society Interface, **5**(20), pp. 383–385.
[33] Gorb, S., 2001, Attachment Devices of Insect Cuticle, Springer Science & Business Media.
[34] Nachtigall, W., 2013, Biological Mechanisms of Attachment: The Comparative Morphology and Bioengineering of Organs for Linkage, Suction, and Adhesion, Springer Science & Business Media.
[35] Yang, X., and Deng, W., 2014, "Review on the Adhesive Tendrils of Parthenocissus," Chin. Sci. Bull., **59**(2), pp. 113–124.
[36] Russell, A. P., Stark, A. Y., and Higham, T. E., 2019, "The Integrative Biology of Gecko Adhesion: Historical Review, Current Understanding, and Grand Challenges," Integrative and Comparative Biology, **59**(1), pp. 101–116.
[37] Carrington, E., and Gosline, J. M., 2004, "Mechanical Design of Mussel Byssus: Load Cycle and Strain Rate Dependence," Am. Malacol. Bull., **18**.

[38] Vaccaro, E., and Waite, J. H., 2001, "Yield and Post-Yield Behavior of Mussel Byssal Thread: A Self-Healing Biomolecular Material," Biomacromolecules, **2**(3), pp. 906–911.
[39] Harrington, M. J., Masic, A., Holten-Andersen, N., Waite, J. H., and Fratzl, P., 2010, "Iron-Clad Fibers: A Metal-Based Biological Strategy for Hard Flexible Coatings," Science, **328**(5975), pp. 216–220.
[40] Sun, C., and Waite, J. H., 2005, "Mapping Chemical Gradients within and along a Fibrous Structural Tissue, Mussel Byssal Threads*," Journal of Biological Chemistry, **280**(47), pp. 39332–39336.
[41] Holten-Andersen, N., and Waite, J. H., 2008, "Mussel-Designed Protective Coatings for Compliant Substrates," J Dent Res, **87**(8), pp. 701–709.
[42] Valois, E., Hoffman, C., Demartini, D. G., and Waite, J. H., 2019, "The Thiol-Rich Interlayer in the Shell/Core Architecture of Mussel Byssal Threads," Langmuir, **35**(48), pp. 15985–15991.
[43] Lee, H., Dellatore, S. M., Miller, W. M., and Messersmith, P. B., 2007, "Mussel-Inspired Surface Chemistry for Multifunctional Coatings," Science, **318**(5849), pp. 426–430.
[44] Zhang, X., Huang, Q., Deng, F., Huang, H., Wan, Q., Liu, M., and Wei, Y., 2017, "Mussel-Inspired Fabrication of Functional Materials and Their Environmental Applications: Progress and Prospects," Applied Materials Today, **7**, pp. 222–238.
[45] Yang, H.-C., Luo, J., Lv, Y., Shen, P., and Xu, Z.-K., 2015, "Surface Engineering of Polymer Membranes via Mussel-Inspired Chemistry," Journal of Membrane Science, **483**, pp. 42–59.
[46] Zhang, C., Wu, B., Zhou, Y., Zhou, F., Liu, W., and Wang, Z., 2020, "Mussel-Inspired Hydrogels: From Design Principles to Promising Applications," Chemical Society Reviews, **49**(11), pp. 3605–3637.
[47] Zhang, L., Liu, Z., Wu, X., Guan, Q., Chen, S., Sun, L., Guo, Y., Wang, S., Song, J., Jeffries, E. M., He, C., Qing, F.-L., Bao, X., and You, Z., 2019, "A Highly Efficient Self-Healing Elastomer with Unprecedented Mechanical Properties," Advanced Materials, **31**(23), p. 1901402.
[48] Filippidi, E., Cristiani, T. R., Eisenbach, C. D., Waite, J. H., Israelachvili, J. N., Ahn, B. K., and Valentine, M. T., 2017, "Toughening Elastomers Using Mussel-Inspired Iron-Catechol Complexes," Science, **358**(6362), pp. 502–505.
[49] Holten-Andersen, N., Harrington, M. J., Birkedal, H., Lee, B. P., Messersmith, P. B., Lee, K. Y. C., and Waite, J. H., 2011, "PH-Induced Metal-Ligand Cross-Links Inspired by Mussel Yield Self-Healing Polymer Networks with near-Covalent Elastic Moduli," PNAS, **108**(7), pp. 2651–2655.
[50] Lin, Q., Gourdon, D., Sun, C., Holten-Andersen, N., Anderson, T. H., Waite, J. H., and Israelachvili, J. N., 2007, "Adhesion Mechanisms of the Mussel Foot Proteins Mfp-1 and Mfp-3," PNAS, **104**(10), pp. 3782–3786.
[51] Russell, A. P., and Johnson, M. K., 2009, "The Gecko Effect: Design Principles of the Gekkotan Adhesive System Across Scales of Organization," Functional Properties of Bio-Inspired Surfaces, WORLD SCIENTIFIC, pp. 103–132.
[52] Johnson, K. L., Kendall, K., Roberts, A. D., and Tabor, D., 1971, "Surface Energy and the Contact of Elastic Solids," Proceedings of the Royal Society of London. A. Mathematical and Physical Sciences, **324**(1558), pp. 301–313.

[53] Autumn, K., 2007, “Gecko Adhesion: Structure, Function, and Applications,” MRS Bulletin, **32**(6), pp. 473–478.
[54] Autumn, K., and Peattie, A. M., 2002, “Mechanisms of Adhesion in Geckos,” Integrative and Comparative Biology, **42**(6), pp. 1081–1090.
[55] Khaderi, S. N., Fleck, N. A., Arzt, E., and McMeeking, R. M., 2015, “Detachment of an Adhered Micropillar from a Dissimilar Substrate,” Journal of the Mechanics and Physics of Solids, **75**, pp. 159–183.
[56] Kamperman, M., Kroner, E., Campo, A. del, McMeeking, R. M., and Arzt, E., 2010, “Functional Adhesive Surfaces with ‘Gecko’ Effect: The Concept of Contact Splitting,” Advanced Engineering Materials, **12**(5), pp. 335–348.
[57] Barreau, V., Hensel, R., Guimard, N. K., Ghatak, A., McMeeking, R. M., and Arzt, E., 2016, “Fibrillar Elastomeric Micropatterns Create Tunable Adhesion Even to Rough Surfaces,” Advanced Functional Materials, **26**(26), pp. 4687–4694.
[58] del Campo, A., Greiner, C., and Arzt, E., 2007, “Contact Shape Controls Adhesion of Bioinspired Fibrillar Surfaces,” Langmuir, **23**(20), pp. 10235–10243.
[59] Spuskanyuk, A. V., McMeeking, R. M., Deshpande, V. S., and Arzt, E., 2008, “The Effect of Shape on the Adhesion of Fibrillar Surfaces,” Acta Biomaterialia, **4**(6), pp. 1669–1676.
[60] Balijepalli, R. G., Begley, M. R., Fleck, N. A., McMeeking, R. M., and Arzt, E., 2016, “Numerical Simulation of the Edge Stress Singularity and the Adhesion Strength for Compliant Mushroom Fibrils Adhered to Rigid Substrates,” International Journal of Solids and Structures, **85–86**, pp. 160–171.
[61] Afferrante, L., and Carbone, G., 2013, “The Mechanisms of Detachment of Mushroom-Shaped Micro-Pillars: From Defect Propagation to Membrane Peeling,” Macromolecular Reaction Engineering, **7**(11), pp. 609–615.
[62] Heepe, L., and Gorb, S. N., 2014, “Biologically Inspired Mushroom-Shaped Adhesive Microstructures,” Annu. Rev. Mater. Res., **44**(1), pp. 173–203.
[63] Li, Y., Krahn, J., and Menon, C., 2016, “Bioinspired Dry Adhesive Materials and Their Application in Robotics: A Review,” J Bionic Eng, **13**(2), pp. 181–199.
[64] Hensel, R., Moh, K., and Arzt, E., 2018, “Engineering Micropatterned Dry Adhesives: From Contact Theory to Handling Applications,” Advanced Functional Materials, **28**(28), p. 1800865.
[65] Sameoto, D., and Menon, C., 2010, “Recent Advances in the Fabrication and Adhesion Testing of Biomimetic Dry Adhesives,” Smart Mater. Struct., **19**(10), p. 103001.
[66] Kwak, M. K., Jeong, H.-E., and Suh, K. Y., 2011, “Rational Design and Enhanced Biocompatibility of a Dry Adhesive Medical Skin Patch,” Adv Mater, **23**(34), pp. 3949–3953.
[67] Baik, S., Kim, D. W., Park, Y., Lee, T.-J., Ho Bhang, S., and Pang, C., 2017, “A Wet-Tolerant Adhesive Patch Inspired by Protuberances in Suction Cups of Octopi,” Nature, **546**(7658), pp. 396–400.
[68] Bae, W. G., Kim, D., Kwak, M. K., Ha, L., Kang, S. M., and Suh, K. Y., 2013, “Enhanced Skin Adhesive Patch with Modulus-Tunable Composite Micropillars,” Advanced Healthcare Materials, **2**(1), pp. 109–113.

[69] Areyano, M., Gockowski, L., and Valentine, M. T., 2018, "Geometric Control of Adhesion Inspired by Mussel Plaque/Thread Structures," Proceeding Adhesion Soceity Annual Meeeting, San Diego, California.
[70] Waite, J. H., Qin, X.-X., and Coyne, K. J., 1998, "The Peculiar Collagens of Mussel Byssus," Matrix Biology, **17**(2), pp. 93–106.
[71] Lucas, J. M., Vaccaro, E., and Waite, J. H., 2002, "A Molecular, Morphometric and Mechanical Comparison of the Structural Elements of Byssus from Mytilus Edulis and Mytilus Galloprovincialis," Journal of Experimental Biology, **205**(12), pp. 1807–1817.
[72] Harrington, M. J., and Waite, J. H., 2007, "Holdfast Heroics: Comparing the Molecular and Mechanical Properties of Mytilus Californianus Byssal Threads," Journal of Experimental Biology, **210**(24), pp. 4307–4318.
[73] Brown, J. C., and Timpl, R., 1995, "The Collagen Superfamily," IAA, **107**(4), pp. 484–490.
[74] Mienaltowski, M. J., and Birk, D. E., 2014, "Structure, Physiology, and Biochemistry of Collagens," Progress in Heritable Soft Connective Tissue Diseases, J. Halper, ed., Springer Netherlands, Dordrecht, pp. 5–29.
[75] Shoulders, M. D., and Raines, R. T., 2009, "Collagen Structure and Stability," Annu. Rev. Biochem., **78**(1), pp. 929–958.
[76] Bhattacharjee, A., and Bansal, M., 2005, "Collagen Structure: The Madras Triple Helix and the Current Scenario," IUBMB Life, **57**(3), pp. 161–172.
[77] Harrington, M. J., "Structure-Function Relationships in the Proteinaceous Fibers of the Mussel Byssus," Ph.D., University of California, Santa Barbara.
[78] Rudall, K. M., 1955, "The Distribution of Collagen and Chitin," pp. 49–71.
[79] Spiro, R. G., Lucas, F., and Rudall, K. M., 1971, "Glycosylation of Hydroxylysine in Collagens," Nature New Biology, **231**(19), pp. 54–55.
[80] Qin, X., and Waite, J. H., 1995, "Exotic Collagen Gradients in the Byssus of the Mussel Mytilus Edulis.," Journal of Experimental Biology, **198**(3), pp. 633–644.
[81] Qin, X.-X., and Waite, J. H., 1998, "A Potential Mediator of Collagenous Block Copolymer Gradients in Mussel Byssal Threads," PNAS, **95**(18), pp. 10517–10522.
[82] Coyne, K. J., Qin, X.-X., and J. Herbert, W., 1997, "Extensible Collagen in Mussel Byssus: A Natural Block Copolymer | Science," Science, **277**(5333), pp. 1830–1832.
[83] Mascolo, J. M., and Waite, J. H., 1986, "Protein Gradients in Byssal Threads of Some Marine Bivalve Molluscs," Journal of Experimental Zoology, **240**(1), pp. 1–7.
[84] Bailey, A. J., Macmillan, J., Shrewry, P. R., Tatham, A. S., Waite, J. H., Vaccaro, E., Sun, C., and Lucas, J. M., 2002, "Elastomeric Gradients: A Hedge against Stress Concentration in Marine Holdfasts?," Philosophical Transactions of the Royal Society of London. Series B: Biological Sciences, **357**(1418), pp. 143–153.
[85] Persikov, A. V., Ramshaw, J. A. M., and Brodsky, B., 2005, "Prediction of Collagen Stability from Amino Acid Sequence *," Journal of Biological Chemistry, **280**(19), pp. 19343–19349.
[86] Sundberg, R. J., and Martin, R. B., 1974, "Interactions of Histidine and Other Imidazole Derivatives with Transition Metal Ions in Chemical and Biological Systems," Chem. Rev., **74**(4), pp. 471–517.

[87] Schmitt, C. N. Z., Politi, Y., Reinecke, A., and Harrington, M. J., 2015, "Role of Sacrificial Protein–Metal Bond Exchange in Mussel Byssal Thread Self-Healing," Biomacromolecules, **16**(9), pp. 2852–2861.
[88] Coombs, T. L., and Keller, P. J., 1981, "Mytilus Byssal Threads as an Environmental Marker for Metals," Aquatic Toxicology, **1**(5), pp. 291–300.
[89] Sagert, J., and Waite, J. H., 2009, "Hyperunstable Matrix Proteins in the Byssus of Mytilus Galloprovincialis," Journal of Experimental Biology, **212**(14), pp. 2224–2236.
[90] Suhre, M. H., and Scheibel, T., 2014, "Structural Diversity of a Collagen-Binding Matrix Protein from the Byssus of Blue Mussels upon Refolding," Journal of Structural Biology, **186**(1), pp. 75–85.
[91] Gosline, J. M., 2018, Mechanical Design of Structural Materials in Animals, Princeton University Press.
[92] Smeathers, J. E., and Vincent, J. F. V., 1979, "Mechanical Properties of Mussel Byssus Threads," Journal of Molluscan Studies, **45**(2), pp. 219–230.
[93] Pearce, T., and LaBarbera, M., 2009, "A Comparative Study of the Mechanical Properties of Mytilid Byssal Threads," Journal of Experimental Biology, **212**(10), pp. 1442–1448.
[94] Pollock, C. M., and Shadwick, R. E., 1994, "Relationship between Body Mass and Biomechanical Properties of Limb Tendons in Adult Mammals," American Journal of Physiology-Regulatory, Integrative and Comparative Physiology, **266**(3), pp. R1016–R1021.
[95] Butler, D. L., Juncosa, N., and Dressler, M. R., 2004, "Functional Efficacy of Tendon Repair Processes," Annual Review of Biomedical Engineering, **6**(1), pp. 303–329.
[96] Mullins, L., 1948, "Effect of Stretching on the Properties of Rubber," Rubber Chemistry and Technology, **21**(2), pp. 281–300.
[97] Mullins, L., 1969, "Softening of Rubber by Deformation," Rubber Chemistry and Technology, **42**(1), pp. 339–362.
[98] Dorfmann, A., and Ogden, R. W., 2003, "A Pseudo-Elastic Model for Loading, Partial Unloading and Reloading of Particle-Reinforced Rubber," International Journal of Solids and Structures, **40**(11), pp. 2699–2714.
[99] Krauss, S., Metzger, T. H., Fratzl, P., and Harrington, M. J., 2013, "Self-Repair of a Biological Fiber Guided by an Ordered Elastic Framework," Biomacromolecules, **14**(5), pp. 1520–1528.
[100] Reinecke, A., Bertinetti, L., Fratzl, P., and Harrington, M. J., 2016, "Cooperative Behavior of a Sacrificial Bond Network and Elastic Framework in Providing Self-Healing Capacity in Mussel Byssal Threads," Journal of Structural Biology, **196**(3), pp. 329–339.

Chapter 2. Geometrical dependencies of mussel inspired adhesion

2.1 Introduction

The work presented in this chapter was conducted to develop an understanding between physical geometrical parameters and adhesion of fibrillar structures inspired by marine mussels. We focused on adhesive structures inspired by mussels because they are almost always deposited radially outwardly exhibiting a geometry with large variations in deposit angles. The work introduced here was supervised by Professor Megan T. Valentine.

Marine mussels are known for thriving in the hostile intertidal zone, withstanding tensile loading from waves and predators [1]. To survive this environment and anchor themselves to surfaces, they quickly make and deposit byssus radially with the use of their foot. Singular threads exhibit a mushroom-shaped structure composed of a collagenous thread (stalk) terminating in a flat circular plaque (mushroom-tip). The adhesive properties and tenacity exhibited by the byssus have lead to many articles aimed at dissecting components involved in the tenacity of these structures [2–9]. Much of the work conducted, although not all, has focused on the properties of the plaque and distal thread separately. Studies of the adhesive plaque have identified 3,4-dihydroxy-L-phenyl-alanine (DOPA) as an indispensable component in the mussels ability to bind to surfaces in the harsh wet environment [10–14]. Furthermore, studies performed on the distal threads have shown that the internal microstructure of the collagenous core is essential for their high extensibility and energy dissipative mechanism, while the stiff cuticle serves as a protective means but also exhibits excellent mechanical properties [15–22].

Understanding the building blocks of the adhesive and mechanical properties of marine mussel byssus has lead to promising new materials which incorporate the chemistry observed within the plaque and cuticle [10–14,23,24]. However, much is yet to be understood about how physical parameters such as the mushroom-shaped geometry affect mussel adhesion. Previous work conducted on micron-scale mushroom-shaped geometry have shown that the mushroom-shaped geometry is optimal for dry adhesion, such as in the gecko system, when compared to other geometries such as straight punches and spatula-shaped geometries [25]. Mussels take full advantage of this mushroom-shaped geometry with some variations such as casting angles, and scale [26]. To decouple the effects of chemistry versus geometry, we utilized macro-scale synthetic structures to mimic marine mussel structures (Figure 2.1). In order to accomplish this, we fabricated structures using custom-designed 3D printed and performed measurements on the adhesion as a function of geometry. Furthermore, we developed a technique that allowed us to test adhesion that was semi-permanent, whereas previous studies have focused on dry adhesion.

The use of millimeter-scale structures enabled us to observe structural deformation during pull tests, as well as modes of failure (center vs. edge cracks). This is something that has proven to be difficult for individual structures at the micron-scale [27–35]. To assess geometrical effects the geometry of the structures was varied using several deposit angles, thus creating asymmetric structures as well as the fillet radius found between the stalk and tip (Figure 2.1). The use of macroscale structures enabled real-time imaging with the use of a custom three-camera imaging system. Comparing forces and extensions at failure allowed us to gain an

improved understanding of how geometrical parameters such as pull-off angles and deposit angles influenced adhesive properties.

2.2 Methods

2.2.1 Design and manufacturing of structures

The mussel-inspired structures were generated by printing 3D molds that were injected with a silicone elastomer, which was then cured, released from the mold, adhered to a glass substrate, and tested. Each custom mold was designed in SolidWorks to mimic the thread-plaque structures of the byssus of marine mussels[3,5,6,12]. Each mimic consisted of a thin stalk of radius 1.5 mm that terminated in a larger disk of 6.0 mm radius that mimics the general features of the mussel plaque (Figure 2.1). The angle formed between the stalk and disk, which we call the casting angle θ, was varied (here, θ = 45º, 60º, 90º). The rounded corner (fillet, R_f) that connects the stalk to the disk was also varied from no rounding to a radius of 5.0 mm. The top of the structure terminated in a thick cylindrical button to enable clamping and pulling in the tensile testing device. A second, smaller fillet (radius 2.1 mm) was added at the top of the stalk where it met the button to reduce stress concentrations and prevent failure at this junction.

Each mold comprised four pieces: two identical halves that when fitted together created the main shape (Appendix A, Figure A.2), as well as a top and bottom plate that sealed and secured the structure. Each mold allowed the formation of five identical structures for mechanical testing. Molds were printed with a Stratasys Objet30 Pro 3D printer using Rigur simulated polypropylene (RGD 450) print material and SUP 705 support material. All molds were printed with a glossy finish. The surface roughness of the molds was found to be highly dependent on the age of the print heads. To ensure that the surface roughness was kept constant across all

conditions, the same molds were used to fabricate all samples. Surface roughness measurements for glossy surfaces on the same printer exhibited a root mean squared amplitude of 140 nm ± 55 nm (N = 3) when characterized using a DektakXT Stylus Profilometer (Bruker, Billerica, MA) with a scan length of 2500 μm.

During printing, we oriented the structure to avoid the use of support material on the surface that will come into contact with the elastomer, as this adds roughness. Due to printer limitations it was not possible to print molds with casting angles less than approximately 40º without significant added support material. This limited the resolution of sharp features in the molds: since the resulting structure differed significantly from the others, the $\theta = 30^{\circ}$ case was not tested. After printing, each mold was cleaned to remove support material, first by hand with a razor blade, and then by blasting with water. Molds were then towel dried and outgassed for 6 hours at a minimum temperature of 60°C in a 1310 standard oven (VWR, Cornelius, OR). Outgassing the molds before use prevents the structures from sticking during the demolding process.

The adhesive structures were generated by injection of a thermally curable commercial polydimethylsiloxane (PDMS) elastomer (Sylgard 184, Dow Corning, Midland, MI) into the custom molds. PDMS was selected because it is well-characterized, its mechanical and interfacial properties enable significant sample deformation under modest loads, and bonding conditions that bias adhesive failure can be achieved [36]. Before injection, the PDMS was mixed by hand at a 10:1 weight ratio of base to crosslinking agent, per the manufacturer's instructions, and degassed for at least 5 minutes. The mixture was immediately injected using

5 mL syringes into the molds and cured for 2 hours at 75°C before being released from the molds.

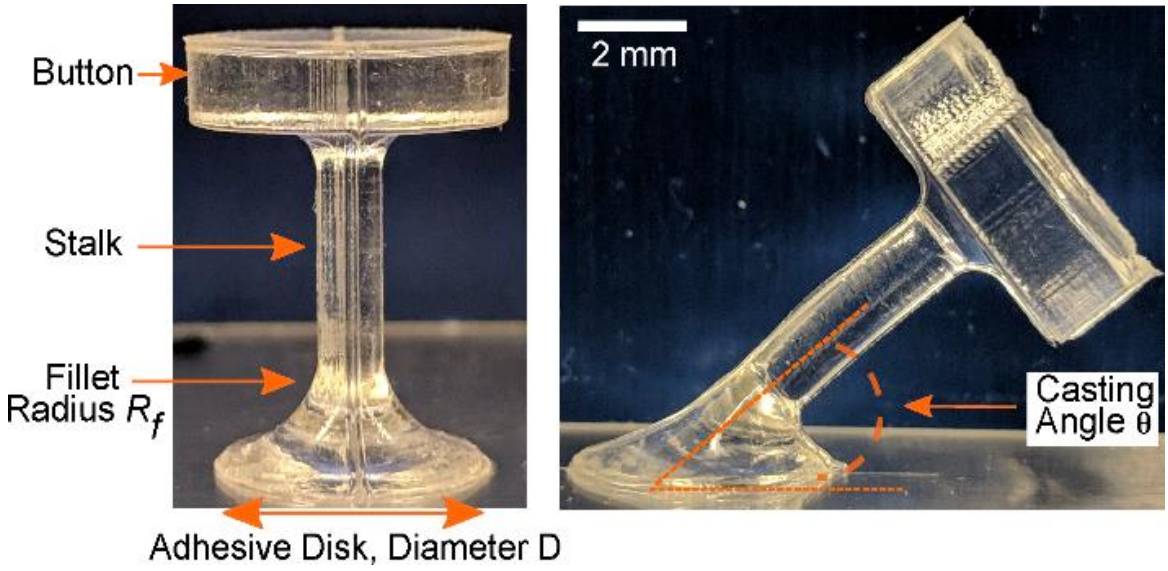

Figure 2.1: Image of PDMS-based, mussel-inspired adhesive structures cast at 90º (left) and 45º (right). The adhesive interface is at the bottom of the image. The button at the top enables attachment of the structure to the tensile testing machine via a custom clamp (Appendix A, Figure A.1). The dimensions are as follows: the stalk radius $b = 1.5$ mm, the flange thickness $h = 0.5$ mm, the flanged tip diameter $D = 12$ mm., fillet radius $R_f = 5$ mm.

2.2.2 Structure adherence to a glass substrate

Within 24 hours of curing, the silicone structures were adhered to borosilicate microscope slides (25×75 mm). Before attachment, each slide was etched using a laser cutter (Trotec,

Marchtrenk, Austria) to create a circular alignment marker at its center. The silicone structures and the microscope slides were placed in an ozone cleaner (PSD-UV6, Novascan, Boone, IA) and oriented such that their adherent surfaces faced the UV lamp. The surfaces were treated for 10 minutes to remove organic contaminants, and then each structure was directly placed on a microscope slide with enough contact pressure to remove trapped air bubbles and form the initial adhesive bond. The samples were then baked at 85 ºC for 5 minutes. This results in an adhesive interface that is strong enough to withstand substantial tensile stress, but one that will typically fail prior to the cohesive failure of the structure, allowing the dynamics of debonding and delamination to be observed.

2.2.3 Mechanical testing

To better understand the role of geometry and structural deformation in adhesive performance, the synthetic structures were loaded and simultaneously imaged using a custom-built, displacement-controlled tensile tester with multi-camera imaging capabilities (Appendix A, Figure A.3). A Lebow Load Cell (Model 3108–10, 10-lb capacity Honeywell Sensing & Control, Charlotte, NC) with custom amplifying electronics was connected to a computer via a USB-mediated data acquisition (DAQ) module (DT9804, Measurement Computing, Norton, MA). Command of the stepper motor (ES22B, Parker CompuMotor, Irwin, PA) via an indexer controller (ZETA 6104, Parker CompuMotor, Irwin, PA), as well as acquisition of force and displacement data, was performed in LabVIEW (National Instruments, Austin, TX). To enable secure attachment and alignment, a custom tilt stage that can control pulling (loading) angle φ from 30º–90º and clamps were designed in SolidWorks and then 3D printed with a glossy finish (Objet 30 Pro, print material RGD450, support material SUP705). For each experiment,

the stage was rotated to the desired loading angle. The microscope slide with adherent sample was placed on the stage and the center of the structure was aligned by eye to the center of the load cell (Appendix A, Figure A.1). The free end of the sample (the 'button', see Figure 2.1) was then placed inside custom clamps and again centered by eye, allowing tensile loads to be applied. The strain rate was set to either 0.004 or 0.008 s^{-1}. Experiments indicated no obvious strain rate dependence in this regime.

The deformation of the elastic structure was recorded during each tensile test using up to three cameras each giving a different view. A Canon Rebel SL2 (Canon 100mm f/2.8 Macro USM fixed lens, frame rate of 30 frames per second (fps)) captured the structural deformation of the whole sample at high resolution from a front view. To observe failure modes at the structure:substrate interface, we use a ViTiny UM02 USB Digital Microscope camera that fit under the stage with variable magnification between 1-320X (30 fps). To capture high magnification videos of failure modes from a sideview we use the Jiusion endoscope with variable magnification between 40-1000X (25 fps). For each experiment, the magnification of each camera was manually adjusted to ensure that the structure or interface fully filled the field of view. Front view images were recorded for almost every sample and a subset of samples was chosen for imaging with additional cameras to provide views of the adherent surface.

Post-experiment, videos were reviewed and the qualitative features of the detachment were noted. We manually scored the mode of failure, which included adhesive failure by the propagation of an edge-initiated crack, growth of a center-initiated cavity, simultaneous propagation of edge- and center-initiated cracks or by cohesive failure within the structure body. Cracks are defined here as regions where the PDMS interface separated from the glass.

The presence and location of cracks at the adhesive interface was recorded, as well as the time(s) at which crack initiation occurred. In total, 121 structures were mechanically tested and imaged by at least one camera; 40 of the samples were imaged with all three cameras.

To enable statistically-meaningful comparisons of the force-extension data collected with different samples and loading schemes, the distributions of forces and elongations at failure were compared using a pairwise Student's t-test implemented in MATLAB.

2.3 Results

2.3.1 Effect of loading angle on force-extension behavior

Force and extensions were recorded to complement the imaging of detachment mechanism of the mussel-inspired structures. Due to changes in the cross-sectional area of the structures, the force and extension are presented instead of stress and strain. An increase in force with extensions up until failure was observed in all tests, and this is visible in the representative force-extension curve is shown in Figure 2.2. As a result of the hyperelastic mechanical response of PDMS, stiffening was observed as structures approached failure [36]. In some tests, as the structures peeled from the glass substrate fluctuations in the force were observed.

The force F_{max} and extension at failure Δ_{max} peaked under loading conditions where $\theta = \varphi$ (Figure 2.3, Table 2.1). Asymmetrically cast and loaded structures (i.e. the 45º/45º and 60º/60º cases) showed no statistical difference in pull-off forces between configurations compared to the 90º/90º case with maximum forces ~ 8N. Compared to this, symmetric structures pulled at asymmetric angles (90º/X where X < 90º), showed a decrease in both F_{max} and Δ_{max} as much as 40%, exhibiting a statistical difference. Significance was assessed using pairwise

Student's t-tests of 90º/X compared to 90º /90º, $p < 0.05$. A full accounting of the results of the statistical analysis of these data are provided in Table 2.2.

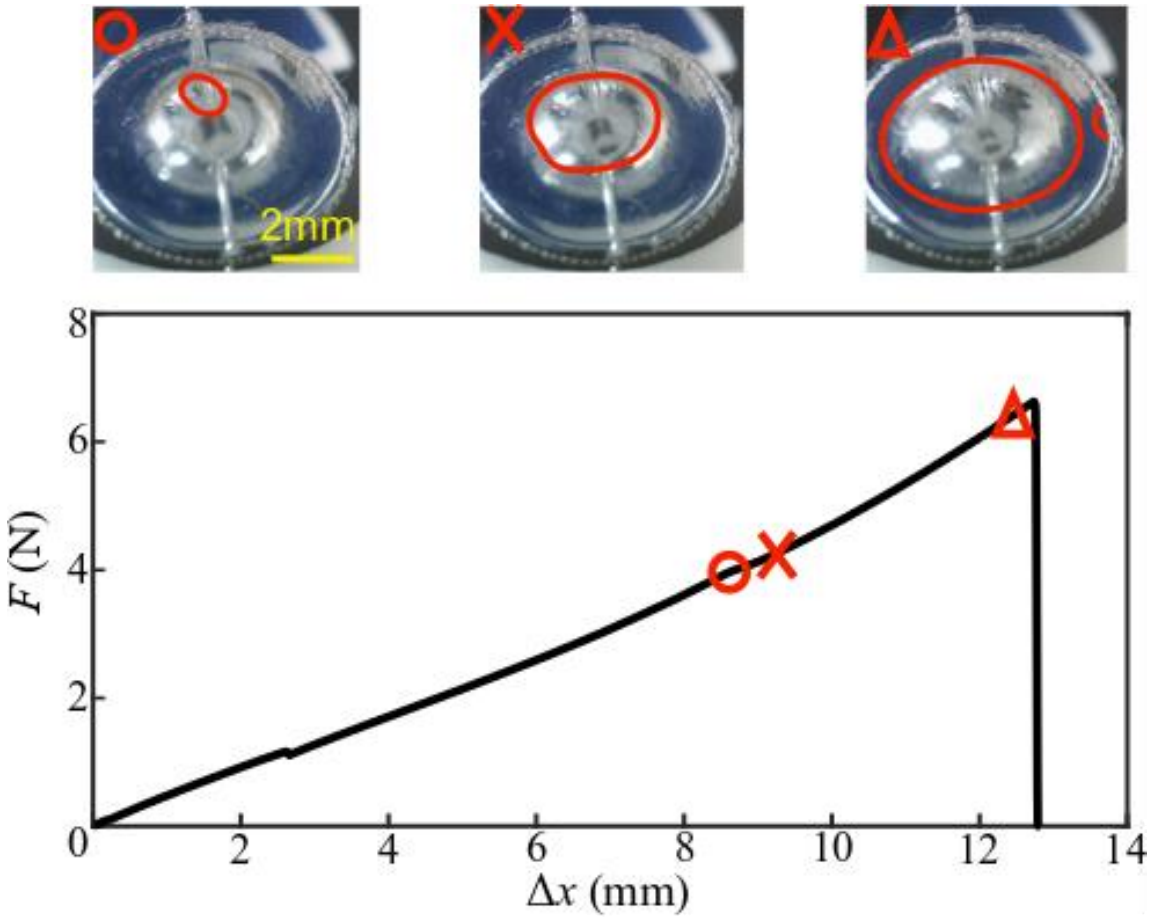

Figure 2.2: Representative force-extension trace for 90º/60º loading. The images show center and edge crack growth. The markers indicates time points just after crack initiation (circle), after rapid crack growth (X), and after the appearance of an edge crack (triangle). The crack boundaries are highlighted (red lines) in each image.

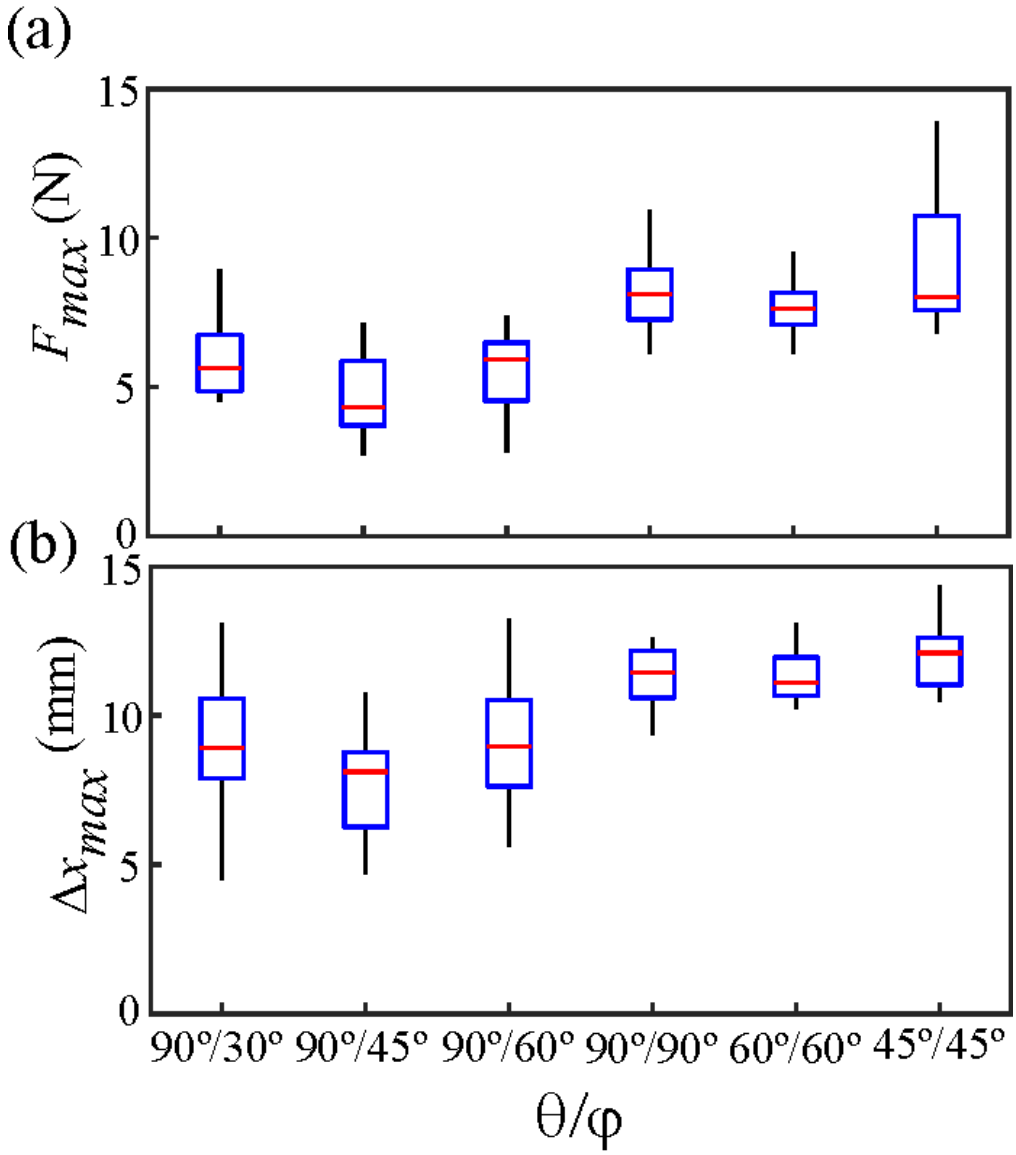

Figure 2.3: Effects of casting and pull angle on (a) peak forces at failure F_{max} and (b) elongations to failure Δx_{max}. In each plot, the red line indicates the median value, the upper box edge represents the 75th percentile, the lower box edge represents the 25th percentile, and the upper and lower whisker extensions represent the 90th and 10th percentiles, respectively (N = 7-24).

Table 2.1: Average maximum forces and elongations for the different configurations. Results were determined experimentally via pull-off tests.

Loading Configuration (θ/ φ)	**Average Peak Forces F_{max} (N)**	**Average Peak Elongation Δx (mm)**
90°/90°	8.14 ± 1.56	11.33 ± .95
60°/60°	7.76 ± 1.15	11.29 ± 1.04
45°/45°	8.96 ± 3.06	11.67 ± 2.13
90°/60°	5.45 ± 1.46	9.04 ± 2.51
90°/45°	4.67 ± 1.27	7.64 ± 1.57
90°/30°	5.66 ± 2.13	8.59 ± 2.51

Table 2.2: Results of the Student's t-test analysis of pairs of loading configurations. The h-value is binary with 1 indicating statistical significance at the 95% confidence level (which corresponds to a p-value of 0.05)

Pairs of Loading	**Force**		**Elongation**	
Configuration (θ/ φ)	***h*-value**	***p*-value**	***h*-value**	***p*-value**
90°/30° & 90°/90°	1	7.14 e-4	1	3.86e-4
90°/45° & 90°/90°	1	4.02e-4	1	8.52e-10
90°/60° & 90°/90°	1	4.09e-6	1	.0019
60°/60° & 90°/90°	0	0.41	0	0.92
45°/45° & 60°/60°	0	0.36	0	0.57
90°/45° & 45°/45°	1	2.03e-7	1	1.10e-8
90°/60° & 60°/60°	1	1.71e-6	1	7.62e-4
90°/60° & 90°/30°	0	0.71	0	0.57
90°/60° & 90°/45°	0	0.06	1	0.03
90°/30° & 90°/45°	0	0.07	0	0.14
60°/60° & 45°/45°	0	0.12	0	0.49

2.3.2 Effects of loading angle on detachment mechanisms

To assess angle effects on the adhesive properties of the mussel-inspired structures with both symmetric and asymmetric geometries, structures were cast and pulled at angles varying between 30º - 90º. Symmetric structures were casted at an angle $\theta = 90º$ and pulled at angles between $\varphi = 30º - 45º$. Synthetic mimics cast at angles other than 90º were pulled at the same angle at which they were deposited. Over 95% of the structures tested, failed adhesively (detached from the glass substrate) with rare instances of cohesive failure which typically occurred at the button stalk interface.

Over 95% of all samples which failed adhesively exhibited center-initiated cracks which were followed by edge-cracks leading to failure. The center-initiated cracks would be appear within the first minute of loading and would grow slowly outwardly, and eventually as the maximum forces were approached, in most cases, an edge crack would be observed as shown in Figure 2.2. These two cracks would then coalesce causing final detachment from the glass substrate. This type of behavior was also observed with the side and/or below camera, as these cameras could more accurately capture crack propagation. Using this viewing system also allowed us to capture edge cracks. This type of observation was only captured for a subset of samples due to camera limitations. Furthermore, for the pull angle $\varphi = 30º$ constraints between the stage and camera prevented us from capturing a bottom and side view of the detachment.

Structures cast at angles other than $\theta = 90º$, were pulled at the same angle $\theta = \varphi$ (i.e. 45º/45º or 60º/60º). These structures showed similar failure mechanisms with a center initiated crack followed by an edge crack. The main difference in detachment was the location in which the center cracks originated. Structures with a 90º/90º configuration showed center-cracks that

originated in random locations whereas structures with a 45º/45º configuration showed cracks originating on the compression side slightly off-center. Contrary to this, structures cast at a 90º angle and pulled at various angles showed center cracks which biased the tension side. The tension and compression sides are shown visually in Appendix A, Figure A.1.

2.3.3 Effect of fillet radius on detachment mode and adhesion strength

Previous work has suggested that the fillet at the interface of the stalk and mushroom-tip can influence the adhesive strength of mushroom-shaped structures [37]. Mussel byssal threads exhibit a fillet radius between the thread and plaque, which likely serves to mitigate stresses at this junction. A fillet radius of $R_f = 5$ mm, which closely resembles the fillet radius of byssal threads, was chosen for all experiments previously presented [1, 10, 26, 27]. To assess the role of the fillet radius, structures were designed with a smaller to no fillet radius and maximum forces (F_{max}) and elongation (Δ_{max}) were compared. To evaluate the three configurations, we utilize a dimensionless parameter $\frac{R_f}{D}$ between the fillet radius (R_f) and mushroom-tip diameter (D), with the mushroom-tip diameter staying constant. The experimental results presented here, were all performed on structures cast and pulled at the same angle ($\theta = \varphi = 90º$).

All structures with a $\frac{R_f}{D} = .41$, corresponding to a fillet radius of $R_f = 5$mm, exhibited adhesive type failure and had the highest pull-off forces compared to the other two conditions. In comparison, samples with $\frac{R_f}{D} = .1$ or 0 (no fillet) mostly failed adhesively (>85%) with some cohesive failures and exhibited a combination of both center- and edge-initiated cracks. The most notable change in adhesive failure between configurations was a decrease in pull-off

force. Reducing $\frac{R_f}{D}$ to 0.1 and 0, caused a decrease in pull-off forces of about 30% in comparison to $\frac{R_f}{D} = .41$, showing a statistical difference (Figure 2.4, Table 2.3). However, there was no statistical difference between $\frac{R_f}{D} = 0.1$ and $\frac{R_f}{D} = 0$. The statistical analysis of these results is presented in Table 2.4.

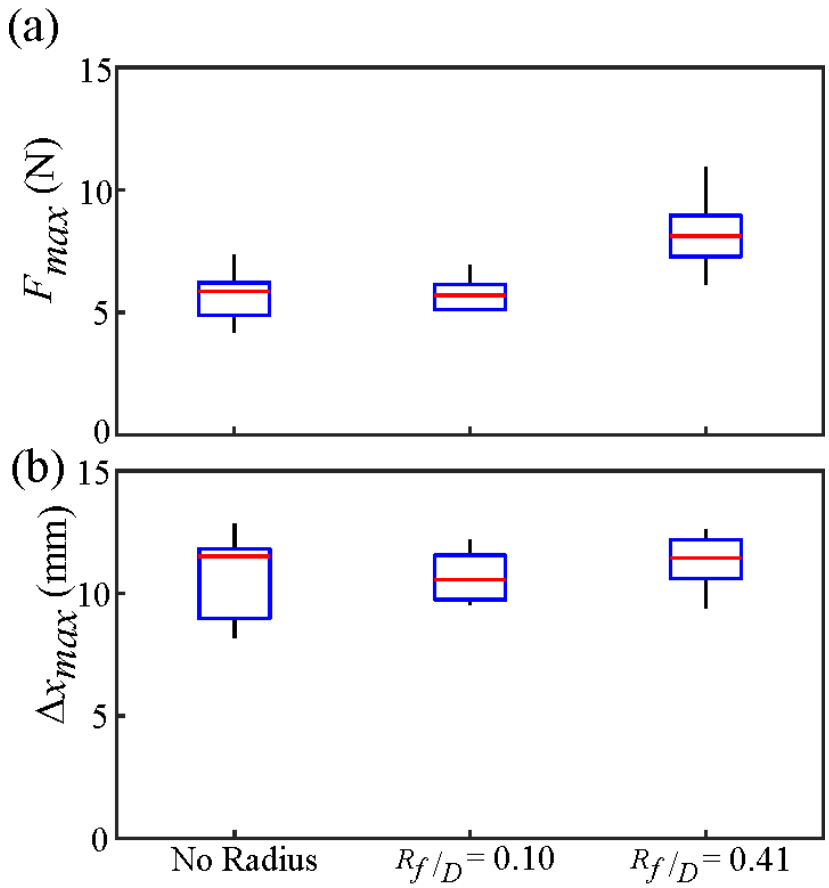

Figure 2.4: Effects of varying fillet radii on peak force and maximum elongation. Box plot is constructed as in Figure 3. 9-13 samples were tested per condition

Table 2.3: Average maximum forces and elongations for the various fillet radii. Results were determined experimentally via pull-off tests.

Geometry	Average Peak Forces F_{max} (N)	Average Peak Elongation Δx (mm)
R_f/D = 0	5.65±0.95	10.75±1.64
R_f/D = .10	5.58±0.91	10.28±1.65
R_f/D = .41	8.15±1.56	11.33±0.95

Table 2.4: Results of the Student's t-test analysis of pairs of loading configurations as a function of for the different fillet radii. The h-value is binary with 1 indicating statistical significance at the 95% confidence level (which corresponds to a p-value of 0.05).

	Force		Elongation	
Geometry Comparisons	***h*-value**	***p*-value**	***h*-value**	***p*-value**
R_f/D = 0 & R_f/D = .10	0	0.87	0	0.56
R_f/D =.10 & R_f/D = .41	1	1.85e-4	0	0.06
R_f/D = .41 & R_f/D = 0	1	1.53e-4	0	0.26

2.4 Discussion

To build a better understanding of how geometrical parameters affect the adhesive properties of mussel-inspired structures, rapid prototyping of synthetic macrostructures was performed using 3D printed molds. A technique using an ozone treatment allowed us to test semi-permanent adhesion, more closely resembling the adhesion observed in mussel threads which is permanent. Using these techniques allowed us to test intricate geometries, with structures pulled and deposited at various angles and with fillet radius varied as well. Utilizing a three-camera imaging set up allowed us to capture detachment mechanisms, which was essential for understanding how stresses are distributed at the structure:substrate interface. Lastly, force and extensions were recorded to quantify the differences in adhesive strengths between configurations.

In comparison to a straight punch configuration, mushroom-shaped structures have shown to outperform in dry adhesive tests as, via their thin flanges, they mitigate severe edge stress concentration [29,37,38]. By introducing a thin flange the failure type between the two structures shifts from edge-initiated cracks (low pull off force) to center-initiated cracks. The increase in pull of forces can be as high as 30 times that of a straight punch [29]. Using the methods presented in section 2.2 revealed that the $\theta = \varphi$ geometry was optimal for achieving the highest forces and extensions, showing no statistical differences between 90º/90º, 60º/60º , and 45º/45º. Imaging also allowed us to observe that for these configurations center-initiated cracks were preferential, agreeing with previous work stating that in order to achieve the highest pull-off forces center-initiated cracks are desired [37–40].

Pulling on symmetrically cast structures ($\theta = 90^o$) at angles other than their cast angle ($\varphi < 90^o$) introduced a similar effect as observed in straight punches leading to a reduction in pull-off forces and shift from center-initiated cracks to edge-initiated cracks. One possible explanation as to why this is occurring is that by pulling at an angle other than the normal casting angle, a moment is introduced causing there to be more tension on one side versus the other. This in turn, leads to edge-initiated cracks resulting in lower pull-off forces. It is worth noting that although there is a decrease in pull-off forces for all 90^o/X with $X < 90^o$ conditions, as compared to the symmetric 90^o case, there is no significant trend in F_{max} with decreasing φ.

Understating the role of angles on the adhesive properties of mussel-adhesion has shown to be a difficult task, as it is impossible to decouple geometrical effects from the chemistry at the plaque:substrate interface in the natural system [26]. With the use of synthetic mimics, we were able to capture differences between pull and casting angles and their effects on adhesive strength. The results presented in this chapter demonstrate that the ideal configuration for maximum adhesive strength is for pull and casting angles to be the same. Interestingly, it has been observed that mussels typically deposit byssal threads that are cast and pulled at a similar angle. Previous work by Desmond et al. [6] showed that pulling threads at angles that lead to large moments cause a decrease in adhesive strength and compromise the structural integrity at the thread:plaque interface.

To complete the study of the effects of geometry on the adhesive strength of mussel-inspired structures we studied the effect of the fillet between the stalk and mushroom-tip. In the natural system it has been observed that most cohesive failures in byssal threads occur at the fillet

interface between the thread and plaque, indicating that this feature has an effect on overall structural integrity and failure mechanism [6]. With the use of mussel-inspired synthetic structures we demonstrate that reducing the fillet radius at the stalk-tip junction led to a decrease in pull-off forces and in some instances to cohesive failures. This agrees with previous computational work which proposed that the addition of a rounded fillet reduces the stress concentration directly under the position in which the stalk meets the tip, and thus leads to higher adhesive strength [37]. The differences between $\frac{R_f}{D} = 0.1$ and $\frac{R_f}{D} = 0$ were indistinguishable implying that there is likely a critical ratio between .41 and 0.1 at which adhesive strength is reduced. Once at the critical ratio adhesive strength is compromised, and further reduction in fillet radius has little to no effect on the adhesive strength.

Taking these data into consideration it can be proposed that changing the fillet radius and pulling at angles other than the casting angle have similar effects on the adhesive strength of macro-scale mushrooms-shaped structures. In both instances there was a decrease in pull-off force and a change to the detachment mechanism (adhesive vs. cohesive, center vs. edge cracks). This implies that structures casted and pulled at the same angle with a large fillet radius are optimal as they exhibit higher adhesive strength and involve center-initiated cracks.

2.5 References

[1] Waite, J. H., 1992, "The Formation of Mussel Byssus: Anatomy of a Natural Manufacturing Process," *Structure, Cellular Synthesis and Assembly of Biopolymers*, S.T. Case, ed., Springer, Berlin, Heidelberg, pp. 27–54.

[2] Bell, E., and Gosline, J., 1996, "Mechanical Design of Mussel Byssus: Material Yield Enhances Attachment Strength," Journal of Experimental Biology, **199**(4), pp. 1005–1017.

[3] Waite, J. H., 2017, "Mussel Adhesion – Essential Footwork," J of Experimental Biology, **220**(4), pp. 517–530.

[4] Filippidi, E., DeMartini, D. G., Molina, P. M. de, Danner, E. W., Kim, J., Helgeson, M. E., Waite, J. H., and Valentine, M. T., 2015, "The Microscopic Network Structure of Mussel (Mytilus) Adhesive Plaques," Journal of The Royal Society Interface, **12**(113), p. 20150827.

[5] Wilhelm, M. H., Filippidi, E., Waite, J. H., and Valentine, M. T., 2017, "Influence of Multi-Cycle Loading on the Structure and Mechanics of Marine Mussel Plaques," Soft Matter, **13**(40), pp. 7381–7388.

[6] Desmond, K. W., Zacchia, N. A., Waite, J. H., and Valentine, M. T., 2015, "Dynamics of Mussel Plaque Detachment," Soft Matter, **11**(34), pp. 6832–6839.

[7] Zhao, H., and Waite, J. H., 2006, "Linking Adhesive and Structural Proteins in the Attachment Plaque of Mytilus Californianus*," Journal of Biological Chemistry, **281**(36), pp. 26150–26158.

[8] Crisp, D. J., Walker, G., Young, G. A., and Yule, A. B., 1985, "Adhesion and Substrate Choice in Mussels and Barnacles," Journal of Colloid and Interface Science, **104**(1), pp. 40–50.

[9] Waite, J. H., Andersen, N. H., Jewhurst, S., and Sun, C., 2005, "Mussel Adhesion: Finding the Tricks Worth Mimicking," The Journal of Adhesion, **81**(3–4), pp. 297–317.

[10] Jeffrey L. Dalsin, Bi-Huang Hu, Bruce P. Lee, and, and Messersmith*, P. B., 2003, "Mussel Adhesive Protein Mimetic Polymers for the Preparation of Nonfouling Surfaces" [Online]. Available: https://pubs.acs.org/doi/abs/10.1021/ja0284963. [Accessed: 01-Mar-2019].

[11] Bruce P. Lee, Jeffrey L. Dalsin, and, and Messersmith*, P. B., 2002, "Synthesis and Gelation of DOPA-Modified Poly(Ethylene Glycol) Hydrogels" [Online]. Available: https://pubs.acs.org/doi/abs/10.1021/bm025546n. [Accessed: 01-Mar-2019].

[12] Lee, B. P., Messersmith, P. B., Israelachvili, J. N., and Waite, J. H., 2011, "Mussel-Inspired Adhesives and Coatings," Annual Review of Materials Research, **41**(1), pp. 99–132.

[13] S. Menyo, M., J. Hawker, C., and Herbert Waite, J., 2013, "Versatile Tuning of Supramolecular Hydrogels through Metal Complexation of Oxidation-Resistant Catechol-Inspired Ligands," Soft Matter, **9**(43), pp. 10314–10323.

[14] Moulay, S., 2014, "Dopa/Catechol-Tethered Polymers: Bioadhesives and Biomimetic Adhesive Materials," Polymer Reviews, **54**(3), pp. 436–513.

[15] Krauss, S., Metzger, T. H., Fratzl, P., and Harrington, M. J., 2013, "Self-Repair of a Biological Fiber Guided by an Ordered Elastic Framework," Biomacromolecules, **14**(5), pp. 1520–1528.

[16] Harrington, M. J., "Structure-Function Relationships in the Proteinaceous Fibers of the Mussel Byssus," Ph.D., University of California, Santa Barbara.
[17] Harrington, M. J., Gupta, H. S., Fratzl, P., and Waite, J. H., 2009, "Collagen Insulated from Tensile Damage by Domains That Unfold Reversibly: In Situ X-Ray Investigation of Mechanical Yield and Damage Repair in the Mussel Byssus," Journal of Structural Biology, **167**(1), pp. 47–54.
[18] Holten-Andersen, N., and Waite, J. H., 2008, "Mussel-Designed Protective Coatings for Compliant Substrates," J Dent Res, **87**(8), pp. 701–709.
[19] Valois, E., Hoffman, C., Demartini, D. G., and Waite, J. H., 2019, "The Thiol-Rich Interlayer in the Shell/Core Architecture of Mussel Byssal Threads," Langmuir, **35**(48), pp. 15985–15991.
[20] Holten-Andersen, N., Fantner, G. E., Hohlbauch, S., Waite, J. H., and Zok, F. W., 2007, "Protective Coatings on Extensible Biofibres," Nature Mater, **6**(9), pp. 669–672.
[21] Holten-Andersen, N., Slack, N., Zok, F., and Waite, J. H., 2005, "Nano-Mechanical Investigation of the Byssal Cuticle, a Protective Coating of a Bio-Elastomer," MRS Online Proceedings Library, **841**(1), p. R3.7/Y3.7.
[22] Monnier, C. A., DeMartini, D. G., and Waite, J. H., 2018, "Intertidal Exposure Favors the Soft-Studded Armor of Adaptive Mussel Coatings," Nature Communications, **9**(1), p. 3424.
[23] Zhang, X., Huang, Q., Deng, F., Huang, H., Wan, Q., Liu, M., and Wei, Y., 2017, "Mussel-Inspired Fabrication of Functional Materials and Their Environmental Applications: Progress and Prospects," Applied Materials Today, **7**, pp. 222–238.
[24] Holten-Andersen, N., Harrington, M. J., Birkedal, H., Lee, B. P., Messersmith, P. B., Lee, K. Y. C., and Waite, J. H., 2011, "PH-Induced Metal-Ligand Cross-Links Inspired by Mussel Yield Self-Healing Polymer Networks with near-Covalent Elastic Moduli," PNAS, **108**(7), pp. 2651–2655.
[25] Heepe, L., and Gorb, S. N., 2014, "Biologically Inspired Mushroom-Shaped Adhesive Microstructures," Annu. Rev. Mater. Res., **44**(1), pp. 173–203.
[26] Lin, Q., Gourdon, D., Sun, C., Holten-Andersen, N., Anderson, T. H., Waite, J. H., and Israelachvili, J. N., 2007, "Adhesion Mechanisms of the Mussel Foot Proteins Mfp-1 and Mfp-3," PNAS, **104**(10), pp. 3782–3786.
[27] Aksak, B., Sahin, K., and Sitti, M., 2014, "The Optimal Shape of Elastomer Mushroom-like Fibers for High and Robust Adhesion," Beilstein Journal of Nanotechnology, **5**(1), pp. 630–638.
[28] Carbone, G., and Pierro, E., 2012, "Sticky Bio-Inspired Micropillars: Finding the Best Shape," Small, **8**(9), pp. 1449–1454.
[29] del Campo, A., Greiner, C., and Arzt, E., 2007, "Contact Shape Controls Adhesion of Bioinspired Fibrillar Surfaces," Langmuir, **23**(20), pp. 10235–10243.
[30] Greiner, C., del Campo, A., and Arzt, E., 2007, "Adhesion of Bioinspired Micropatterned Surfaces: Effects of Pillar Radius, Aspect Ratio, and Preload," Langmuir, **23**(7), pp. 3495–3502.
[31] Hossfeld, C. K., Schneider, A. S., Arzt, E., and Frick, C. P., 2013, "Detachment Behavior of Mushroom-Shaped Fibrillar Adhesive Surfaces in Peel Testing," Langmuir, **29**(49), pp. 15394–15404.

[32] Kim, S., and Sitti, M., 2006, "Biologically Inspired Polymer Microfibers with Spatulate Tips as Repeatable Fibrillar Adhesives," Appl. Phys. Lett., **89**(26), p. 261911.
[33] Minsky, H. K., and Turner, K. T., 2015, "Achieving Enhanced and Tunable Adhesion via Composite Posts," Applied Physics Letters, **106**(20), p. 201604.
[34] Murphy, M. P., Aksak, B., and Sitti, M., 2009, "Gecko-Inspired Directional and Controllable Adhesion," Small, **5**(2), pp. 170–175.
[35] Gorb, S., Varenberg, M., Peressadko, A., and Tuma, J., 2007, "Biomimetic Mushroom-Shaped Fibrillar Adhesive Microstructure," Journal of The Royal Society Interface, **4**(13), pp. 271–275.
[36] Kim, T. K., Kim, J. K., and Jeong, O. C., 2011, "Measurement of Nonlinear Mechanical Properties of PDMS Elastomer," Microelectronic Engineering, **88**(8), pp. 1982–1985.
[37] Balijepalli, R. G., Begley, M. R., Fleck, N. A., McMeeking, R. M., and Arzt, E., 2016, "Numerical Simulation of the Edge Stress Singularity and the Adhesion Strength for Compliant Mushroom Fibrils Adhered to Rigid Substrates," International Journal of Solids and Structures, **85–86**, pp. 160–171.
[38] Spuskanyuk, A. V., McMeeking, R. M., Deshpande, V. S., and Arzt, E., 2008, "The Effect of Shape on the Adhesion of Fibrillar Surfaces," Acta Biomaterialia, **4**(6), pp. 1669–1676.
[39] Khaderi, S. N., Fleck, N. A., Arzt, E., and McMeeking, R. M., 2015, "Detachment of an Adhered Micropillar from a Dissimilar Substrate," Journal of the Mechanics and Physics of Solids, **75**, pp. 159–183.
[40] Afferrante, L., and Carbone, G., 2013, "The Mechanisms of Detachment of Mushroom-Shaped Micro-Pillars: From Defect Propagation to Membrane Peeling," Macromolecular Reaction Engineering, **7**(11), pp. 609–615.

Chapter 3. Suction-controlled detachment of mushroom-shaped adhesive structures

3.1 Introduction

This chapter serves as a continuation of the work presented in chapter 2. Through this work we aimed to further understand how other physical parameters affect the adhesion of bioinspired mushroom structures. Here, we explored how suction affects the adhesive performance of mushroom-shaped structures via experiments and modeling. The work presented here was conducted in collaboration with Jamie A. Booth who performed the modeling. This work was built on experimental techniques presented in chapter 2.

Fibrillar adhesives inspired by nature have long been studied for their superb adhesive properties in both reversible and permanent adhesion. Attachment structures and sizes utilized in nature range from nanoscale spatula tips observed in geckos, to macroscale spatula plaques used to permanently adhere by marine mussels [1–3]. Although the source of adhesion is different in the two systems, with geckos relying on intermolecular van der Waals forces [4] and marine mussels on chemical bonding [5], both of these systems appear to make use of mushroom-shaped geometries [5,6]. Studies of synthetic mushroom-shaped microstructures show improvements in the adhesion strength by factors as high as thirty times that of straight punches [7,8]. These improvements have led to the use of micropatterned surfaces in various applications, including climbing robots and in pick-and-place operations [9–11]. As previously mentioned, the high adhesion of these structures is the result of the mitigation of the severe stress concentration which occurs at the contact edge of a punch [7,12,13]. The inclusion of the thin flange at the tip has the effect of reducing strain energy at the contact edge and creating

a turning action which results in a compressive contribution to the stresses in this region. This leads to a preference for defect propagation from the center of the contact [14,15]. Mitigation of the contact edge stress concentration in mushroom-shaped structures has inspired other designs which harness similar effects, including those based on combining multiple materials [16–19] or using cupped tip geometries [20,21].

One effect not given significant attention in the modeling of mushroom-tipped structures is the role of suction. Many groups have sought to investigate this effect experimentally by reducing the atmospheric pressure under which mechanical testing is performed, without clear consensus. Henrey et al. reported no dependence on ambient atmospheric pressure for an array of microstructures with 17 μm tip diameter [22]. Likewise, Sameoto et al. reported little to no change in the pull-off force (defined as the maximum tensile load supported by the junction) with pressure for tip diameters of 16 μm or less [23]. However, a significant number of other studies have shown that pull-off force is lowered in a reduced pressure environment [24–27]. Heepe et al. showed that for an array of 50 μm diameter mushroom-tipped structures, the absence of suction led to a 10% reduction in the pull-off force [24]. Crucially, the authors also highlighted that the suction contribution was dependent on the retraction velocity and suggested this was the result of imperfect sealing of the defect which allowed for equalization of the pressure difference over longer loading times. Tinnemann et al. tested mushroom-shaped structures with tip diameter of 710 μm under various atmospheric pressures, and on rough and smooth surfaces [25]. It was shown that for structures adhered to smooth surfaces, reduction in the atmospheric pressure from 1000 mbar to 1 mbar lead to a 20% reduction in the pull-off force. On rough surfaces the effect was reduced to 6%,

hypothesized to be the result of improper sealing at the contact edge. Purtov et al. presented a study on similar sub-millimeter-scale structures which showed a reduction in pull-off force in the absence of suction of ~ 25% [26].

While it is difficult to draw absolute conclusions from the preceding literature given differences in the details of the fabrication processes, substrates, and measurement systems, there is evidence that suction may influence the strength of attachment in micropatterned adhesives utilizing mushroom-shaped microstructures under certain conditions. Furthermore, these studies have suggested that the suction contribution may scale with the mushroom tip size [23,25,26]. In this work, we aimed to investigate the role of suction in greater detail. We developed a model based upon linear elastic fracture mechanics to determine the strength of attachment of structures as a function of various system parameters, including the geometric and material properties, the adhesive strength of the interface, the ambient atmospheric pressure, and the initial interfacial defect size and trapped volume of air. This model was used to explain the results of experimental investigation of millimeter-scale elastomeric mushroom-shaped structures. Since the properties of these structures differ from others in the literature (larger length-scale, wider flanged tips), more general insights provided by the model are also explored.

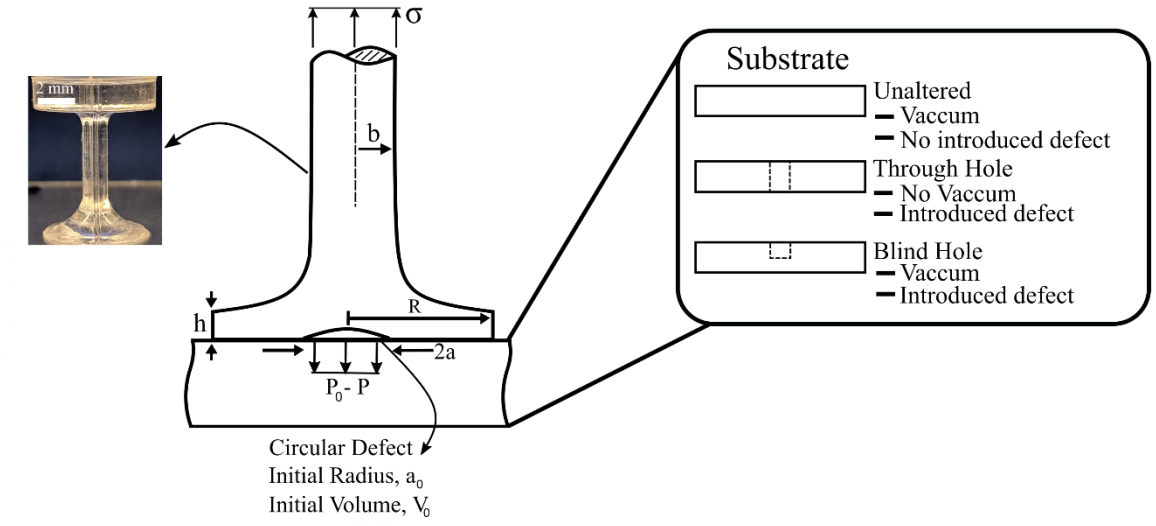

Figure 3.1: Schematic of the adhesive structure, substrate, and loading configuration. The geometric parameters of the structure are shown, along with the properties of the component material. The tractions on free surfaces of the structure are also shown, namely the applied stress, σ, and the net traction due to reduced pressure inside of the defect, $p_0 - p$.

Figure 3.1 is a schematic depiction of the system considered, encompassing both experimental and modeling efforts. Detachment is primarily associated with the propagation of a defect from the contact center, also depicted in the figure. If air is trapped in the defect as it propagates, and if the time scale of the detachment process is faster than those of leakage flow through asperities at the interface or permeation through the structure, then reduced pressure will develop in the defect. As illustrated in the figure, this results in a net tensile traction exerted on the structure inside of the defect, increasing the resistance to further

separation. Three substrate configurations were considered experimentally to assess the role of this suction effect on the attachment strength of the structure. In addition to an unaltered substrate, a sample with a through-hole was created. This was centered with respect to the stalk to eliminate the possibility of reduced pressure developing inside of the defect. Given that this hole could be viewed as a preexisting flaw in the contact, an additional control was considered with a blind hole of the same diameter and location.

3.2 Materials and Methods

3.2.1. Fabrication of structures

The bio-inspired structures were generated using the same methodology presented in chapter 2, section 2.2.1. For this study only structures casted at 90º were fabricated, and have the same parameters as those shown in Figure 2.1

3.2.2. Substrate preparation and bonding of structures

Before attachment of the mushroom-shaped structures, each substrate (borosilicate microscope slides, 25 mm × 75 mm) was etched using a Speedy 100 laser cutter (Trotec, Marchtrenk, Austria) to create a circular alignment marker at its center. To decouple the effects of suction and adhesion under defect propagation, three substrate configurations were fabricated (Figure 3.1). Both configurations with holes were created by drilling using a CNC mill (Sherline, Vista, CA) controlled with a microstepping controller (Flashcut CNC, Deerfield, IL). The diameter of each was 0.75 mm, with the blind hole drilled to a depth of 0.44 mm. The holes were centered with respect to the stalk. After the holes were drilled, the slides were cleaned with isopropanol to remove glass debris and other contaminants. Within

24 hours of thermally curing the PDMS structures, they were adhered to the substrate. The bonding process involved treatment of the PDMS structures and the microscope slides for 10 minutes in an UV-Ozone cleaner (PSD-UV6, Novascan, Boone, IA) to remove organic contaminants. Immediately following the ozone treatment, each structure was placed directly on a microscope slide with sufficient contact pressure to remove trapped air bubbles and form the adhesive bond. All structures were then mechanically tested within 3 hours of this bonding process.

3.2.3. Mechanical Testing

The synthetic structures were loaded to failure using a custom-built tensile tester with multi-camera imaging capabilities (Appendix A, Figure A.3). A Lebow Load Cell (Model 3108–10, 10-lb capacity Honeywell Sensing & Control, Charlotte, NC) with custom amplifying electronics is connected to a computer via a USB-mediated data acquisition (DAQ) module (DT9804, Measurement Computing, Norton, MA). Command of the stepper motor (ES22B, Parker CompuMotor, Irwin, PA) via an indexer controller (ZETA 6104, Parker CompuMotor, Irwin, PA), as well as acquisition of force and displacement data, was performed in LabVIEW (National Instruments, Austin, TX). The microscope slide and the adhered sample were placed on the stage and the center of the structure was aligned by eye to the center of the load cell (Appendix A, Figure A.3). The button at the free end of the sample was placed inside custom clamps and again centered by eye. The experiments were conducted under displacement control. The strain rate for all experiments presented was 0.004 s^{-1}, which was calculated by dividing crosshead velocity (2.5 mm/min) by the stalk length.

The deformation of the structure was recorded during each tensile test using a Canon Rebel SL2 with a Canon 100mm f/2.8 Macro USM fixed lens. This camera captured the structural deformation of the whole sample from a 'front view', at a rate of 30 frames per second (fps). Defect growth rates were determined by measuring the defect diameter in screenshots taken from these videos (Figure 3.2).

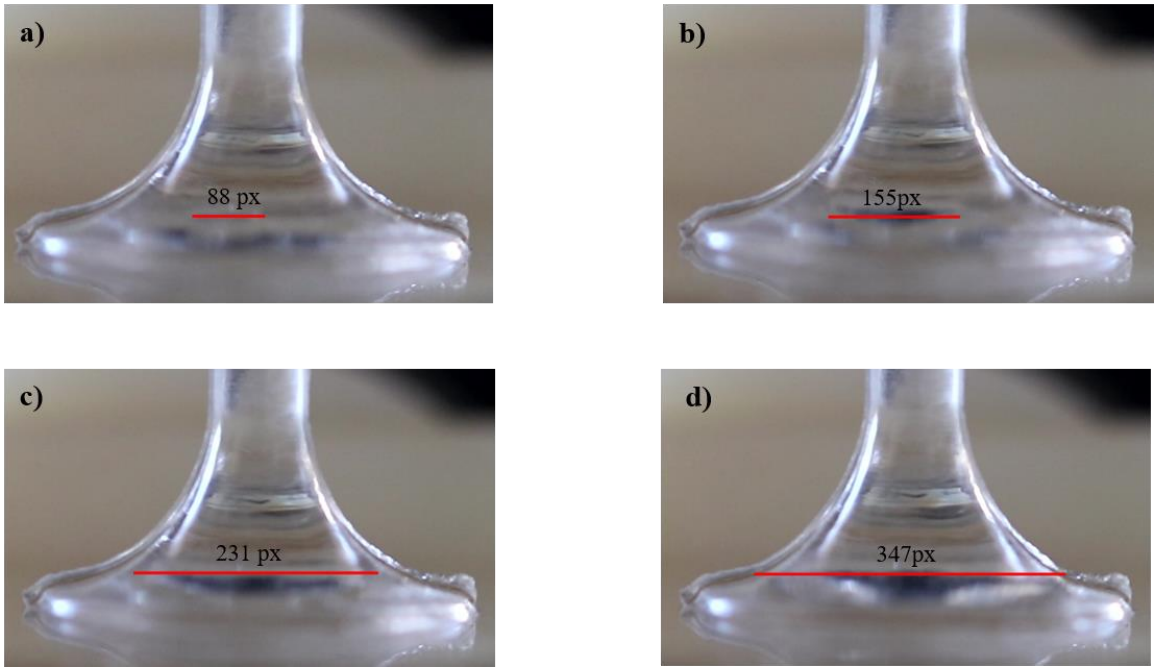

Figure 3.2: Front view camera screenshots used to determine defect growth rate by measuring the diameter at different time stamps in Fiji (ImageJ). The length of the red line in px is converted to mm (49 px/mm). Below we state the defect radius, a, for consistency with the modeling efforts of Section 3; (a) At time $t = 171\ s$, when the defect first becomes visible, $a = 0.9\ mm$; (b) At time $t = 178\ s$, $a = 1.6\ mm$; (c) At time $t = 183\ s$, $a = 2.4\ mm$; (d) At time $t = 205\ s$, as defect growth is arrested, $a = 3.5\ mm$.

To enable statistically-meaningful comparisons of the force-extension data collected with different samples and loading schemes, the distributions of forces and elongations at failure were compared using a pairwise Student's *t*-test implemented in MATLAB (Mathworks, Natick, MA).

3.3 Model

Returning to the schematic shown in Figure 3.1, we consider the defect to be penny-shaped with radius a, located at the center of the contact. The stalk has radius b, and the flanged tip has radius R. The thickness of the flanged tip is h. The fibril is subject to an applied tensile stress, σ. Prior to application of stress ($\sigma = 0$), the defect is considered to have initial volume V_o. As the applied stress is increased, deformation and eventual propagation of the defect cause the volume inside, V, to increase. If air is trapped within the defect as this occurs, then the absolute pressure inside the defect, p, will be reduced. Assuming that the initial trapped volume of air is at ambient atmospheric pressure, p_0, then the ideal gas law for the air in the defect provides

$$p = p_0 \frac{V_0}{V} \tag{1}$$

The net effect on the structure will be a tensile traction of magnitude $p_0 - p$, acting on the bottom surface of the tip over the cross-sectional area of the defect, as shown in Figure 3.1. In general, as the volume in the defect increases, the absolute pressure will be reduced, and the magnitude of this tensile traction will increase. We seek to introduce a model based on linear elastic fracture mechanics to examine how this suction effect influences defect growth, in

combination with the adhesive strength of the interface. The ultimate goal is to determine the maximum applied stress which can be supported by the structure prior to complete detachment.

3.3.1. Interfacial defect radius inside of the fibril stalk

In the limit that the defect radius is smaller than that of the fibril stalk, $a < b$, the analysis can be performed by approximating the fibril as a straight sided cylinder of radius b. Under the assumption of a frictionless interface, linear elastic fracture mechanics provides the solution for the stress intensity factor at the outer perimeter of the defect when subject to a remote tensile stress and a uniform traction on the defect surface, as [28]

$$K_{\mathrm{I}} = \frac{2}{\pi}(\sigma + p - p_0)\sqrt{\pi a} f\left(\frac{a}{b}\right) \tag{2}$$

where

$$f\left(\frac{a}{b}\right) = \frac{1 - \frac{1}{2}\frac{a}{b} + 0.148\left(\frac{a}{b}\right)^3}{\sqrt{1-\frac{a}{b}}} \tag{3}$$

Invoking eq. (1), the stress intensity factor can be rewritten in a dimensionless form as

$$\frac{K_{\mathrm{I}}}{p_0\sqrt{\pi b}} = \frac{2}{\pi}\left(\frac{\sigma}{p_0} + \frac{V_0}{V} - 1\right)\sqrt{\frac{a}{b}} f\left(\frac{a}{b}\right) \tag{4}$$

The volume of the defect is also given by linear elastic fracture mechanics as [28]

$$V = V_0 + \frac{8a^3}{3E^*}(\sigma + p - p_o) g\left(\frac{a}{b}\right) \tag{5}$$

where

$$g\left(\frac{a}{b}\right)=\frac{1}{\left(\frac{a}{b}\right)^3}\left[1.260\ln\left(\frac{1}{1-\frac{a}{b}}\right)-1.260\left(\frac{a}{b}\right)-0.630\left(\frac{a}{b}\right)^2+0.580\left(\frac{a}{b}\right)^3-0.315\left(\frac{a}{b}\right)^4-\right.$$

$$\left.0.102\left(\frac{a}{b}\right)^5+0.063\left(\frac{a}{b}\right)^6+0.093\left(\frac{a}{b}\right)^7-0.0081\left(\frac{a}{b}\right)^8\right] \quad (6)$$

and $E^*=E/(1-\nu^2)$, where E is the Young's modulus and ν the Poisson's ratio. Introducing eq. (1) we obtain a quadratic equation for the volume

$$\left(\frac{V}{V_0}\right)^2-\left[1+\frac{8}{3}\frac{p_0b^3}{E^*V_0}\left(\frac{\sigma}{p_0}-1\right)\left(\frac{a}{b}\right)^3 g\left(\frac{a}{b}\right)\right]\frac{V}{V_0}-\frac{8}{3}\frac{p_0b^3}{E^*V_0}\left(\frac{a}{b}\right)^3 g\left(\frac{a}{b}\right)=0 \quad (7)$$

the solution of which is

$$\frac{V}{V_0}=\frac{1}{2}+\frac{4}{3}\frac{p_0b^3}{E^*V_0}\left(\frac{\sigma}{p_0}-1\right)\left(\frac{a}{b}\right)^3 g\left(\frac{a}{b}\right)+$$

$$\frac{1}{2}\sqrt{\left[1+\frac{8}{3}\frac{p_0b^3}{E^*V_0}\left(\frac{\sigma}{p_0}-1\right)\left(\frac{a}{b}\right)^3 g\left(\frac{a}{b}\right)\right]^2+\frac{32}{3}\frac{p_0b^3}{E^*V_0}\left(\frac{a}{b}\right)^3 g\left(\frac{a}{b}\right)} \quad (8)$$

Defect growth occurs when the stress intensity factor reaches a critical value, characteristic of the strength of the adhesive bond at the interface, $K_{\mathrm{I}}=K_{\mathrm{c}}=\sqrt{2E^*W}$, where K_{c} is termed the interfacial toughness and W is the work of adhesion. In combination with eq. (4) and eq. (8), this condition can be used to solve for the corresponding critical stress $\sigma=\sigma_c$. For the results presented in Section 4.1, this was achieved numerically in MATLAB (Mathworks, Natick, MA).

A closed form solution for the critical stress is possible for the condition in which air is not sealed within the defect, or where the structure is placed in a vacuum environment. We refer to this situation as 'No Suction' (NS). In this case $p_0=0$, and

$$\sigma_c^{NS} = \frac{\pi}{2f\left(\frac{a}{b}\right)}\frac{K_c}{\sqrt{\pi a}} \tag{9}$$

or in terms of equivalent dimensionless parameters to those in eq. (4), as

$$\left(\frac{\sigma_c}{p_0}\right)_{NS} = \frac{\pi}{2f\left(\frac{a}{b}\right)}\sqrt{\frac{b}{a}}\left(\frac{K_c}{p_0\sqrt{\pi b}}\right) \tag{10}$$

3.3.2. Interfacial defect radius outside of the fibril stalk

In this case we assume that the mushroom flange is thin ($h \ll R$) and wide ($R \gg b$), and thus its deformation can be treated by Kirchhoff-Love plate theory. The deflection is therefore given by solution of the biharmonic equation for an axisymmetric system [29]. We establish a radial coordinate r, defined from the center of the contact. The boundary conditions are determined under the assumption that in comparison to the flange, the fibril stalk can be considered rigid. Consequently, the rotation of the section where the flange meets the stalk, and at the perimeter of the defect is assumed to be zero. The solution for the deflection due to the remote load, based on an applied shear force where the flange meets the stalk, is

$$w(r) = \frac{3\sigma_a b^4}{4E^* h^3\left[\left(\frac{a}{b}\right)^2 - 1\right]}\left\{\left[\left(\frac{a}{b}\right)^2 - 1\right]\left[\left(\frac{a}{b}\right)^2 - \left(\frac{r}{b}\right)^2\right] + 2\left(\frac{a}{b}\right)^2\left(\frac{r}{b}\right)^2 \ln\left(\frac{r}{a}\right) - 2\left(\frac{r}{b}\right)^2 \ln\left(\frac{r}{b}\right) + 2\left(\frac{a}{b}\right)^2 \ln\left(\frac{a}{b}\right) + 4\left(\frac{a}{b}\right)^2 \ln\left(\frac{a}{b}\right)\ln\left(\frac{r}{a}\right)\right\} \tag{11}$$

in the region $b \le r \le a$ and

$$w(b) = \frac{3\sigma b^4}{4E^* h^3\left[\left(\frac{a}{b}\right)^2 - 1\right]}\left\{\left[\left(\frac{a}{b}\right)^2 - 1\right]^2 - 4\left(\frac{a}{b}\right)^2 \ln\left(\frac{a}{b}\right)\ln\left(\frac{a}{b}\right)\right\} \tag{12}$$

in the region $0 \le r \le b$. In treating the pressure contribution, it is assumed that the volume in the defect is very large as compared to that which was initially trapped. As a result, we assume vacuum conditions have developed in the defect ($p = 0$). The tensile traction applied to the bottom surface of the structure inside of the defect is therefore p_0 (Figure 3.1). This enters the plate theory formulation as an applied shear force where the flange meets the stalk (associated with the tensile traction under the stalk) and a uniform distributed load on the region outside of the stalk to the perimeter of the defect. Together, these lead to the solution for deflection due to the tensile traction inside of the defect

$$w(r) = -\frac{3p_0 b^4}{16E^* h^3}\left\{\left(\frac{r}{b}\right)^4 - \left(\frac{a}{b}\right)^4 + 2\left[\left(\frac{a}{b}\right)^2 + 1\right]\left[\left(\frac{a}{b}\right)^2 - \left(\frac{r}{b}\right)^2\right] + 4\left(\frac{a}{b}\right)^2 \ln\left(\frac{r}{a}\right)\right\} \qquad (13)$$

in the region $b \le r \le a$ and

$$w(b) = -\frac{3p_0 b^4}{16E^* h^3}\left[\left(\frac{a}{b}\right)^4 - 1 - 4\left(\frac{a}{b}\right)^2 \ln\left(\frac{a}{b}\right)\right] \qquad (14)$$

in the region $0 \le r \le b$. To compute the strain energy, $U(\sigma, p_0)$ we first compute the result for σ alone and obtain

$$U(\sigma, 0) = \frac{3\sigma^2 \pi b^6}{8E^* h^3\left[\left(\frac{a}{b}\right)^2 - 1\right]}\left\{\left[\left(\frac{a}{b}\right)^2 - 1\right]^2 - 4\left(\frac{a}{b}\right)^2 \ln\left(\frac{a}{b}\right)\ln\left(\frac{a}{b}\right)\right\} \qquad (15)$$

Maintaining σ as fixed, the pressure p_0 is increased from zero. The increment of additional strain energy is given by

$$\mathrm{d}U = (\sigma - p_0)\pi b^2\left\{-\frac{3\mathrm{d}p_0 b^4}{16E^* h^3}\left[\left(\frac{a}{b}\right)^4 - 1 - 4\left(\frac{a}{b}\right)^2 \ln\left(\frac{a}{b}\right)\right]\right\} + \int_b^a \left(-\frac{3\mathrm{d}p_0 b^4}{16E^* h^3}\left\{\left(\frac{r}{b}\right)^4 - \left(\frac{a}{b}\right)^4 + 2\left[\left(\frac{a}{b}\right)^2 + 1\right]\left[\left(\frac{a}{b}\right)^2 - \left(\frac{r}{b}\right)^2\right] + 4\left(\frac{a}{b}\right)^2 \ln\left(\frac{r}{a}\right)\right\}\right)(-p_o)2\pi r\,\mathrm{d}r \qquad (16)$$

where the first term is associated with the region under the stalk, and the second term is associated with the region outside of the stalk to the perimeter of the defect. Integration over the outer region yields

$$\mathrm{d}U = -\frac{3\pi b^6}{16E^* h^3}\left[\left(\frac{a}{b}\right)^4 - 1 - 4\left(\frac{a}{b}\right)^2 \ln\left(\frac{a}{b}\right)\right]\sigma \mathrm{d}p_0 + \frac{\pi b^6}{16E^* h^3}\left[\left(\frac{a}{b}\right)^2 - 1\right]^3 p_0 \mathrm{d}p_0 \qquad (17)$$

Upon integration of the load parameters, this leads to

$$U(\sigma, p_0; a) = \frac{3\sigma^2 \pi b^6}{8E^* h^3}\left[\left(\frac{a}{b}\right)^2 - 1 - \frac{4\left(\frac{a}{b}\right)^2 \ln\left(\frac{a}{b}\right)\ln\left(\frac{a}{b}\right)}{\left(\frac{a}{b}\right)^2 - 1}\right] - \frac{3\sigma p_0 \pi b^6}{16E^* h^3}\left[\left(\frac{a}{b}\right)^4 - 1 - 4\left(\frac{a}{b}\right)^2 \ln\left(\frac{a}{b}\right)\right] +$$

$$\frac{{p_0}^2 \pi b^6}{32E^* h^3}\left[\left(\frac{a}{b}\right)^2 - 1\right]^3 \qquad (18)$$

The energy release rate is given by

$$\mathcal{G} = \frac{1}{2\pi a}\frac{\partial U(\sigma, p_0; a)}{\partial a} \qquad (19)$$

which, in combination with the result of (18), leads to

$$\mathcal{G} = \frac{3{p_0}^2 b^4}{8E^* h^3}\left\{\frac{\sigma}{p_0}\left[1 - \frac{2\ln\left(\frac{a}{b}\right)}{\left(\frac{a}{b}\right)^2 - 1}\right] - \frac{1}{2}\left[\left(\frac{a}{b}\right)^2 - 1\right]\right\}^2 \qquad (20)$$

Once again, defect growth is known to occur when the energy release rate attains a critical value characteristic of the strength of the adhesive bond at the interface, which in this case is the work of adhesion, $\mathcal{G} = W = {K_\mathrm{c}}^2/2E^*$. In combination with eq. (20), this condition can be used to solve for the corresponding critical stress $\sigma = \sigma_c$ as

$$\frac{\sigma_\mathrm{c}}{p_0} = \frac{\left(\frac{a}{b}\right)^2 - 1}{\left(\frac{a}{b}\right)^2 - 1 - 2\ln\left(\frac{a}{b}\right)}\left\{\frac{1}{2}\left[\left(\frac{a}{b}\right)^2 - 1\right] + \left(\frac{4\pi}{3}\right)^{\frac{1}{2}}\left(\frac{h}{b}\right)^{\frac{3}{2}}\frac{K_\mathrm{c}}{p_0\sqrt{\pi b}}\right\} \qquad (21)$$

In the situation in which air is not trapped within the defect, or equivalently the junction is formed in conditions of zero atmospheric pressure ($\boldsymbol{p_0 = 0}$), the critical stress will be

$$\boldsymbol{\sigma_c^{NS} = \frac{\left(\frac{a}{b}\right)^2 - 1}{\left(\frac{a}{b}\right)^2 - 1 - 2\ln\left(\frac{a}{b}\right)} \left(\frac{4\pi}{3}\right)^{\frac{1}{2}} \left(\frac{h}{b}\right)^{\frac{3}{2}} \frac{K_c}{\sqrt{\pi b}}} \quad \textbf{(22)}$$

This can be stated in an equivalent dimensionless form to eq. (21), as

$$\boldsymbol{\left(\frac{\sigma_c}{p_0}\right)_{NS} = \frac{\left(\frac{a}{b}\right)^2 - 1}{\left(\frac{a}{b}\right)^2 - 1 - 2\ln\left(\frac{a}{b}\right)} \left(\frac{4\pi}{3}\right)^{\frac{1}{2}} \left(\frac{h}{b}\right)^{\frac{3}{2}} \frac{K_c}{p_0\sqrt{\pi b}}} \quad \textbf{(23)}$$

3.4 Results and Discussion

3.4.1. Model

Figure 3.3 shows the normalized critical stress, σ_c/p_0, required to drive defect growth, as a function of the normalized defect radius, a/b, in both limits presented in Section 3. Three values of the dimensionless interface toughness parameter, $K_c/p_0\sqrt{\pi b}$, are considered. In the limit in which the defect is inside of the fibril stalk, three values of the dimensionless pressure parameter, $p_0 b^3/E^* V_0$ are considered (although the intermediate value is omitted for higher toughness to preserve clarity of the plot). In the limit that the defect is outside of the fibril stalk, we show the results with suction ($p_0 \neq 0$, eq. (21)) and without suction ($p_0 = 0$, eq. (23)), and consider a single value of the normalized flange thickness, $h/b = 0.1$.

The normalized critical stress is seen to increase with the pressure parameter, $p_0 b^3/E^* V_0$. This is a result of an enhancement of the suction effect introduced in Section 3. The tensile traction on the bottom of the structure inside of the defect (Figure 3.1), which results when the volume of air trapped within increases and the pressure is reduced, acts to pull

the defect closed. This allows for a higher magnitude of applied stress to be supported without defect growth. A larger tensile traction develops when the ambient atmospheric pressure, p_0, (outside of the defect) is high or the initial trapped volume in the defect, V_0, is small. Larger structures (increased b) and more compliant materials (reduced E^*) allow for greater increases in defect volume, greater reduction of the pressure inside the defect, and thus also a larger tensile traction.

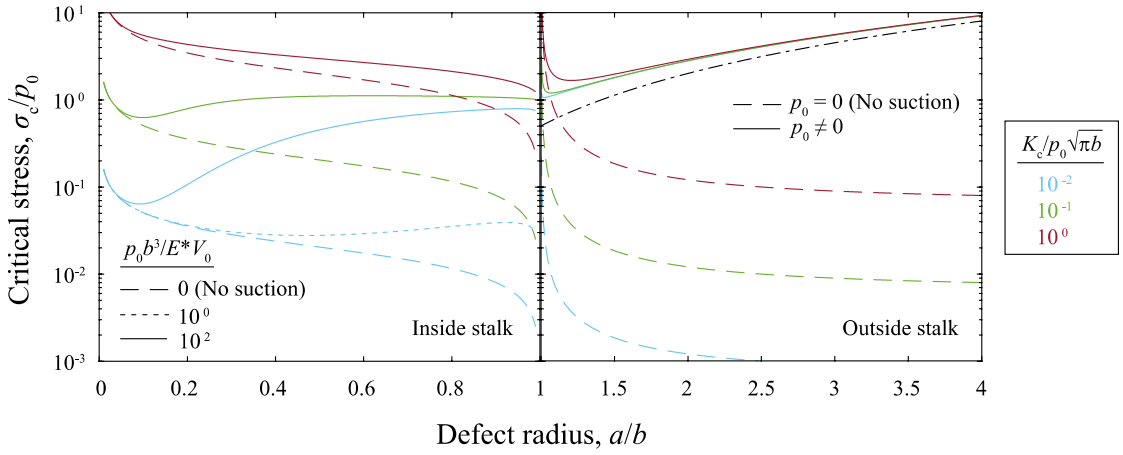

Figure 3.3: Normalized critical stress, σ_c/p_0, vs. normalized defect radius, a/b, for three values of the dimensionless interface toughness parameter, $K_c/p_0\sqrt{\pi b}$. The same results are shown without the effect of suction. Limiting behavior when the interfacial defect radius is inside (left) and outside (right) of the fibril stalk is shown. In the latter case, a single value of the normalized flange thickness, $h/b = 0.1$, is considered. The black dashed line (outside stalk) represents the limiting behavior of eq. (25).

Considering the behavior when the defect is inside of the stalk in greater detail, we observe a monotonic decay in the normalized critical stress with increasing defect size when interface toughness is high (e.g. for $K_c/p_0\sqrt{\pi b} = 1$). This indicates unstable defect propagation. The dominant effect during defect growth is an increase in the stress intensity at the defect perimeter associated with the remote applied stress. The high toughness renders the stresses required for defect growth higher than can be supported by tensile tractions inside of the defect due to the pressure difference alone. Consequently the critical stress is found to exceed the ambient pressure, $\sigma_c/p_0 > 1$, across the relevant range of defect radius. It is observed that the normalized critical stress is reduced as the toughness of the interface is reduced. A regime of stable defect growth may emerge, evidenced by an increase in the normalized critical stress with defect radius (e.g. for $K_c/p_0\sqrt{\pi b} = 0.01$ and $K_c/p_0\sqrt{\pi b} = 0.1$). In this case the dominant effect of defect growth is reduction of pressure inside of the defect. If the value of the parameter $p_0 b^3/E^* V_0$ is sufficiently high, the results asymptotically approach a critical stress equal to the ambient pressure, $\sigma_c/p_0 \to 1$, as the defect approaches the edge of the stalk. Under these conditions the absolute pressure inside of the defect is negligible ($p = 0$). Consequently, the tensile traction on the bottom surface of the structure due to the suction effect is maximized, being equal to the ambient atmospheric pressure, p_0. As the defect approaches the edge of the stalk, $a/b \to 1$, the applied stress is almost entirely supported by this tensile traction on the bottom of the structure.

At the point of transition between limiting behaviors, $\boldsymbol{a/b \rightarrow 1}$, the prediction of the critical stress from plate theory approaches infinity[1] . This unphysical result is a consequence of the absence of strain energy in the flange in this limit, as per eq. (15). In reality, as the defect passes through this region the stress will exhibit a smooth transition between the limits provided that the pressure in the defect, $\boldsymbol{p}$, is sufficiently close to zero (as is assumed in the plate theory formulation). If this is not the case (e.g. pale blue small dashed line) then the actual critical stress will be lower than the prediction of plate theory until the defect has grown sufficiently and the pressure inside is effectively zero.

Considering the behavior when the defect is outside of the stalk, we observe that in the absence of suction the critical stress continues to decrease monotonically. The defect propagation remains unstable, as it was inside of the stalk in this case. Consequently, the maximum value of applied stress (thus the strength of attachment of the structure in load control) will be attained prior to defect propagation, and thus controlled by the initial defect size.

In the presence of suction, the dominant effect when the defect is outside of the stalk is an increase in the critical stress with the defect radius. This behavior is simply the result of the recruitment of more area over which the tensile traction on the bottom of the structure, due to the suction effect, may act. It is observed that the behavior, with increasing defect radius,

[1]We note that Carbone *et al.* [14] erroneously use this artificial divergence to claim that a fibril can have infinite adhesion strength when the defect radius coincides with that of the stalk

approaches a limit independent of the toughness of the interface. It is therefore illustrative to consider the critical stress when interfacial bonding is negligible and suction dominates. When the toughness is zero, eq. (21) yields

$$\left(\frac{\sigma_c}{p_0}\right)_{K_c=0} = \frac{1}{2}\frac{\left[\left(\frac{a}{b}\right)^2-1\right]^2}{\left(\frac{a}{b}\right)^2-1-2\ln\left(\frac{a}{b}\right)} \tag{24}$$

In the limit that the defect is large, $\boldsymbol{a \gg b}$, we reach

$$\boldsymbol{\frac{\sigma_c}{p_0} = \frac{1}{2}\left(\frac{a}{b}\right)^2} \tag{25}$$

This result is shown as a black dashed line in Figure 2. This limiting case is quite significant, as it differs by a factor of 1/2 from the critical stress that is calculated by a simple balance of forces associated with the applied stress and the tensile traction on the bottom of the structure due to suction. Such an approach to approximate the suction contribution is suggested in ref. [15], and is revealed here to be an overestimate of the effect by 100%. Plate theory reveals the source of this discrepancy. When the shear force (per unit length) on the cross-section around the perimeter of the defect (i.e. at $\boldsymbol{r = a}$) is considered, we obtain

$$Q = \frac{\sigma b^2}{2a} - \frac{1}{2}p_0 a \tag{26}$$

When the critical stress is given by eq. (25), the shear force is therefore

$$Q = -\frac{1}{4}p_0 a \tag{27}$$

This negative shear implies that the interface supports compressive tractions outside of the defect. This compression of the flanged tip against the substrate supports half of the total load generated by the tensile tractions due to the suction effect, thus lowering the critical stress.

In summary, since the critical stress in the presence of suction is non-monotonic, the width of the tip will dictate whether the maximum value of critical stress is attained with the defect inside or outside of the stalk, and thus whether the presence of the flanged tip is of significance to the strength of the structure. If the tip is not wide relative to the stalk, then the maximum value of the critical stress is attained when the defect is under the stalk. By the time it reaches the flange, its propagation will be unstable. However, if the tip is wide, eventually the critical stress will be larger than that which was observed under the stalk. The maximum stress will be attained as the defect approaches the edge of the tip, thus the strength will be controlled by its width. Under these conditions, it is most advantageous to make the tip as wide as possible without violation of its structural integrity or other manufacturing constraints.

3.4.2. Comparison to experiment

Figure 3.4 shows representative force-extension curves for the different configurations described in Section 3.2.2. In all cases we observed an increase in force with increasing extension up until the onset of detachment, consistent with elastic deformation of the stalk. Table 3.1 shows the maximum force $F_{\max}$ and extension to failure $\Delta_{\max}$. Significance was assessed using pairwise Student's *t*-tests for the various slide configurations, $p < 0.05$. A full accounting of the results of the statistical analysis of these data are provided in table 3.2.

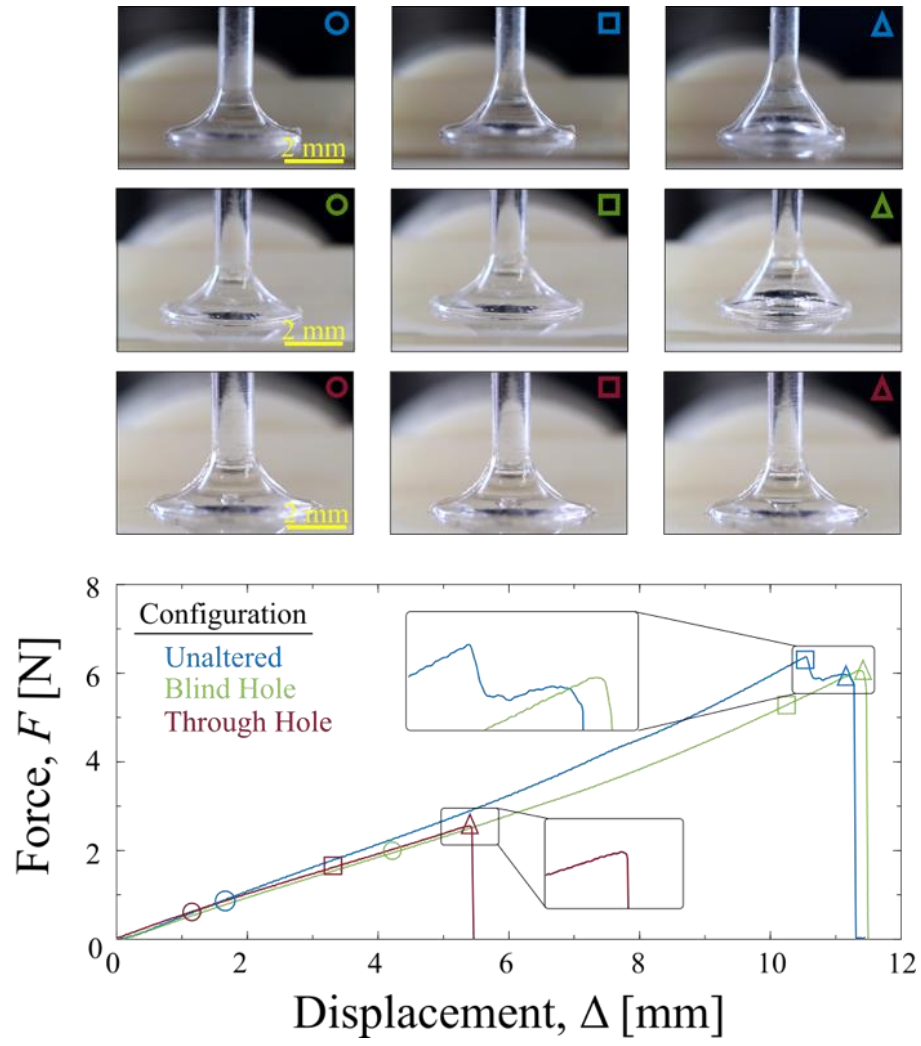

Figure 3.4: Representative force-displacement trace for structures adhered to each substrate configuration. The markers indicate time points at which images of the structures (above) were captured.

Table 3.1: Average maximum force (and associated standard deviation), and average maximum elongation (and associated standard deviation) measured experimentally. The number of experiments was between 10 and 14 per substrate configuration.

Substrate configuration	**Average maximum force F_{max} [N]**	**Average maximum elongation Δ_{max} [mm]**
Unaltered	6.88 ± 1.56	10.74 ± 1.16
Blind hole	5.94 ± 1.76	10.11 ± 1.94
Through-hole	2.50 ± 0.42	4.73 ± 1.94

Table 3.2: Results of the Student's t-test analysis of the maximum force for pairs of loading configurations. The h-value is binary with 1 indicating statistical significance at the 95% confidence level (which corresponds to a p-value of 0.05).

Pairs of Loading Configuration	**Force**		**Elongation**	
	***h*-value**	***p*-value**	***h*-value**	***p*-value**
Unaltered & Blind Hole	0	0.118	0	0.3205
Unaltered & Through Hole	1	1.147×10^{-13}	1	1.940×10^{-15}
Blind Hole & Through Hole	1	3.937×10^{-7}	1	3.517×10^{-9}

The maximum force and extension to failure were largest for structures adhered to unaltered glass slides, or slides with a blind hole. The difference in these two cases was not statistically significant, suggesting that the presence of the hole alone does not control the strength of attachment. By contrast, structures adhered to glass slides with a through-hole,

designed to prevent the trapping of air within the defect, exhibited a significant drop in the maximum force. The reduction, as compared to the other two cases, is on the order of 60%. Alternatively, suction can be viewed as providing an enhancement of the maximum force on the order of ~ 150%.

In order to compare the results to the model presented, it was first necessary to consider the nature of defect propagation and the defect size at which the maximum load was observed. Figure 3.4 also shows snapshot images of the loaded structures at various stages of structure-substrate separation.

In the cases of an anticipated suction contribution, for the unaltered substrate (Figure 3.4, blue images) and blind hole substrate (Figure 3.4, green images), a defect at the center of the contact begun to propagate at a critical load and grew stably. Specifically, for the unaltered substrate, initiation occurred at a load of ~ 3N. The defect was then observed to grow at a constant rate of 0.16 ± 0.02 mm/s, passing the edge where the stalk meets the flange; we denote this as Regime 1. At a load of ~ 5N, when the defect extends outside of the stalk, the defect growth rate slowed considerably to a value of 0.051 ± 0.003 mm/s; we denote this as Regime 2. When load reaches ~ 6N (i.e. at the point of approximately maximal load) the defect grew rapidly toward the edge of the tip. As the defect reached the edge, a cupping effect was observed consistent with flange deformation. In this regime, it wasn't not possible to accurately measure the defect growth rate. Flange deformation was followed by the final detachment of the structure from the substrate. Results for the defect growth rate obtained from measurements of three additional structures are included in the Table 3.3.

Table 3.3: Defect growth rate for the unaltered substrate in regimes 1 and 2 (as defined in the body of the manuscript), and the associated standard deviation.

Sample Number	Regime 1 rate [mm/s]	Regime 2 rate [mm/s]
1	0.16 ± 0.01	0.051 ± 0.003
2	0.24 ± 0.02	0.100 ± 0.007
3	0.25 ± 0.03	0.031 ± 0.002
4	0.30 ± 0.01	0.053 ± 0.002

The slowing of the defect growth in the flange region is evidence of an increase in the critical stress, which was predicted in the preceding model when suction was present and the defect was outside of the stalk. This suggests that the overall strength will be controlled by the tip radius, R. Experimental observations of the radius of the defect at the point of maximum load, $a_{\max}$, suggest that the ratio $a_{\max}/b > 3$. This is approaching the tip-stalk ratio, $R/b = 4$. Further evidence of the critical role played by the radius of the tip is the observation that the experimental results appear independent of the initial defect size. There is minimal difference in the maximum force supported by the unaltered substrate (with no perceptible initial defect) and the blind hole substrate (with the hole representing a well-characterized initial defect size).

When the defect is far outside of the stalk and a suction effect is present, the preceding model suggests that the strength is approximately independent of the toughness of the interface and is thus well approximated by eq. (25). Using the tip radius as an estimate of the defect size at maximum load, $a_{\max}/b = 4$, in combination with the result of eq. (25) we obtain an estimate of the strength of the attachment $\sigma_{\max} \sim 900$ kPa or $F_{\max} \sim 6.4$ N. This is in excellent

agreement with the experimental observations, and suggests that the strength is indeed controlled by the width of the flange relative to the stalk. It should be emphasized that this is the maximum value of the applied stress as defined in Figure 3.3 and utilized in the model described in Section 3.3, which implicitly assumes normalization of the maximum applied force with respect to the cross-sectional area of the stalk. If instead the maximum applied force is normalized with respect to the projected area of the contact at the tip then we obtain a strength of attachment of ~ 50 kPa.

In the case of the through-hole substrate, without the possibility of a suction contribution, different defect propagation behavior was observed (Figure 3.4, red images). A center defect was observed to start growing at a load of ~ 2.5 N. Unsurprisingly, this is similar to the critical load for defect growth initiation in cases where a suction effect is possible, as suction cannot play a role until significant defect growth occurs. Unlike the other cases, once the defect begun to grow it propagated rapidly and the structure detached completely (without arrest in the flange region). This is also consistent with the model presented, which predicts a monotonic reduction in the critical stress (and thus unstable propagation) in the absence of suction.

3.4.3. Comparison to existing literature

The suction effect observed in the current study was considerably larger than in the existing literature (60% vs. < 25% [22–27]). There are two primary differences in the structures studied here. The first is the overall scale, being on the order of millimeters as compared to sub-millimeter [25,26] or micron [22–24,27]. The second was that the width of the flanged tip is considerably larger relative to the stalk than in previous studies (tip-stalk ratio of 4 vs. < 2

[22–27]). The model presented has revealed that the strength of attachment of the structures studied here is dominated by the tip-stalk ratio, via eq. (25), hence it is the latter of the two differences which is primarily responsible for the difference observed.

The role played by the overall scale of the structures, while secondary here, may be more significant when the tip-stalk ratio is small. In this case the model presented predicts the strength will be controlled by behavior of the defect when it is inside of the stalk radius. In this regime, increases in the parameter $\boldsymbol{p_0 b^3 / E^* V_0}$ were seen to correspond to an increase in the suction effect. Fibrils with larger stalk radius, $\boldsymbol{b}$, accommodate a greater volume change in the defect at an equivalent applied stress, thus a greater reduction in pressure within the defect. This is in agreement with general trends observed in the literature for small tip-stalk ratios [22–27], but detailed conclusions about this scaling will require examination of suction while systematically varying structure size.

3.5 References

[1] Desmond, K. W., Zacchia, N. A., Waite, J. H., and Valentine, M. T., 2015, "Dynamics of Mussel Plaque Detachment," Soft Matter, **11**(34), pp. 6832–6839.

[2] Autumn, K., and Peattie, A. M., 2002, "Mechanisms of Adhesion in Geckos," Integrative and Comparative Biology, **42**(6), pp. 1081–1090.

[3] Gorb, S. N., and Varenberg, M., 2007, "Mushroom-Shaped Geometry of Contact Elements in Biological Adhesive Systems," Adhesion Science and Technology, **21**(12–13), pp. 1175–1183.

[4] Autumn, K., Sitti, M., Liang, Y. A., Peattie, A. M., Hansen, W. R., Sponberg, S., Kenny, T. W., Fearing, R., Israelachvili, J. N., and Full, R. J., 2002, "Evidence for van Der Waals Adhesion in Gecko Setae," PNAS, **99**(19), pp. 12252–12256.

[5] Waite, J. H., 2017, "Mussel Adhesion – Essential Footwork," J of Experimental Biology, **220**(4), pp. 517–530.

[6] Autumn, K., Niewiarowski, P. H., and Puthoff, J. B., 2014, "Gecko Adhesion as a Model System for Integrative Biology, Interdisciplinary Science, and Bioinspired Engineering," Annual Review of Ecology, Evolution, and Systems, **45**(1), pp. 445–470.

[7] Spuskanyuk, A. V., McMeeking, R. M., Deshpande, V. S., and Arzt, E., 2008, "The Effect of Shape on the Adhesion of Fibrillar Surfaces," Acta Biomaterialia, **4**(6), pp. 1669–1676.

[8] del Campo, A., Greiner, C., and Arzt, E., 2007, "Contact Shape Controls Adhesion of Bioinspired Fibrillar Surfaces," Langmuir, **23**(20), pp. 10235–10243.

[9] Heepe, L., and Gorb, S. N., 2014, "Biologically Inspired Mushroom-Shaped Adhesive Microstructures," Annu. Rev. Mater. Res., **44**(1), pp. 173–203.

[10] Li, Y., Krahn, J., and Menon, C., 2016, "Bioinspired Dry Adhesive Materials and Their Application in Robotics: A Review," J Bionic Eng, **13**(2), pp. 181–199.

[11] Hensel, R., Moh, K., and Arzt, E., 2018, "Engineering Micropatterned Dry Adhesives: From Contact Theory to Handling Applications," Advanced Functional Materials, **28**(28), p. 1800865.

[12] Khaderi, S. N., Fleck, N. A., Arzt, E., and McMeeking, R. M., 2015, "Detachment of an Adhered Micropillar from a Dissimilar Substrate," Journal of the Mechanics and Physics of Solids, **75**, pp. 159–183.

[13] Balijepalli, R. G., Begley, M. R., Fleck, N. A., McMeeking, R. M., and Arzt, E., 2016, "Numerical Simulation of the Edge Stress Singularity and the Adhesion Strength for Compliant Mushroom Fibrils Adhered to Rigid Substrates," International Journal of Solids and Structures, **85–86**, pp. 160–171.

[14] Carbone, G., Pierro, E., and Gorb, S. N., 2011, "Origin of the Superior Adhesive Performance of Mushroom-Shaped Microstructured Surfaces," Soft Matter, **7**(12), pp. 5545–5552.

[15] Afferrante, L., and Carbone, G., 2013, "The Mechanisms of Detachment of Mushroom-Shaped Micro-Pillars: From Defect Propagation to Membrane Peeling," Macromolecular Reaction Engineering, **7**(11), pp. 609–615.

[16] Minsky, H. K., and Turner, K. T., 2015, "Achieving Enhanced and Tunable Adhesion via Composite Posts," Applied Physics Letters, **106**(20), p. 201604.

[17] Minsky, H. K., and Turner, K. T., 2017, “Composite Microposts with High Dry Adhesion Strength,” ACS Appl. Mater. Interfaces, **9**(21), pp. 18322–18327.
[18] Fischer, S. C. L., Arzt, E., and Hensel, R., 2017, “Composite Pillars with a Tunable Interface for Adhesion to Rough Substrates,” ACS Applied Materials & Interfaces, **9**(1), pp. 1036–1044.
[19] Bae, W. G., Kim, D., Kwak, M. K., Ha, L., Kang, S. M., and Suh, K. Y., 2013, “Enhanced Skin Adhesive Patch with Modulus-Tunable Composite Micropillars,” Advanced Healthcare Materials, **2**(1), pp. 109–113.
[20] Fischer, S. C. L., Groß, K., Abad, O. T., Becker, M. M., Park, E., Hensel, R., and Arzt, E., 2017, “Funnel-Shaped Microstructures for Strong Reversible Adhesion,” Advanced Materials Interfaces, **4**(20), p. 1700292.
[21] Wang, Y., Kang, V., Arzt, E., Federle, W., and Hensel, R., 2019, “Strong Wet and Dry Adhesion by Cupped Microstructures,” ACS Appl. Mater. Interfaces, **11**(29), pp. 26483–26490.
[22] Henrey, M., Díaz Téllez, J. P., Wormnes, K., Pambaguian, L., and Menon, C., 2013, “Towards the Use of Mushroom-Capped Dry Adhesives in Outer Space: Effects of Low Pressure and Temperature on Adhesion Strength,” Aerospace Science and Technology, **29**(1), pp. 185–190.
[23] Sameoto, D., Sharif, H., and Menon, C., 2012, “Investigation of Low-Pressure Adhesion Performance of Mushroom Shaped Biomimetic Dry Adhesives,” Journal of Adhesion Science and Technology, **26**(23), pp. 2641–2652.
[24] Heepe, L., Varenberg, M., Itovich, Y., and Gorb, S. N., 2011, “Suction Component in Adhesion of Mushroom-Shaped Microstructure,” Journal of The Royal Society Interface, **8**(57), pp. 585–589.
[25] Tinnemann, V., Hernández, L., Fischer, S. C. L., Arzt, E., Bennewitz, R., and Hensel, R., 2019, “In Situ Observation Reveals Local Detachment Mechanisms and Suction Effects in Micropatterned Adhesives,” Advanced Functional Materials, **29**(14), p. 1807713.
[26] Purtov, J., Frensemeier, M., and Kroner, E., 2015, “Switchable Adhesion in Vacuum Using Bio-Inspired Dry Adhesives,” ACS Appl. Mater. Interfaces, **7**(43), pp. 24127–24135.
[27] Davies, J., Haq, S., Hawke, T., and Sargent, J. P., 2009, “A Practical Approach to the Development of a Synthetic Gecko Tape,” International Journal of Adhesion and Adhesives, **29**(4), pp. 380–390.
[28] Tada, H., Paris, P. C., and Irwin, G. R., 2000, The Stress Analysis of Cracks Handbook, Third Edition, ASME, NY.
[29] Timoshenko, S., and Woinowsky-Krieger, S., 1959, Theory of Plates and Shells, McGraw-Hill, NY.

Chapter 4. Viscoelastic analysis of mussel distal threads

4.1 Introduction

Mussel byssal threads are essentially "fast" mini-tendons formed in 1-5 min and immediately recruited into load-bearing service [1–3]. Similar to vertebrate tendons, byssal distal threads are highly anisotropic with parallel staggered arrays of collagens organized as bundles [4–6]. Although byssal threads exhibit strength and modulus comparable with tendon, they extend nearly 10-fold more than tendon [6–10]. Such deformability endows threads with impressive hysteresis and toughness, which, at ~45 MJ/m^3, is comparable to that of Kevlar (Table 4.1)[8] [6,10,11]. In addition, threads can recover their mechanical properties after undergoing yield, whereas tendon damage requires cell-mediated repair [2,5,10]. The high toughness and hysteresis properties indicate that these threads utilize adaptive mechanisms to dissipate energy not possible in typical tendons.

Table 4.1: Comparison of some mechanical properties of byssal distal thread with those of tendon and Kevlar ®.

Material	Modulus [GPa]	Strength [GPa]	Extensibility [mm/mm]	Hysteresis [%]	Toughness [MJ/m^3]
Distal thread	0.9	0.08	1.10	72	45
Collagen (tendon)	1.2	0.12	0.13	10	6
Kevlar®	130	3.60	0.03	nd	50

Many of the mechanical properties of byssal threads have been credited to their hierarchical composite assembly (Figure 1.7) [2,4,5,12–16]. Individual threads are composed of a proximal region, which typically lies within the shell of the mussel, and the distal region, which extends from the shell to the plaque. The fibrous core of the distal thread (diameter ~150 μm) is encapsulated by a stiff outer cuticle (thickness≤5 μm) [17–19]. The core is composed of a network of complex, collagenous, multi-domain, proteins named preCols that resemble pentablock copolymers. The preCols assemble in 6 + 1 bundles which, in turn, come together to form highly ordered fibrils that are orientated parallel to the long axis of the thread [4,5,12,15,20]. preCols have three distinct protein domains that are organized quasi-symmetrically. Starting at the N- terminus, the organization is as follows: an unstructured histidine (His)-rich N-terminus, an alanine/glycine-rich silk-like domain, a kinked central collagen core, an alanine-rich silk-like domain, and finally another unstructured His-rich domain at the C-terminus.

Numerous studies have been conducted on mussel distal threads focused around the materials' elastic response [2,8–10,21–23] . Based on these studies, several energy dissipative mechanisms have been proposed. One of the postulated mechanisms is that energy is dissipated via the breaking of metal coordinate crosslinks in the His-rich domains as the threads are loaded [2,10]. Another proposed mechanism is that the polyalanine and polyglycine β-sheets contained in silk-like domains unfold and reorient during the yielding phase, further contributing to energy dissipation [13]. Although these studies have shed light on many of the thread's mechanical properties, they fail to account for viscoelastic effects in the material [7,24]. Understanding their viscoelastic properties is imperative as energy dissipation is

dominated by viscous processes, which are poorly understood in distal threads. Here, we propose that by studying the viscoelastic response of distal threads a better understanding will be developed of how this composite biomaterial utilizes diverse protein domains flanking the collagen core to dissipate energy.

When held at a constant strain, nearly all polymers (natural and synthetic) experience a decrease in stress over time through a process known as stress relaxation. During this process, energy is typically released as polymer chains are untangled and/or slide past one another [25]. Through stress relaxation experiments we sought to dissect the contribution of each domain to the relaxation response and to identify which energy dissipating mechanisms are incurred during the process. To test this, we perturbed different domains *via* chemical treatments and observed changes in the relaxation behavior. Stress relaxation experiments were coupled with *in situ tensile* Small Angle X-Ray Scattering (SAXS) to shed light on the effects of the various treatments on molecular spacing and hence on viscous processes incurred during relaxation.

Due to the micro-geometry of the distal threads, conducting dynamic analysis has been challenging. Work by Aldred *et al*. on *Mytilus edulis* distal threads revealed the glass transition temperature and storage modulus for relevant ecological temperatures [7]. In a different study it was observed that, with a static load of .046 N, as the frequency of oscillations increased energy dissipation also increased [24]. Although these studies provide insight into the dynamic response of byssal threads, it is still unclear at which frequency distal threads dissipate maximum energy. To provide a constitutive model, in the present work, a generalized Maxwell viscoelastic model was used to analyze stress relaxation data and mathematically derive the material's viscoelastic parameters (Figure 4.1). Using the material's viscoelastic parameters,

we estimated the storage and loss moduli. This in turn allowed us to determine the relative degree of damping in the material and the frequency at which maximum damping occurs. Beyond revealing quantitative information about the distal thread's material parameters, this model provides insights into how the different domains may be responding in a manner resembling that of a spring (elastic components) or damper (viscous components).

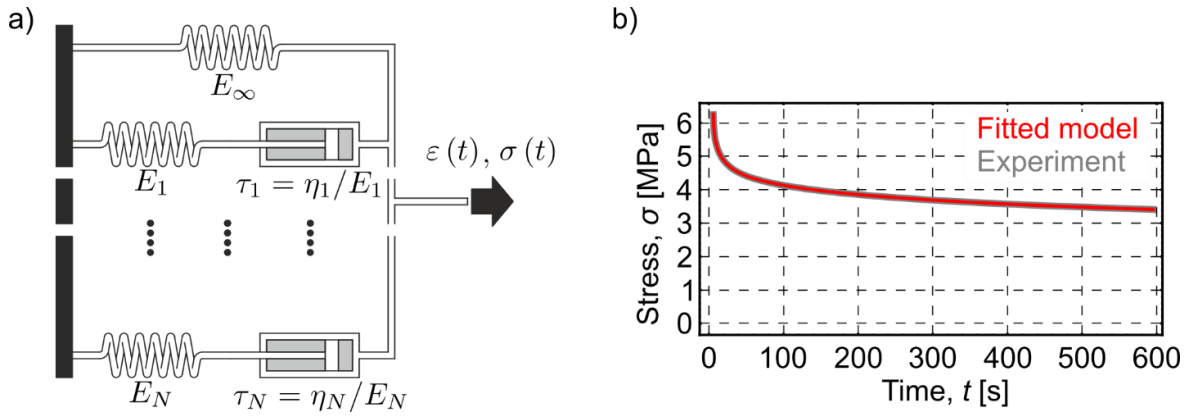

Figure 4.1: Maxwell model diagram and fitting results. a) Representative schematic of the generalized Maxwell model: N represents the number of maxwell elements, E_∞ denotes the long-term elastic modulus, E_i is the value for the elastic modulus for the springs in the Maxwell elements, and η_i is the linear viscosity parameter for individual dashpots. b) Illustration of the fitting accuracy of the 5th-order generalized Maxwell model for a native thread.

4.2 Methods and Materials

4.2.1 Reagents

Sodium acetate and sodium phosphate were obtained from Sigma Aldrich (St. Louis, MO). Urea and ethylenediamine tetraacetic acid (EDTA) were obtained from Fisher Scientific (Pittsburgh, PA).

4.2.2 Thread Collection

Mussels *Mytilus californianus* were collected from Goleta Pier near Santa Barbara, CA and stored in maricultural tanks with an open seawater circulation system. Individual mussels were secured onto glass plates with the use of rubber bands overnight, this prevented the mussels from moving and allowed them to deposit byssus onto the glass surface. Threads were removed within 48 hours of plating and mechanically tested within 72 hours. The proximal region of the threads was removed using a razor blade. Threads were stored in seawater filtered through a 0.22µm filter.

4.2.3 Chemical Treatments

In native conditions, distal threads were collected and stored in filtered seawater. For threads exposed only to pH changes, threads were immersed in buffered solutions (100 mM acetate, 100 mM phosphate) at pH = 5.5, 6.5, and 7.5 for a minimum of 24 hours prior to testing. Buffers used for urea treatment were freshly prepared at pH = 5.5, 6.5 and 7.5 with 100 mM acetate and 100mM phosphate and supplemented with 8M urea. EDTA treatment buffers were prepared in the same manner as previously stated but substituting 100mM EDTA for urea. Samples treated in their respective buffer were submerged for a minimum of 24 hours prior to testing.

4.2.4 Stress Relaxation Measurements

Stress relaxation experiments were conducted on a tabletop tensile tester (Bionix 200 universal testing machine, MTS, Eden Prairie, MN), at a nominal strain rate of 1.0 min^{-1} using a 10 N load cell and a built-in optical encoder to measure the load and displacement. All mechanical tests were performed with the distal threads fully submerged in seawater inside the Bionix 200 environmental chamber. The two ends of the threads were secured with custom-built clamps and aligned by eye on the tensile tester. Once the threads were secured, initial thread lengths were measured with a digital caliper (ABS Digimatic Caliper, Mitutoyo, Kanagawa, Japan) and recorded. All threads were pulled to a strain of 10% and held at this strain for 5-10 minutes. Force, extension, and time were recorded during the duration the test. Representative stress relaxation curves are shown in the Figure 4.2.

Relaxation percentage (R %) was calculated by subtracting the force after 5 minutes of loading ($F_{t\,=\,5min}$) from the initial force when the sample was first strained to 10% ($F_{t\,=\,0}$) and dividing by the initial force eq.(4.1).

$$R\,\% = \frac{F_{t\,=\,0} - F_{t\,=\,5min}}{F_{t\,=\,0}} \tag{4.1}$$

To enable statistically meaningful comparisons of the relaxation for the various treatments, the distribution of relaxations were compared using a pairwise Student's t-test implemented in MATLAB (Mathworks, Natick, MA).

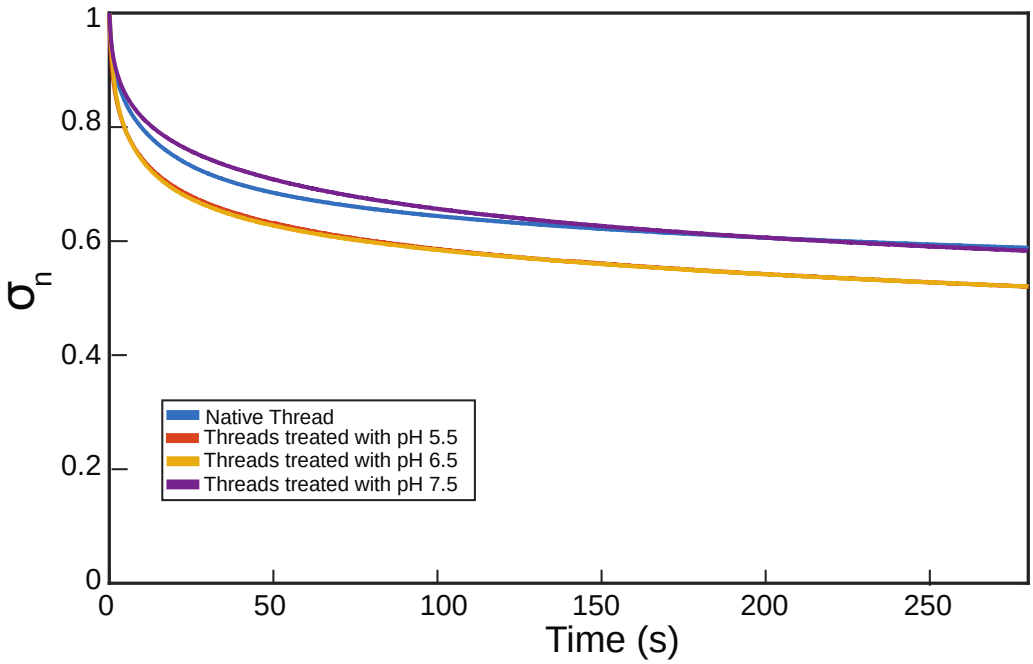

Figure 4.2: Representative normalized stress relaxation plot with stress response over time. All threads were strained to 10% and held at this strain for 5-10min, while the force was recorded. The stress was normalized by dividing all values by the maximum value of the stress.

4.2.5 SAXS Measurements

SAXS measurements were conducted at the BioSAXS beam line 4-2 at the Stanford Synchrotron Radiation Lightsource (SSRL) (Menlo Park,CA). Measurements were performed with a wavelength of 1 Å and a beam size of 100 µm X 100 µm. Diffraction patterns were acquired with the 2D CCD detector Rayonix225HE (Rayonix Inc., Evanston, IL) with an array of 3072 X 3072 pixels and pixel size of 73 µm. Two different experiments were conducted with detector center-to-sample- distances of 1186 mm and 1215 mm, and calibrations were done using a silver behenate (AgBeh) standard.

All threads were kept submerged in their appropriate conditions for a minimum of 24 hours prior to testing and pulled in a custom-built micromechanical tensile tester (Appendix B, Figure B.1). Thread ends were first secured with a hex key in the custom-built tester clamps and aligned by eye. Once positioned, the thread length was measured using a digital caliper (ABS Digimatic Caliper, Mitutoyo, Kanagawa, Japan) and recorded. Before measurements were conducted threads were hydrated with a drop of water. A single SAXS image was acquired for each sample prior to being pulled to serve as a baseline. Threads were then pulled to 10% strain, and extensions were measured by a micrometer head that is attached to the custom-built tester (Micrometer Head MHS, Mitutoyo, Kanagawa, Japan) (Appendix B, Figure B.1). Samples were held at a strain of 10% between 5-10 min, during which SAXS images were acquired every 20 seconds.

The 2D SAXS patterns were analyzed with a custom-built MATLAB function (Mathworks, Natick, MA). The SAXS reflection peaks values were averaged in the meridional and equatorial directions. The 1D equatorial intensities (q_e) empty beam background and

variations were removed using exponentially decaying functions. No fits were necessary for the meridional reflections due to the sharp peaks (Figure 4.3). The 1D equatorial intensities were fitted with a sum of Gaussian curves. Peak positions were represented by q_m and q_e which are inversely correlated with the corresponding *D*-spacing, $D = \frac{2\pi}{q}$ and has units of nm. The molecular strain was determined as follows:

$$\varepsilon_{m,q} = \frac{D(t=0) - D(t)}{D(t=0)} \times 100\% \quad (4.2)$$

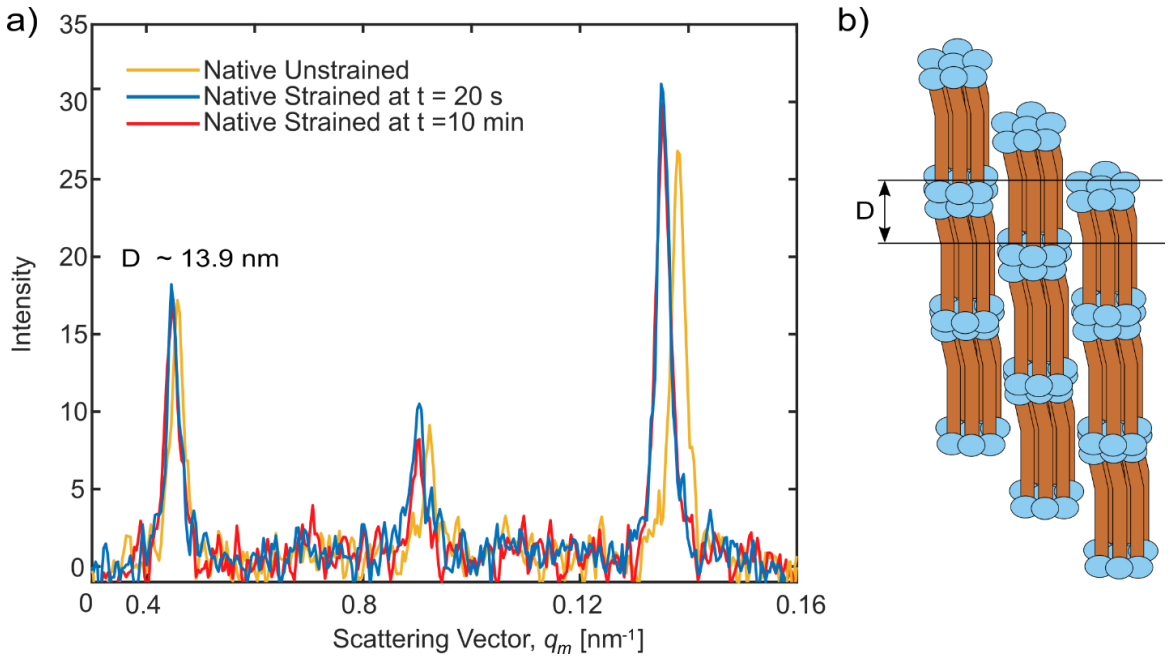

Figure 4.3: SAXS meridional scattering of mussel distal threads. a) Integration of the peak intensity of the meridional peaks for a native thread prior to straining, at t = 20 seconds after initial 10% strain, and at t = 10 min held at the constant strain of 10%. b) Representative axial staggering of the preCol bundles, D represents the axial staggering length captured from the integration of peak intensity; this value repeats every ~13.9 nm.

4.2.6 Modeling the Stress Relaxation

To characterize the stress relaxation phenomenon observed in the uniaxial tensile relaxation test we used the generalized Maxwell model, which is depicted in Figure 4.1. The one-dimensional representation of the model consists of $N+1$ linear springs and N linear dashpot elements, where N (positive integer) represents the model order. The long-term behavior (*i.e.* the response in infinitely slow loading rate or after infinite waiting time) of the model is described by the elastic modulus E_∞ of the spring in the network having no dashpot element. The other networks ($i = 1 \ldots N$) contain springs with elastic modulus E_i and dashpots with linear viscosity η_i. Parameter τ_i was introduced for simplicity.

The first part of the prescribed strain history in the relaxation experiments was a ramp loading, where the sample was deformed from its undeformed configuration until the desired strain ε_0 during time t_0. After t_0, the strain was kept constant. Thus, the strain history is defined as

$$\varepsilon(t) = \begin{cases} \dot{\varepsilon} \cdot t & t \le t_0 \\ \varepsilon_0 & t > t_0 \end{cases}. \tag{4.3}$$

The resulting stress solutions are

$$\sigma(t) = \begin{cases} E_\infty \dot{\varepsilon} t + \sum_{i=1}^{N} (1 - \exp[-t/\tau_i]) \cdot E_i \tau_i \dot{\varepsilon} & t \le t_0 \\ E_\infty \varepsilon_0 + \sum_{i=1}^{N} \exp[-(t - t_0)/\tau_i] \cdot (1 - \exp[-t_0/\tau_i]) \cdot E_i \tau_i \dot{\varepsilon} & t > t_0 \end{cases}. \tag{4.4}$$

An alternative representation of the solution is the following:

$$\sigma(t) = \int_0^t E(t-s) \cdot \dot{\varepsilon}(s) \mathrm{d}s, \tag{4.5}$$

where the time-dependent elastic modulus is expressed using the Prony series representation as

$$E(t) = E_\infty + \sum_{i=1}^{N} E_i \cdot \exp[-t/\tau_i]. \tag{4.6}$$

The instantaneous model response was characterized by the instantaneous elastic modulus $E_0 = E(0) = E_\infty + \sum_{i=1}^{N} E_i$. Consequently, the one-dimensional Nth-order generalized Maxwell model contains $2N$+1 material parameters, which were obtained by minimizing the error between the model prediction and the experimental data. This error can be measured by the square root of the mean of the squares of deviations as follows:

$$Q = \sqrt{\frac{1}{m}\sum_{k=1}^{m}\left(\sigma_k^{exp} - \sigma_k^{sim}\right)^2}, \tag{4.7}$$

where m is the number of data points. σ_k^{exp} is the experimental stress value, whereas σ_k^{sim} denotes the model prediction. Once the material parameters were obtained, one can express the storage and loss moduli with the parameters of the model as

$$E'(\omega) = E_\infty + \sum_{i=1}^{N} \frac{\tau_i^2\omega^2}{\tau_i^2\omega^2 + 1} e_i, \quad E''(\omega) = \sum_{i=1}^{N} \frac{\tau_i\omega}{\tau_i^2\omega^2 + 1} e_i, \tag{4.8}$$

where the relative moduli are expressed as $e_i = E_i/E_0$. The dimensionless quantity $\tan\delta$ is defined as the ratio of the loss and storage moduli as $\tan\delta = E''/E'$. This quantity provides information about the relative degree of damping of the material and energy dissipation

4.3 Results

4.3.1 Stress Relaxation Experiments

Native threads, strained under native seawater conditions (pH ~8), experienced average stress relaxation of ~ 40%. To assess the effect of pH on stress relaxation, the relaxation percentage was calculated (at t = 5 min) for threads incubated in buffers pH = 5.5, 6.5, and 7.5. Relaxation results are shown in Table 4.2. Significance was assessed using a pairwise Student's t-test for the various treatment conditions ($p<.05$). A full accounting of the statistical analysis of these data is provided in Table 4.3. Although collagen and the silk-like domains are quite resistant to moderate pH changes [26], the same cannot be said of the His-rich domain. The pK_a of histidine's imidazolium containing side chain (~6.5) results in two discrete protonation states within the range of biologically relevant pH [27]. This leads us to deduce that at pH 5.5 approximately 90% of the histidine residues are protonated thus interfering with its ability to form metal coordinate bonds [2]. At pH 7.5, the histidine residues are largely deprotonated (91%), thus permitting the formation of reversible coordinate bonds to transition metals. When compared with pristine threads, threads treated at pH 7.5 showed no statistical difference in total relaxation: ~40%. Conversely, threads incubated at pH 6.5 and 5.5, corresponding to pH at or below the pK_a of histidine, respectively, experienced ~50% relaxation.

.

Table 4.2: Results for stress relaxation percentage after 5 minutes, the relaxation percentage was determined as described by equation 1. The average and standard deviation are presented for all conditions. Sample size varied between 4 and 12 samples.

Condition	Average Relaxation [R %]
Native	38.8 ± 4.8
pH 5.5	48 ± 10.4
pH 6.5	48 ± 6.6
pH 7.5	41.7 ± 2.5
EDTA pH 5.5	53.1 ± 10.8
EDTA pH 6.5	50.0 ± 6.36
EDTA pH 7.5	48.5 ± 5.1
Urea pH 5.5	23.4 ± 5.1
Urea pH 6.5	24.9 ± 4.1
Urea pH 7.5	33.6 ± 4.7

Table 4.3: Results of the Student's *t*-test analysis of the relaxation percentage pairs. The *h*-value is binary with 1 indicating statistical significance at the 95% confidence.

Pairs for comparison	*h*-value	*p*-value
Native & pH 5.5	1	.0199
Native & pH 6.5	1	.0026
Native & pH 7.5	0	.1952
EDTA pH 5.5 & pH 5.5	0	.2967
EDTA pH 6.5 & pH 6.5	0	.5951
EDTA pH 7.5 & pH 7.5	1	.0222
Urea pH 5.5 vs. Urea pH 6.5	0	.6327
Native vs. Urea pH 5.5	1	4.25E-5
Native vs. Urea pH 6.5	1	6.47E-5
Native vs. Urea pH 7.5	0	.0603

Chelators were agents used to sequester metal ions *via* coordinate bonds from materials. Chelating agents with a high affinity for metal ions are often able to partially or completely strip metal ions from proteins. To further target the metal coordinate bonds in the His-rich domains, threads were treated with the chelating agent ethylenediaminetetraacetic acid (EDTA) at the equivalent pH values described above. All EDTA-treated samples showed comparable relaxation of ~50%. Samples treated with EDTA at pH 5.5 and 6.5 were not statistically different from samples treated with pH only (Table 4.3). By contrast, samples at

pH = 7.5 with and without EDTA deviated by a statistically appreciable amount with the addition of EDTA increasing relaxation by ~7% to ~50%, resembling that of pH 5.5 and 6.5 treatments.

Although His-rich domains are implicated in mechanical stress response via pH and chelator treatments, the role of silk-like domains cannot be discounted [10]. The silk-like domains were challenged using concentrated urea (~8M). Urea is a chaotropic agent known to destabilize secondary protein structure while having minimal effects on metal-coordination bonds [28–30], thus allowing the silk-like domains to be interrogated independently from the His-rich domains. Unlike samples treated with pH and EDTA, urea treatment resulted in decreased relaxation percentage at all pH values tested. Threads incubated with urea at pH 5.5 and 6.5 experienced total relaxations of 23% and 24%, respectively, a statistically significant difference from pH only treatments (Table 4.3). At pH 7.5, the addition of urea reduced relaxation by 5%, yielding a total relaxation of ~33%. Although lower than native controls, the difference was not statistically significant.

4.3.2 In situ tensile SAXS

Previous tensile *in situ* SAXS measurements of byssal threads pulled to 30-50% strain found shifts in meridional peaks to lower q_m values indicating the molecular spacing between preCol bundles increased [5]. Here, *in situ* SAXS measurements on strained threads were conducted to assess changes in molecular spacing because of the relaxation process. It is important to note that SAXS does not capture individual protein domain unfolding but rather changes in the spacing of stagger between preCol bundles. To avoid non-linearities resulting from yielding in the threads, the strain was held at 10%, well below the yielding regime. A

representative 2D scattering diffraction pattern is shown in Appendix B, Figure B.2. The data shown in Figures 4.3 and 4.4 are in terms of the scattering vector, q_m, which is related to the molecular spacing objects (D-spacing) by the equation: $D = \frac{2\pi}{q}$.

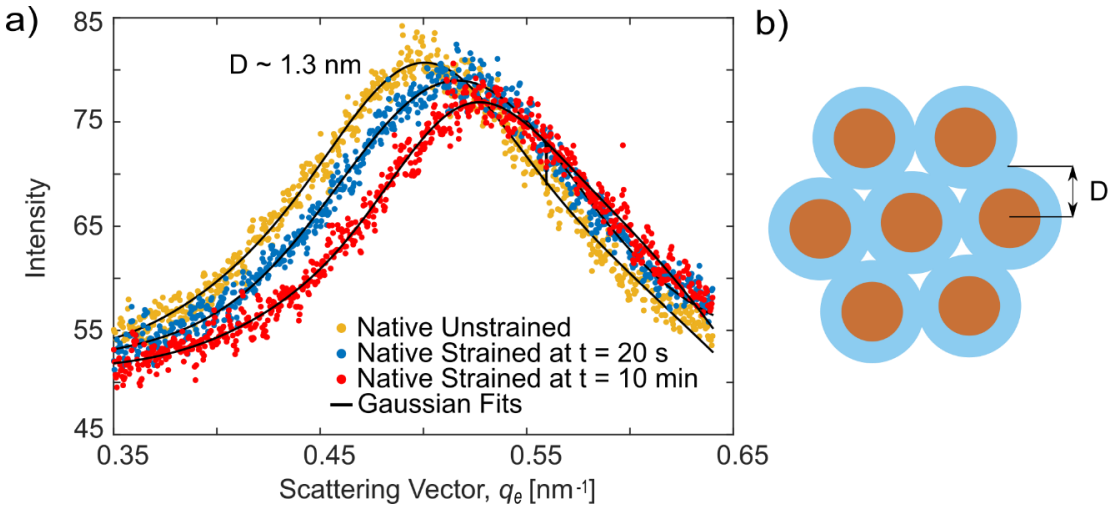

Figure 4.4: SAXS equatorial scattering of mussel distal threads. a) Integration of the peak intensity of the equatorial peaks for a native thread prior to straining, at t = 20 seconds after initial 10% strain, and at t = 10 min with the constant strain of 10% (background was removed). b) Representative hexagonal packing of the preCol 6+1 bundled; D represents the spacing between the center of the collagen domain to the edge of the His-rich and silk domains.

Figure 4.3 shows sharp meridional reflections that arise from the highly aligned and semicrystalline structure the preCols form along the fiber axis. The first peak (at q_m = 0.045) shows a *D*-spacing of ~13.9 nm. The remaining peaks are spaced equally apart by q_m~ 0.045 showing that a spacing of 13.9 nm is repeated. We observed shifts in the meridional peak position upon initial loading that range between 0 to 0.9 nm corresponding to a molecular strain of 0%-6.5% (calculated with Equation 2). EDTA-treated threads exhibited the largest molecular strain (Table 4.4). Importantly, peak position did not exhibit additional changes over time.

The equatorial peaks reveal information about the lateral packing and straining of the preCols. Previous work by Krauss et. al showed that a number of equatorial peaks correspond to the $\sqrt{3}$ ratio of the D-spacing for an ideal hexagonal lattice and confirmed the proposed 6+1 bundled structures [4]. In our studies, only one peak was visible, most likely due to weak signal. This peak has been assigned to the molecular spacing from the center of the triple-helical collagen domain to the edge of the silk-like + His domains (Figure 4.4). Each preCol can be thought of as having a dumbbell-like structure where the silk-like + His domains are larger in diameter compared with the triple-helical collagen central domain. We observed a shift in the equatorial peak immediately upon loading (Figure 4.4). In contrast to the meridional peaks, the equatorial peak shifted to larger q_e values over time while the thread was held at constant strain. This indicates a decrease in molecular spacing (*D*-spacing) after 5 minutes when compared to t ~1 minute under all conditions. These shifts were most pronounced for EDTA and urea-treated samples (Table 4.5).

Table 4.4: Average axial molecular strain at t = 20 seconds after initial 10 % bulk strain. The molecular strain is determined using equation 2 from scattering vector q_m. The second column shows the average molecular strain with the respective standard deviation. The third column shows the number of samples for which molecular strain (peak shifts) were captured. No further space changes were captured after the initial change at t = 20 seconds. The sample size varied between 2 and 7 per condition.

Condition	Average Molecular Strain [%]	Number of samples with peak shifts
Native	3.65 ± 3.60	4/5
pH 5.5	3.08 ± 4.19	3/7
pH 6.5	2.73 ± 3.86	1/2
pH 7.5	2.62 ± 1.66	3/3
EDTA pH 5.5	5.31 ± 0.55	3/3
EDTA pH 6.5	6.12 ± 1.13	4/4
EDTA pH 7.5	6.51 ± 1.74	4/4
Urea pH 5.5	3.37 ± 4.84	4/5
Urea pH 6.5	2.30 ± 1.61	5/5
Urea pH 7.5	3.26 ± 1.82	3/3

Table 4.5: Average lateral molecular strain at t = 20 seconds and the difference in strain between 20 seconds and 5 minutes. The molecular strain is determined using equation 2 from the scattering vector q_e. The second column shows the average molecular strain with the respective standard deviation at t = 20 seconds. The third column shows the change in strain between t = 20 seconds and t = 5 minutes. The negative sign indicates that the spacing between domains is decreasing. The sample size varied between 2 and 5 per condition.

Condition	Average molecular strain at t = 20 s [%]	Average strain change between t = 20 s & t = 5 min [%]
Native	-4.70 ± 2.11	-1.56 ± 0.23
pH 5.5	-1.49 ± 1.72	-1.13 ± 0.73
pH 6.5	-2.04 ± 0.67	-1.70 ± 1.55
pH 7.5	-1.62 ± 1.57	-0.50 ± 0.70
EDTA pH 5.5	-3.42 ± 0.49	-1.32 ± 0.21
EDTA pH 6.5	-3.49 ± 1.66	-0.47 ± 0.16
EDTA pH 7.5	-3.13 ± .033	-0.99 ± 0.31
Urea pH 5.5	-3.59 ± 1.67	-3.15 ± 1.49
Urea pH 6.5	-3.63 ± 2.53	-3.39 ± 2.22
Urea pH 7.5	-6.52 ± 2.06	-2.59 ± 0.21

4.3.2 Fitting the Generalized Maxwell Model

To build a viscoelastic model describing the material response of distal threads we fit the generalized Maxwell model to our stress relaxation measurements and find that the 5th-order model provides excellent agreement in all cases. Increasing the model order did not improve the model prediction. A representative model fitting is illustrated in Figure 2b) where the gray curve shows the measured stress relaxation, whereas the red curve is the model prediction. One can conclude that the curves overlap one another and are almost indistinguishable. The frequency-dependent storage and loss moduli were determined from the fitted models. Representative results for a native sample are shown in Figure 4.5.

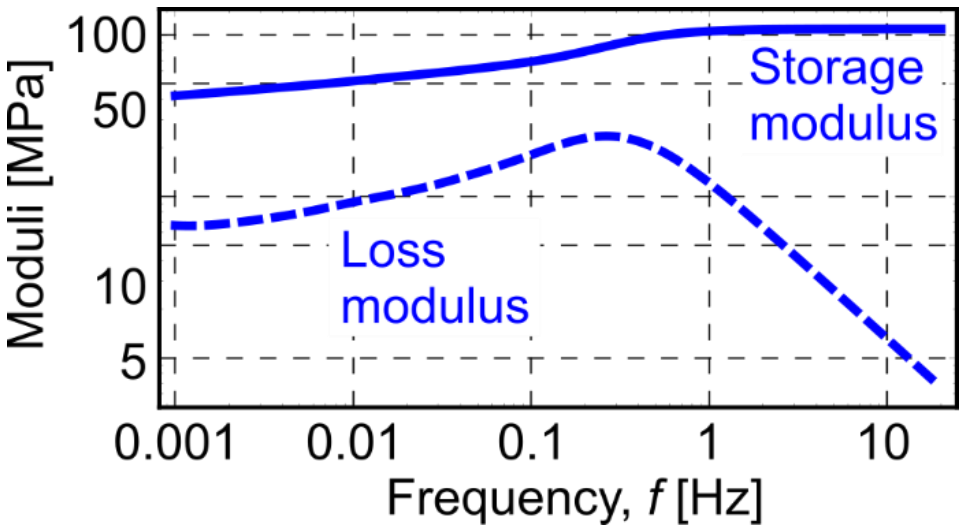

Figure 4.5: Representative storage and loss moduli for a native sample. The loss and storage moduli were modeled using parameters obtained from the generalized Maxwell model. Maximum damping on average was determined to be at ~0.1 Hz.

The frequency values corresponding to the maximum of tan δ were calculated. These values have great importance as they represent the frequency values at which the relative damping of the viscoelastic model is greatest. The results are presented in Figure 4.6. One can observe that the different treatments have a minor effect on the frequency value at which the relative damping is maximal.

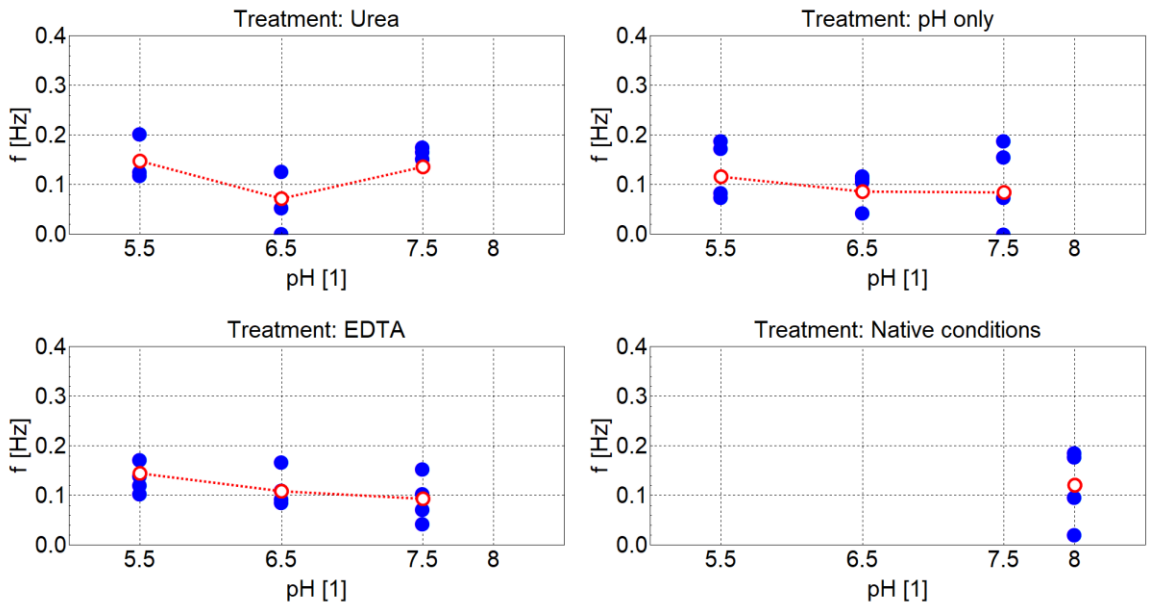

Figure 4.6: The frequency values corresponding to the maximum of $tan\delta$ calculated for all the treatments. Empty red circles show the average values.

4.4 Discussion

The composite structure of the mussel byssus coupled with its unique combination of load-bearing chemistries has served as model systems for bio-inspired materials engineering for decades [31–39]. The goal of this study was to investigate which components in multi-domain preCols dissipate energy via viscous processes. A pristine byssal thread can achieve an impressive 40% stress relaxation on the time scale of minutes. It has been previously demonstrated that when a bulk thread is strained up to 50%, the collagenous domain has a constant maximum molecular strain of merely 2% while the flanking domains extend up to ~150%, this suggests the flanking domains are largely responsible for extending and dissipating strain energy [13,20]. To test this hypothesis, byssal threads were subjected to several chemical treatments aimed at disrupting the two flanking His-rich and silk-like domains, while subsequently stress-relaxation experiments were conducted.

EDTA greatly impacts the His-rich domain but has little effect on the silk-like domain which is devoid of metal coordination complexes [2]. Conversely, urea treatments minimally affect metal coordinate structures and hence have little effect on the His-rich domain [10,30,40]. Although urea can unravel the triple-helical structure of tropocollagens [28], in distal threads the semi-crystalline collagen structure observed in SAXS remained unchanged upon urea addition [41]. When the His-rich domains were compromised via EDTA treatment but the silk-like domains were left intact, the thread experienced the greatest relaxation, hence dissipating the largest amount of energy. Conversely, disruption of the silk-like domains with urea, while leaving the His-rich domains untouched, produced threads capable of reducing very little stress by comparison. This indicates that when a byssal thread is held in tension at strains

below the yield point, the silk-like domains contribute most to stress relief. However, given the complexity of byssus biochemistry and composite structure, inferences based on single treatments deserve a healthy measure of caution. Therefore, to gather a further understanding of what is occurring at the molecular level *in situ* tensile SAXS was utilized.

In agreement with previous studies, the SAXS spectra contained two distinct features. First, there is a meridional peak arising from the axial spacing between the C-terminus of one collagen domain to the adjacent collagen's N- terminus. Thus, this space is occupied primarily by a small part of the collagen and the less-ordered silk-like and His-rich domains [5]. Straining a native thread to 10% led to a molecular strain of approximately 3%. As threads were held at a constant strain, no shifts were observed beyond the initial peak shift indicating the molecular spacing does not change over time. The most notable results when analyzing meridional features were that threads treated with EDTA showed the highest molecular strains ~6%, two times that of the other conditions. Removal of the metal-coordinate complexes via EDTA treatment rendered the His-rich domains non-loadbearing. Instead, the load was immediately transferred to the silk-like domains following modest collagen extension [13]. As a result, the hydrogen bonds and hydrophobic interactions are ruptured as the silk-like domains undergo partial unfolding and extension. This provides the increased molecular strain that accompanies EDTA treatment [42,43]. This behavior has been captured by many other studies in which the β-sheets in silk fibers will orient and stretch, allowing the macromolecular chains to form interlocking regions that transfer loads between chains [44–48]. Conversely, His-metal complexes possess similar bonding energies as covalent interactions [49,50]; therefore, when

loaded, the His-rich domains are able to resist deformation, resulting in lower molecular strains as observed in native threads and threads treated with urea.

Second, a single broad equatorial peak assigned as the spacing from the center of the collagen domain to the edge of the flanking region [5] is observed with SAXS (Figure 4.4). Our data show that although axial spacing between preCols increased upon initial loading, the lateral molecular spacing decreased. This effect was most pronounced for urea-treated threads with initial strains as high as -6.5%. Unlike the axial molecular spacing, this feature continued to decrease during stress relaxation for each condition. We suggest this arises from the rearrangement of the silk-like domains. As the silk-like domains unfold, they can reorient themselves to facilitate closer packing of the preCols. This effect was more pronounced when the system is treated with urea, likely due to the disruption of the silk-like domains.

Based on these data, we propose that relaxation in the core of the thread is largely due to molecular rearrangement in the flanking domains, primarily the silk-like domains. Upon loading, the load is transferred from the His-rich domains to the silk-like domains, whereupon the silk domains begin to extend and/or reorient to relieve local stress over time. This would then require the His-rich domains to contract in order to maintain the observed constant axial spacing. Thus, reorientation and/or molecular movement is responsible for energy dissipation during stress relaxation, similar to that of a viscous damper [25].

Our generalized Maxwell model accurately represents the relaxation behavior of a byssal thread and allows us to further investigate the threads' viscoelastic properties. Even though nonlinear models have been developed describing the viscoelastic effects in

biomaterials and other soft materials, a linear model was used as the strains at which experiments were conducted are well within the elastic regime of the threads [51,52]. Extraction of $\tan\delta$ from the constitutive model indicates maximum energy dissipation (or viscoelastic damping) occurs at ~0.1Hz (Figure 4.6). This is particularly interesting because a 22-year study of near-coast Santa Barbara and Ventura County wave statistics determined an average swell period of 11.01 seconds, or a frequency of 0.09Hz [53]. This makes the byssal thread precisely engineered to cope with ambient environmental stresses. Previous work by Carrington *et al.* showed a different trend suggesting that $\tan\delta$ increased with the oscillation frequency [24]. However, this disagreement is not surprising as our experimental approach was significantly different: our threads were not preconditioned; moreover, their loads were greater by an order of magnitude.

While we used the generalized Maxwell model to fit to the stress relaxation of the entire distal thread, the springs and dashpots also translate to the molecular components in the thread, *e.g.*, the triple helix collagen behaves like a stiff spring that responds to the instantaneous load via extension of no more than 2%[13,20]. Similarly, the His-rich and silk-like domains behave as a spring and dashpot in series (Maxwell elements), with the His-rich domain extending upon initial loading just like a spring and over time the silk-like domains rearrange, behaving more like a damper and allowing the His-rich domain to contract. Although the proposed mechanism accounts for Maxwell elements in series it is unclear as to what element behaves as the spring in parallel with these elements. One possibility is that the entire core behaves as a series of Maxwell elements while the outer stiff cuticle, known to have a modulus 10 times that of the core [19], behaves as a spring in parallel with those elements, thus providing the long term

elastic component. Although there are no known mechanics studies of the matrix proteins, they do exist as a discrete component in the system and could also be contributing to the long term elasticity in the threads [54].

4.5 References

[1] Carrington, E., Waite, J. H., Sarà, G., and Sebens, K. P., 2015, "Mussels as a Model System for Integrative Ecomechanics," Annual Review of Marine Science, **7**(1), pp. 443–469.

[2] Harrington, M. J., and Waite, J. H., 2007, "Holdfast Heroics: Comparing the Molecular and Mechanical Properties of Mytilus Californianus Byssal Threads," Journal of Experimental Biology, **210**(24), pp. 4307–4318.

[3] Waite, J. H., 1992, "The Formation of Mussel Byssus: Anatomy of a Natural Manufacturing Process," *Structure, Cellular Synthesis and Assembly of Biopolymers*, S.T. Case, ed., Springer, Berlin, Heidelberg, pp. 27–54.

[4] Hassenkam, T., Gutsmann, T., Hansma, P., Sagert, J., and Waite, J. H., 2004, "Giant Bent-Core Mesogens in the Thread Forming Process of Marine Mussels," Biomacromolecules, **5**(4), pp. 1351–1355.

[5] Krauss, S., Metzger, T. H., Fratzl, P., and Harrington, M. J., 2013, "Self-Repair of a Biological Fiber Guided by an Ordered Elastic Framework," Biomacromolecules, **14**(5), pp. 1520–1528.

[6] Waite, J. H., Qin, X.-X., and Coyne, K. J., 1998, "The Peculiar Collagens of Mussel Byssus," Matrix Biology, **17**(2), pp. 93–106.

[7] Aldred, N., Wills, T., Williams, D. N., and Clare, A. S., 2007, "Tensile and Dynamic Mechanical Analysis of the Distal Portion of Mussel (Mytilus Edulis) Byssal Threads," J R Soc Interface, **4**(17), pp. 1159–1167.

[8] Bell, E., and Gosline, J., 1996, "Mechanical Design of Mussel Byssus: Material Yield Enhances Attachment Strength," Journal of Experimental Biology, **199**(4), pp. 1005–1017.

[9] Smeathers, J. E., and Vincent, J. F. V., 1979, "Mechanical Properties of Mussel Byssus Threads," Journal of Molluscan Studies, **45**(2), pp. 219–230.

[10] Vaccaro, E., and Waite, J. H., 2001, "Yield and Post-Yield Behavior of Mussel Byssal Thread: A Self-Healing Biomolecular Material," Biomacromolecules, **2**(3), pp. 906–911.

[11] Gosline, J. M., 2018, *Mechanical Design of Structural Materials in Animals*, Princeton University Press.

[12] Arnold, A. A., Byette, F., Séguin-Heine, M.-O., LeBlanc, A., Sleno, L., Tremblay, R., Pellerin, C., and Marcotte, I., 2013, "Solid-State NMR Structure Determination of Whole Anchoring Threads from the Blue Mussel Mytilus Edulis," Biomacromolecules, **14**(1), pp. 132–141.

[13] Hagenau, A., Papadopoulos, P., Kremer, F., and Scheibel, T., 2011, "Mussel Collagen Molecules with Silk-like Domains as Load-Bearing Elements in Distal Byssal Threads," Journal of Structural Biology, **175**(3), pp. 339–347.

[14] Bertoldi, K., and Boyce, M. C., 2007, "Mechanics of the Hysteretic Large Strain Behavior of Mussel Byssus Threads," J Mater Sci, **42**(21), pp. 8943–8956.

[15] Hagenau, A., Scheidt, H. A., Serpell, L., Huster, D., and Scheibel, T., 2009, "Structural Analysis of Proteinaceous Components in Byssal Threads of the Mussel Mytilus Galloprovincialis," Macromolecular Bioscience, **9**(2), pp. 162–168.

[16] Brown, C. H., 1952, "Some Structural Proteins of Mytilus Edulis," Journal of Cell Science, **s3-93**(24), pp. 487–502.
[17] Holten-Andersen, N., and Waite, J. H., 2008, "Mussel-Designed Protective Coatings for Compliant Substrates," J Dent Res, **87**(8), pp. 701–709.
[18] Monnier, C. A., DeMartini, D. G., and Waite, J. H., 2018, "Intertidal Exposure Favors the Soft-Studded Armor of Adaptive Mussel Coatings," Nat Commun, **9**(1), pp. 1–9.
[19] Valois, E., Hoffman, C., Demartini, D. G., and Waite, J. H., 2019, "The Thiol-Rich Interlayer in the Shell/Core Architecture of Mussel Byssal Threads," Langmuir, **35**(48), pp. 15985–15991.
[20] Harrington, M. J., Gupta, H. S., Fratzl, P., and Waite, J. H., 2009, "Collagen Insulated from Tensile Damage by Domains That Unfold Reversibly: In Situ X-Ray Investigation of Mechanical Yield and Damage Repair in the Mussel Byssus," Journal of Structural Biology, **167**(1), pp. 47–54.
[21] Bailey, A. J., Macmillan, J., Shrewry, P. R., Tatham, A. S., Waite, J. H., Vaccaro, E., Sun, C., and Lucas, J. M., 2002, "Elastomeric Gradients: A Hedge against Stress Concentration in Marine Holdfasts?," Philosophical Transactions of the Royal Society of London. Series B: Biological Sciences, **357**(1418), pp. 143–153.
[22] Pearce, T., and LaBarbera, M., 2009, "A Comparative Study of the Mechanical Properties of Mytilid Byssal Threads," Journal of Experimental Biology, **212**(10), pp. 1442–1448.
[23] Cohen, N., Waite, J. H., McMeeking, R. M., and Valentine, M. T., 2019, "Force Distribution and Multiscale Mechanics in the Mussel Byssus," Philosophical Transactions of the Royal Society B: Biological Sciences, **374**(1784), p. 20190202.
[24] Carrington, E., and Gosline, J. M., 2004, "Mechanical Design of Mussel Byssus: Load Cycle and Strain Rate Dependence," Am. Malacol. Bull., **18**.
[25] Lakes, R., and Lakes, R. S., 2009, *Viscoelastic Materials*, Cambridge University Press.
[26] Holmgren, S. K., Bretscher, L. E., Taylor, K. M., and Raines, R. T., 1999, "A Hyperstable Collagen Mimic," Chemistry & Biology, **6**(2), pp. 63–70.
[27] Tanokura, M., Tasumi, M., and Miyazawa, T., 1976, "1H Nuclear Magnetic Resonance Studies of Histidine-Containing Di- and Tripeptides. Estimation of the Effects of Charged Groups on the PKa Value of the Imidazole Ring," Biopolymers, **15**(2), pp. 393–401.
[28] Bennion, B. J., and Daggett, V., 2003, "The Molecular Basis for the Chemical Denaturation of Proteins by Urea," PNAS, **100**(9), pp. 5142–5147.
[29] Canchi, D. R., Paschek, D., and García, A. E., 2010, "Equilibrium Study of Protein Denaturation by Urea," J. Am. Chem. Soc., **132**(7), pp. 2338–2344.
[30] Stumpe, M. C., and Grubmüller, H., 2007, "Interaction of Urea with Amino Acids: Implications for Urea-Induced Protein Denaturation," J. Am. Chem. Soc., **129**(51), pp. 16126–16131.
[31] Barrett, D. G., Fullenkamp, D. E., He, L., Holten-Andersen, N., Lee, K. Y. C., and Messersmith, P. B., 2013, "PH-Based Regulation of Hydrogel Mechanical Properties Through Mussel-Inspired Chemistry and Processing," Advanced Functional Materials, **23**(9), pp. 1111–1119.

[32] Fullenkamp, D. E., He, L., Barrett, D. G., Burghardt, W. R., and Messersmith, P. B., 2013, "Mussel-Inspired Histidine-Based Transient Network Metal Coordination Hydrogels," Macromolecules, **46**(3), pp. 1167–1174.
[33] Holten-Andersen, N., Harrington, M. J., Birkedal, H., Lee, B. P., Messersmith, P. B., Lee, K. Y. C., and Waite, J. H., 2011, "PH-Induced Metal-Ligand Cross-Links Inspired by Mussel Yield Self-Healing Polymer Networks with near-Covalent Elastic Moduli," PNAS, **108**(7), pp. 2651–2655.
[34] Lee, B. P., Messersmith, P. B., Israelachvili, J. N., and Waite, J. H., 2011, "Mussel-Inspired Adhesives and Coatings," Annual Review of Materials Research, **41**(1), pp. 99–132.
[35] Lee, H., Lee, B. P., and Messersmith, P. B., 2007, "A Reversible Wet/Dry Adhesive Inspired by Mussels and Geckos," Nature, **448**(7151), pp. 338–341.
[36] North, M. A., Del Grosso, C. A., and Wilker, J. J., 2017, "High Strength Underwater Bonding with Polymer Mimics of Mussel Adhesive Proteins," ACS Appl. Mater. Interfaces, **9**(8), pp. 7866–7872.
[37] Waite, J. H., Andersen, N. H., Jewhurst, S., and Sun, C., 2005, "Mussel Adhesion: Finding the Tricks Worth Mimicking," The Journal of Adhesion, **81**(3–4), pp. 297–317.
[38] Dalsin, J. L., Hu, B.-H., Lee, B. P., and Messersmith, P. B., 2003, "Mussel Adhesive Protein Mimetic Polymers for the Preparation of Nonfouling Surfaces," J Am Chem Soc, **125**(14), pp. 4253–4258.
[39] Lee, B. P., Dalsin, J. L., and Messersmith, P. B., 2002, "Synthesis and Gelation of DOPA-Modified Poly(Ethylene Glycol) Hydrogels," Biomacromolecules, **3**(5), pp. 1038–1047.
[40] Creighton, T. E., 1993, *Proteins: Structures and Molecular Properties*, Macmillan.
[41] Sizeland, H. K., Wells, H. C., Kelly, S. J. R., Edmonds, R. L., Kirby, N. M., Hawley, A., Mudie, S. T., Ryan, T. M., and Haverkamp, R. G., 2017, "The Influence of Water, Lanolin, Urea, Proline, Paraffin and Fatliquor on Collagen D -Spacing in Leather," RSC Advances, **7**(64), pp. 40658–40663.
[42] Keten, S., and Buehler, M. J., 2010, "Nanostructure and Molecular Mechanics of Spider Dragline Silk Protein Assemblies," Journal of The Royal Society Interface, **7**(53), pp. 1709–1721.
[43] Sheu, S.-Y., Yang, D.-Y., Selzle, H. L., and Schlag, E. W., 2003, "Energetics of Hydrogen Bonds in Peptides," PNAS, **100**(22), pp. 12683–12687.
[44] Brockwell, D. J., Paci, E., Zinober, R. C., Beddard, G. S., Olmsted, P. D., Smith, D. A., Perham, R. N., and Radford, S. E., 2003, "Pulling Geometry Defines the Mechanical Resistance of a β-Sheet Protein," Nat Struct Mol Biol, **10**(9), pp. 731–737.
[45] Du, N., Yang, Z., Liu, X. Y., Li, Y., and Xu, H. Y., 2011, "Structural Origin of the Strain-Hardening of Spider Silk," Advanced Functional Materials, **21**(4), pp. 772–778.
[46] Keten, S., Xu, Z., Ihle, B., and Buehler, M. J., 2010, "Nanoconfinement Controls Stiffness, Strength and Mechanical Toughness of β-Sheet Crystals in Silk," Nature Mater, **9**(4), pp. 359–367.
[47] Lefèvre, T., Rousseau, M.-E., and Pézolet, M., 2007, "Protein Secondary Structure and Orientation in Silk as Revealed by Raman Spectromicroscopy," Biophysical Journal, **92**(8), pp. 2885–2895.

[48] Xiao, S., Stacklies, W., Cetinkaya, M., Markert, B., and Gräter, F., 2009, "Mechanical Response of Silk Crystalline Units from Force-Distribution Analysis," Biophysical Journal, **96**(10), pp. 3997–4005.
[49] Degtyar, E., Harrington, M. J., Politi, Y., and Fratzl, P., 2014, "The Mechanical Role of Metal Ions in Biogenic Protein-Based Materials," Angew Chem Int Ed Engl, **53**(45), pp. 12026–12044.
[50] Khare, E., Holten-Andersen, N., and Buehler, M. J., 2021, "Transition-Metal Coordinate Bonds for Bioinspired Macromolecules with Tunable Mechanical Properties," Nat Rev Mater, **6**(5), pp. 421–436.
[51] Xu, Q., Engquist, B., Solaimanian, M., and Yan, K., 2020, "A New Nonlinear Viscoelastic Model and Mathematical Solution of Solids for Improving Prediction Accuracy," Sci Rep, **10**(1), p. 2202.
[52] Zhang, W., Capilnasiu, A., and Nordsletten, D., 2021, "Comparative Analysis of Nonlinear Viscoelastic Models Across Common Biomechanical Experiments," J Elast.
[53] Beyene, A., and Wilson, J. H., 2006, "Comparison of Wave Energy Flux for Northern, Central, and Southern Coast of California Based on Long-Term Statistical Wave Data," Energy, **31**(12), pp. 1856–1869.
[54] Sagert, J., and Waite, J. H., 2009, "Hyperunstable Matrix Proteins in the Byssus of Mytilus Galloprovincialis," Journal of Experimental Biology, **212**(14), pp. 2224–2236.

Chapter 5. Microstructure effects on hysteresis loops observed in distal threads

5.1 Introduction

Highly composite natural biopolymeric materials are often endowed with remarkable properties and understanding the structural-function relationship can lead to the discovery of vital information needed for engineering bioinspired materials. An excellent model system for this kind of study is byssal threads. Byssal threads present incredible structural and biochemical arrangements yielding excellent mechanical properties [1–12]. The study of the structural-function relationship of byssal threads have already yielded a plethora of mussel-inspired materials[13–18,18–22]. Like in many materials with core/shell architectures byssal threads, specifically the distal portion, possess a soft core with a stiff outer coating. The granular outer coating, known as the cuticle, serves as a both a stiff mechanical component, but also a shielding coating protecting the threads from the environment[23]. The cuticle is roughly 5 μm in thickness, while the whole thread diameter is ~150 μm. Many of the mechanical properties of the threads have been attributed to the collagenous core. The core is composed of highly ordered collagenous fibers known as preCols[24].

Measurements of the core-cuticle modulus indicate that the cuticle can be up to 10 times stiffer than the core[23,25]. Although, these studies have expanded our understating of the byssal threads mechanics, many questions remain unanswered. For example, it is still unclear as to how the cuticle and core interact during mechanical loading to yield high extensibility, toughness, and energy dissipative mechanisms. Recent studies have revealed that there is a thiol-rich interlayer between the core and cuticle, suggesting this layer serves as both

a long-lasting redox reservoir as well as a transition possessing mechanical properties intermediate to the core and cuticle (Figure 5.1) [25]. Furthermore, *in-situ* Small Angle X-Ray Scattering (SAXS) measurements conducted during cyclic loading have revealed that the collagenous microstructure undergoes phase transitions during mechanical loading[4,26,27]. It has also been observed that for true strains (ε_{true}) up to 40% the bulk strain of the core correlates on a one-to-one ratio to preCol strain, suggesting most of the strain is captured in the collagenous core.

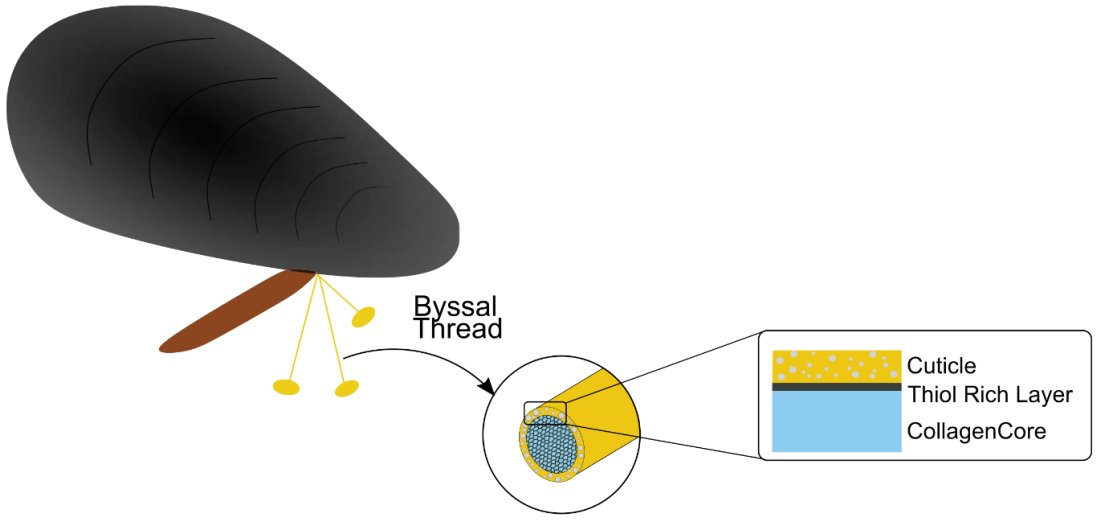

Figure 5.1: Marine distal threads core/shell architecture. The distal thread is composed of a highly ordered collagen core, followed by a thiol rich layer which is then encapsulated by a stiff granular cuticle.

To extend the current understanding of distal thread architecture to mechanical response it is imperative that the behavior of the thread under cyclic loading is further studied. Previous work has shown that the threads exhibit hysteresis of up to 70% when they are loaded and unloaded, meaning they can dissipate large amounts of energy [1]. It has been speculated that energy dissipative mechanism incurred by the thread include breaking and reforming of metal coordinate bonds in the Histidine rich domains found in the preCols [5,6]. Others suggested the silk-like domains found in the preCols break and rearrange during the yield phase to dissipate energy as well [28]. Another unique feature that distal threads exhibit is their ability to mechanically heal on a time scale of hours after incurring mechanical damage[4–6]. This phenomenon means that, if the thread is loaded beyond its elastic regime (the instantaneously recoverable stage) into the yield like regime, and unloaded before failure, the thread will largely recover its prior mechanical properties and subsequently show behavior similar to that of a pristine thread. This is one of the features making the threads such an excellent system for studying, as they can recover their mechanical properties despite being mostly composed of proteins, with no cell-mediation for healing.

To compliment the previous work conducted on distal thread mechanics, we present a study of the cyclic behavior of distal threads accompanied by hyperelastic a neo-Hookean-based model. Experimental data show that during cyclic loading the threads exhibit a Mullins-like effect in which upon unloading the thread undergoes stress softening[29–32]. However, unlike many other materials showing a Mullins behavior, during reloading distal threads experience mechanical recovery and show an increase in modulus upon reloading as compared to the unloading modulus [33–35]. Evidence suggest that during the unloading and reloading

of the threads a phase transition occurs in the collagenous core microstructure [4,27]. In this sense, the thread exhibits a response reminiscent that of shape-memory alloys which are known to undergo phase transitions in their microstructure as a result of temperature changes and due to straining[36,37]. Here, we propose a mechanical model based on previous SAXS studies that elaborates on phase transitions in the core as the threads are cyclically loaded. A neo-Hookean based model which incorporates the mechanical response from two distinct phases is presented as a proof of concept for explaining the mechanical response due to phase transitions in the core. Furthermore, contributions from the cuticle are considered. Lastly, cyclic data from the composite thread are fitted using a 3-Network Yeoh Power Mullins calibrated model.

5.2 Methods

5.2.1 Thread Collection

Mussels *Mytilus californianus* were collected from Goleta Pier near Santa Barbara, CA and stored in maricultural tanks with an open seawater circulation system. Individual mussels were secured onto glass plates with the use of rubber bands overnight, as this prevented the mussels from moving and allowed them to deposit byssus onto the glass surface. Threads were removed within 48 hours of plating and mechanically tested within 72 hours. The proximal region of the threads was removed using a razor blade. Threads were stored in seawater filtered through a 0.22μm filter.

5.2.2 Tensile Testing and Cyclic Testing

Tensile and cyclic loading experiments were conducted on a tabletop tensile tester (Bionix 200 universal testing machine, MTS, Eden Prairie, MN), at nominal strain rates of .4 min^{-1} and .5 min^{-1} respectively. Measurements were conducted using a 10 N load cell and a built-in optical encoder to measure the load and displacement. All mechanical tests were performed with the distal threads fully submerged in seawater inside the Bionix 200 environmental chamber. The two ends of the threads were secured with custom-built clamps and aligned by eye on the tensile tester. Once the threads were secured, initial thread lengths were measured with a digital caliper (ABS Digimatic Caliper, Mitutoyo, Kanagawa, Japan) and recorded. For uniaxial tensile tests, the samples were pulled to failure. Using a different thread, the sample was cycled four different times with an increase of 20% starting with 20% strain and ending at 80% strain with no rest time in between cycles. Force, extension, and time were recorded during the duration of the test.

5.2.3 Data fitting

Cyclic data were fitted using the software MCalibrator (PolymerFEM). The material model for calibration selected was a 3-Yeoh Networks with Power-Law Flow and Mullins softening model, a native Abaqus model (Dassault Systemes Velizy-Vallacoublay, France). This model is a special case of the more general Parallel Rheological Framework (PRF) model. This model was selected as it provided the best fit for the loading paths and incorporates viscoelastic effects.

5.3 Model

Figure 5.2 shows a representative cyclic behavior engineering stress vs. engineering strain curve. Previous studies of the core have correlated a 1 to 1 ratio between the bulk strain and preCol strain for true strains, ε_{true} of up to 40% ($\varepsilon_{engineering}$ ~50%). Assuming the hysteretic behavior observed in the threads is a result of the collagenous core undergoing phase transitions, we consider a hyperelastic model which includes contributions from two distinct phases. In analogy to the terminology for shape-memory alloys, we designate these as an austenitic phase and a martensitic phase.

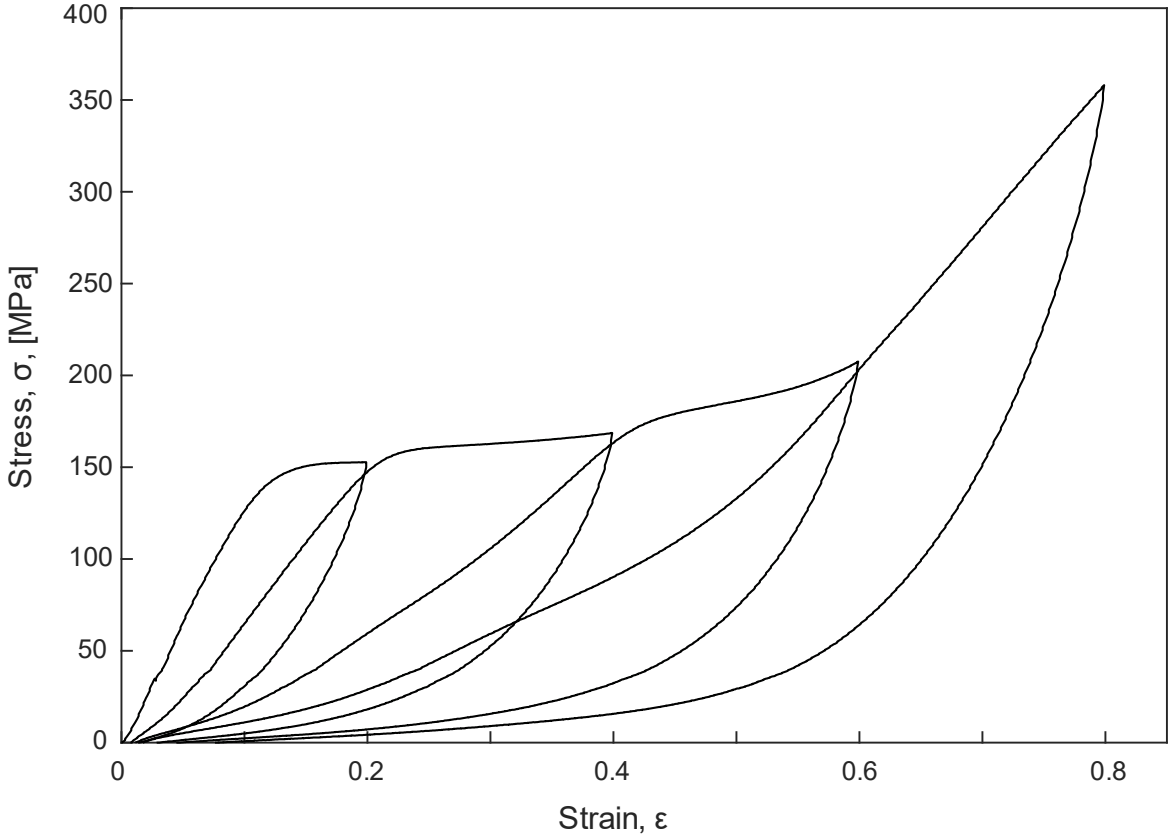

Figure 5.2: Representative cyclic loading response of distal threads. A single thread was loaded four different times starting at zero strain, stretched to 20% then unloaded to zero stress. Loading and unloading cycles were repeated with the maximum strain increased by increments of 20% each time. Cycles were conducted with no wait time in between. Results are presented in terms of engineering stress and strain.

A model in which the austenitic phase is a neo-Hookean material with shear modulus μ_A and the martensitic phase is a different neo-Hookean material with shear modulus μ_M is considered. Since the phases are distinct the shear moduli are selected such that $\mu_M < \mu_A$. It is imposed that both phases experience the same nominal stress, t. In a single phase neo-Hookean material the uniaxial nominal stress is given by (nominal stress):

$$t = \mu\left(\lambda - \frac{1}{\lambda^2}\right) \quad (4.1)$$

where μ is the shear modulus, and λ is the axial stretch ratio. This inverts to provide

$$\lambda = \left[\frac{1}{2} + \left(\frac{t}{3\mu}\right)^3 + \sqrt{\frac{1}{4} + \left(\frac{t}{3\mu}\right)^3}\right]^{\frac{1}{3}} + \left[\frac{1}{2} + \left(\frac{t}{3\mu}\right)^3 - \sqrt{\frac{1}{4} + \left(\frac{t}{3\mu}\right)^3}\right]^{\frac{1}{3}} + \frac{t}{3\mu} \quad (4.2)$$

In general, the material is composed of martensite with volume fraction f and austenite with volume fraction $1 - f$. With the two phases having the same uniaxial nominal stress, the composite stretch ratio is modeled by a rule of mixtures as:

$$\lambda = (1 - f)\lambda_A + f\lambda_M \quad (4.3)$$

where λ_A is the stretch ratio of austenite and λ_M is the stretch ratio of the martensite phase. This leads to

$$\lambda = (1-f)\left\{\left[\frac{1}{2}+\left(\frac{t}{3\mu_A}\right)^3+\sqrt{\frac{1}{4}+\left(\frac{t}{3\mu_A}\right)^3}\right]^{\frac{1}{3}}+\left[\frac{1}{2}+\left(\frac{t}{3\mu_A}\right)^3-\sqrt{\frac{1}{4}+\left(\frac{t}{3\mu_A}\right)^3}\right]^{\frac{1}{3}}+\frac{t}{3\mu_A}\right\}+$$

$$f\left\{\left[\frac{1}{2}+\left(\frac{t}{3\mu_M}\right)^3+\sqrt{\frac{1}{4}+\left(\frac{t}{3\mu_M}\right)^3}\right]^{\frac{1}{3}}+\left[\frac{1}{2}+\left(\frac{t}{3\mu_M}\right)^3-\sqrt{\frac{1}{4}+\left(\frac{t}{3\mu_M}\right)^3}\right]^{\frac{1}{3}}+\frac{t}{3\mu_M}\right\} \quad (4.4)$$

Assuming the shear moduli are such that $\mu_M < \mu_A$ it is then proposed that the martensite will experience a larger strain than the austenite. Starting at zero stress, *i.e.*, at $\lambda = 1$, the material is entirely austenite hence $f = 0$. As the material is loaded and stretched until the stress is equal to a critical value $t = t_M$ the material behaves as neo-Hookean with the shear modulus equal to the austenitic value. When further stretch is imposed, with the critical value $t = t_M$ maintained, f will begin to increase smoothly such that austenite is gradually converted to martensite. Using equation 4.4, a model of the cyclic behavior of a neo-Hookean material with two distinct phases is obtained. All simulations were implemented in MATLAB (Mathworks, Natick, MA).

5.4 Results

5.4.1 Uniaxial and cyclic testing results

To understand the cyclic response of distal threads, it is imperative to first understand the uniaxial tensile response of the threads. Tensile testing of the threads reveal that the threads exhibit a hyperelastic response with three distinct regimes during loading up until failure[1,3,6]. Figure 5.3 shows a representative stress strain curve for a thread that was pulled

to failure. First, an elastic regime is observed where the thread exhibits a linear relationship between the stress and the strain with a modulus of ~ 800 MPa. In this regime, as long as the strain is < 15%, the thread largely behaves in a linear elastic manner. Meaning, if the sample is unloaded and reloaded in this regime it will follow the same curve during the loading. The second stage in Figure 5.3 is a yield like regime, in which large strains are observed accompanied by very little increase in stress. Here, if the sample is unloaded and reloaded the unloading curve will differ from the prior loading curve, as presumably some internal damage has occurred. Lastly, in Figure 5.3 a stiffening regime is observed in which the material once again behaves in a linear manner with a reduction in tangent modulus of about half (~400 MPa) when compared to the initial loading regime.

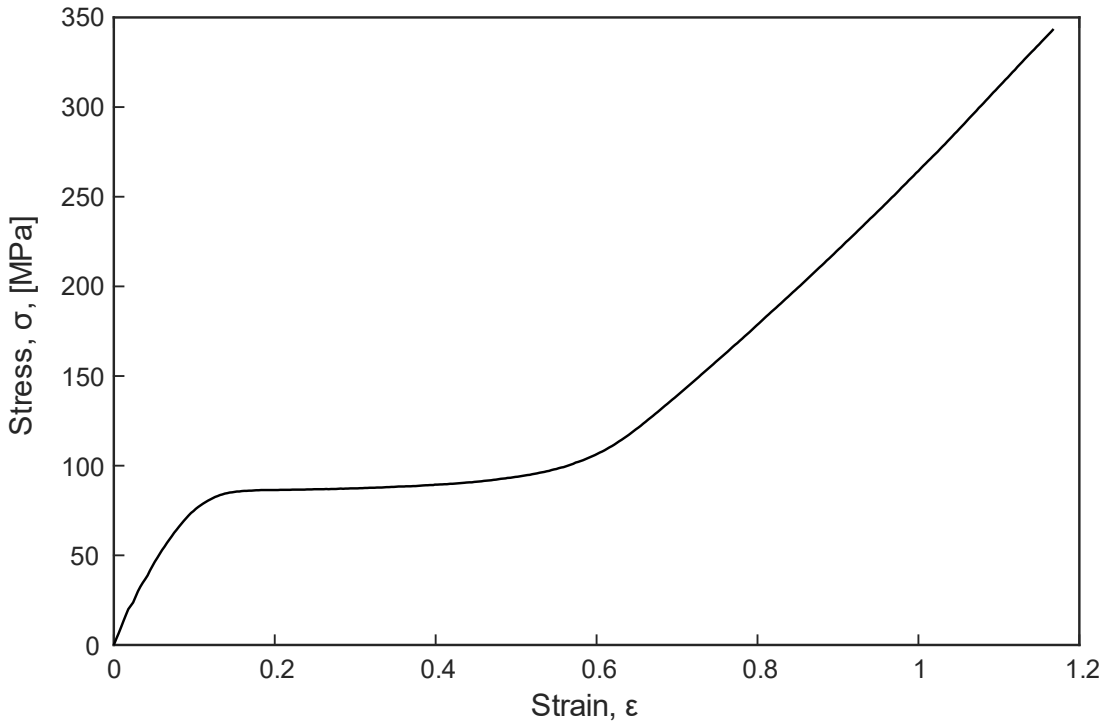

Figure 5.3: Representative tensile loading stress strain curve of mussel distal threads. The stress strain curve exhibits three distinct domains: I) Elastic regime with a modulus of ~800 MPa, II) A yield like regime, III) A linear stiffening regime with a modulus of ~400 MPa. Results are presented in terms of engineering stress and strain.

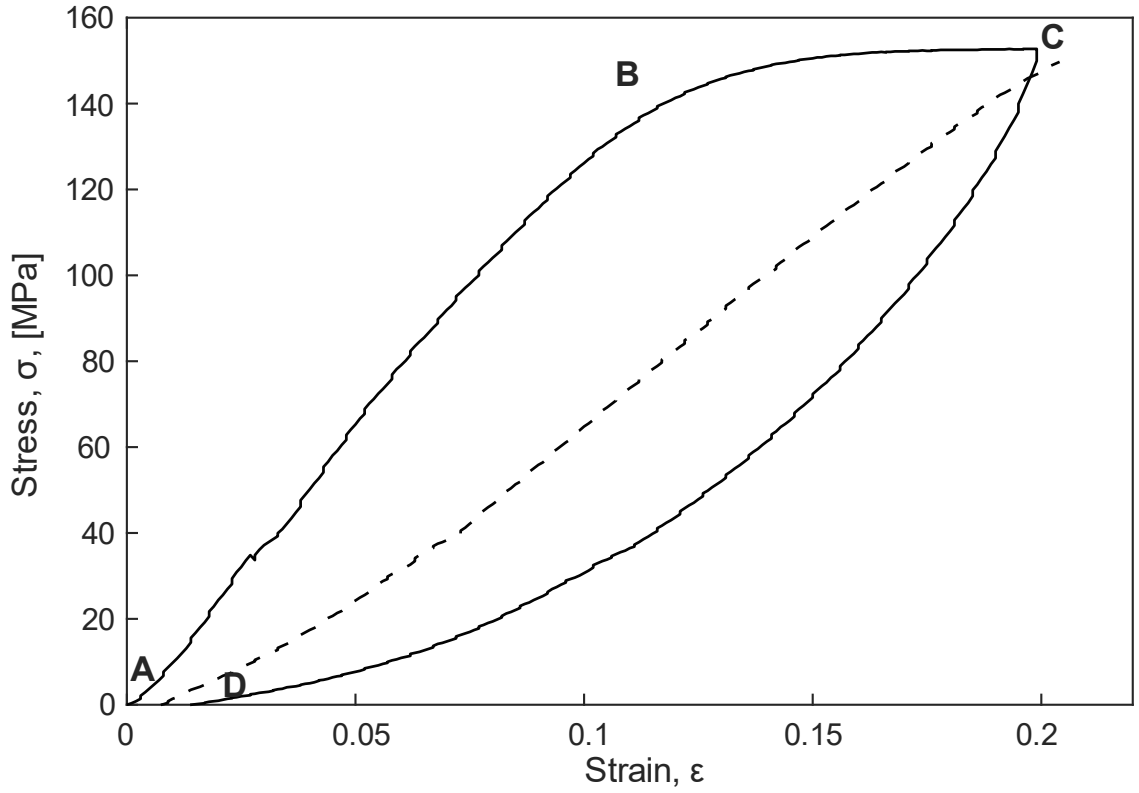

Figure 5.4: Representative hysteresis loop for the first cycle exhibited by distal threads during cyclic loading. The solid line indicates the first loading and unloading cycle. The dashed line indicates the reloading of the thread with no wait time in between the unloading and reloading. The thread exhibits four different stages: I) A-B the thread largely responds in an linear elastic manner, II) B-C the thread enters a yield-like phase in which very little increase in stress is observed, III) C-D there is a softening (Mullins) effect as the thread is unloaded IV) D-C mechanical recovery is observed as the thread is reloaded. Results are presented in terms of engineering stress and strain.

A single thread was cycled four times with increments of 20% strain per cycle up until 80% engineering strain (Figure 5.2). Under cyclic loading at strains exceeding previous maximum values, distal threads show the same primary loading curve as that from a monotonic uniaxial test. To simplify analysis of the data, we focus on the first cycle accompanied by the loading phase of the second cycle shown in Figure 5.4. During the loading portion of the first cycle a linear regime is observed, in a similar manner to that of a uniaxial test. This is followed by a yield-like regime in which very little increase in stress is observed; however, the strain continues to increase. Upon unloading a softening, or Mullins, effect is observed in which there is a loss in modulus. As the thread is reloaded for a subsequent cycle it is observed that there is an instantaneous recovery in the modulus. This happens on the time scale of seconds, whereas a full recovery in mechanical stiffness would occur on the time scale of hours[6]. To quantify differences between cycles the moduli on the loading curve and the hysteresis were calculated; results are shown in table 5.1. From these data it can be observed that with each subsequent cycle there is an increase in hysteresis (higher energy dissipation) at the cost of modulus. The hysteresis is noted to increase by 30-40 $^{J}/_{cm^3}$ with each cycle, while the modulus roughly decreases by a half with each successive cycle.

Table 5.1: Calculated modulus and hysteresis for a single thread undergoing four cycles of straining. Results presented correspond to the data shown in Figure 5.2. No modulus was calculated for the last cycle as this response was not linear.

Cycle	Modulus (MPa)	Hysteresis ($^{J}/_{cm^3}$)
1	1299	29.39
2	824	56.2
3	418	83.7
4	NA	138

5.4.2 Cyclic data fitting

Due to the similarities in distal thread response to a Mullins like response a 3 Yeoh Networks with Power-Law Flow and Mullins softening model was used for modeling the cyclic behavior. This native Abaqus model incorporates hyperelastic, viscous (flow), and plastic elements along with Mullins damage [38]. Figure 5.5 shows the results of the calibrated model; the R^2 value of the fit was .987.

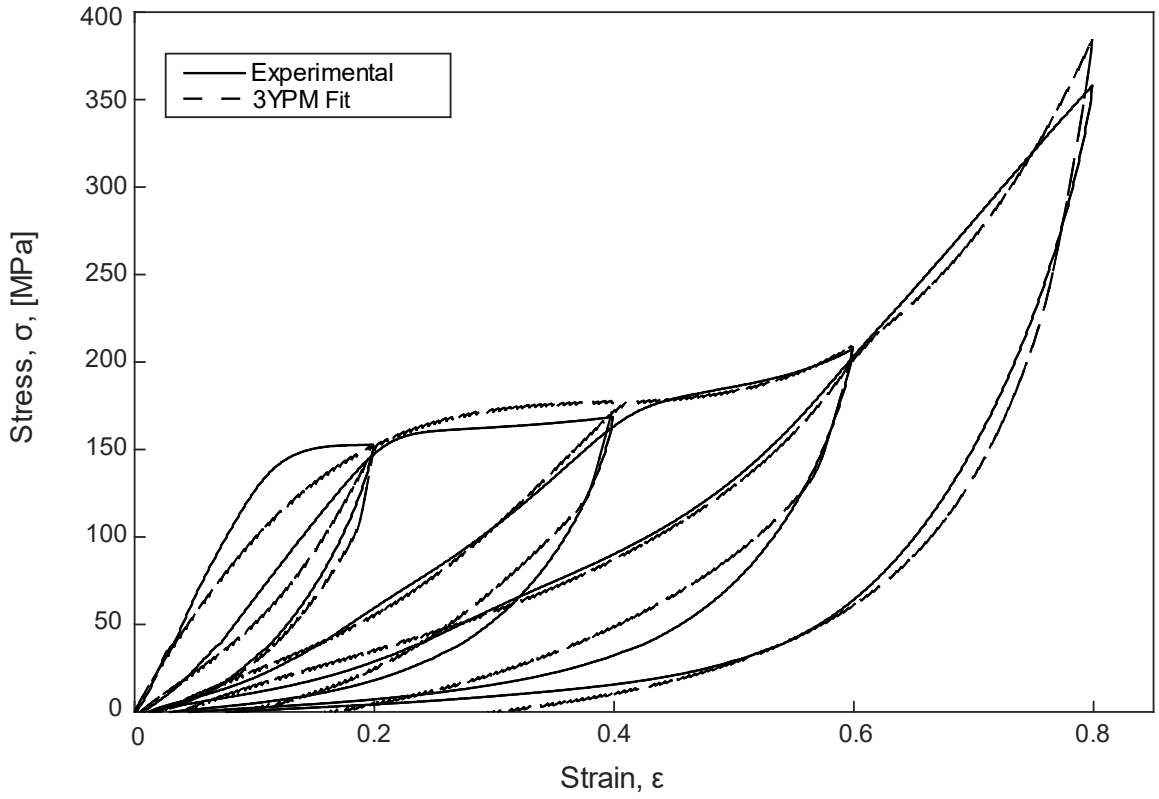

Figure 5.5: Comparison of experimental and predicted results for distal thread cyclic response. The prediction was conducted using the Abaqus 3 Yeoh Networks with Power-Law Flow and Mullins softening material model. The prediction resulted in an R^2 value of .987. Results are presented in terms of engineering stress and strain.

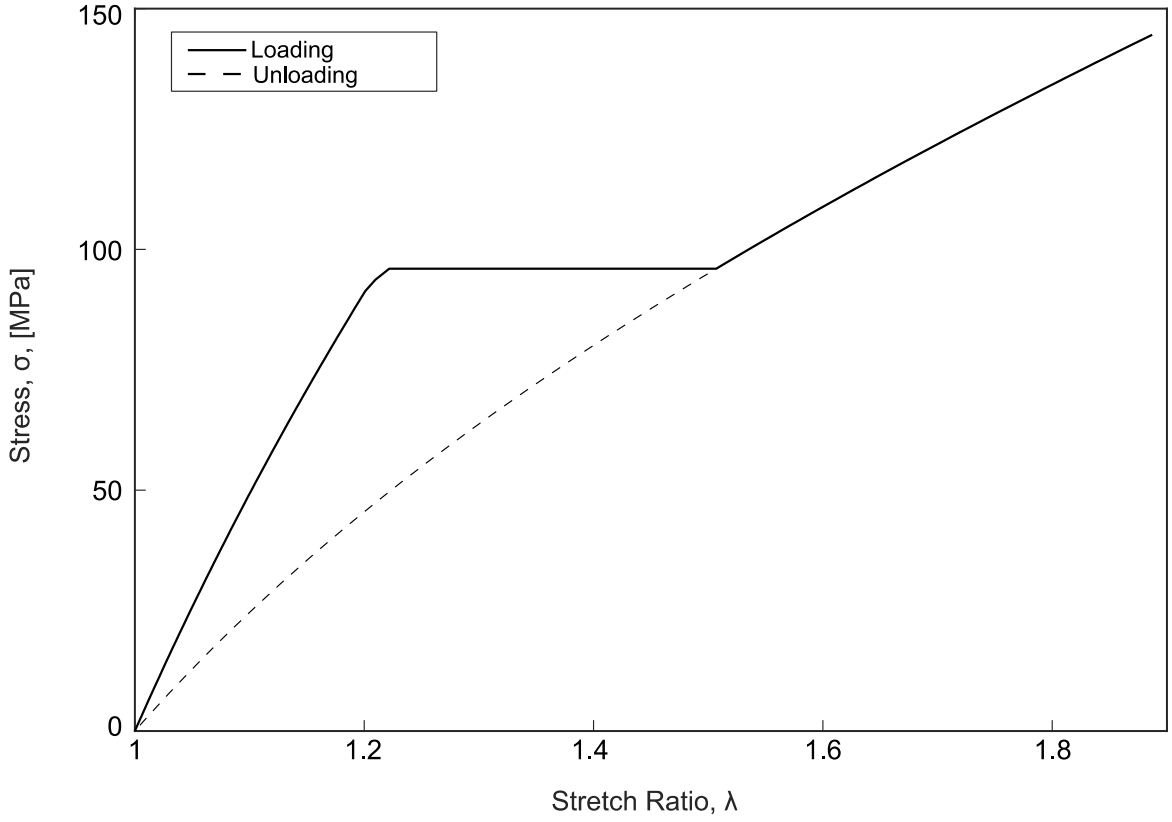

Figure 5.6: Representative hysteresis loop obtained with the neo-Hookean based model. The solid line represents the loading curve with the first stage corresponding to a purely phase II material. At around ~100 MPa the transition between phase I to phase II begins, this is accompanied by no additional stress. During the last stage the microstructure was been completely transformed to phase II.

5.4.3 Model

Figure 5.6 show the cyclic response of a neo-Hookean material with a microstructure that undergoes phase transitions from one phase to another (austenitic → martensitic phase) in response to loading (eq. 4.4). Using shear moduli based on the thread core shear modulus ($\mu_a = \mu_{core}$, $\mu_b = .5\mu_{core}$) a full cycle with unloading is considered. During initial loading, the stress-strain response follows the primary loading curve of a neo-Hookean material with only one phase (i.e. 100% austenitic phase) during the first regime. After the critical stress is reached needed to begin the transition from austenite to martensite, large strain is accommodated with no additional stress. As loading continues it is assumed that the microstructure will continue to transition from austenitic to martensitic phase in a continuous manner. After completing the transition between the phases, the material response will follow the response of a neo-Hookean material with a microstructure made up only phase II. Upon unloading the transition in phases has led to a loss of mechanics, and thus unloading occurs along the same path as loading would occur for a material that has a martensite configuration. It can be observed that as a result hysteresis loops are formed.

5.5 Discussion

Figure 5.2 shows a representative cyclic loading curve obtained for a distal thread. From here it can be observed that the threads exhibit hysteresis loops and undergo softening upon unloading on every cycle, similar to that of a Mullins effect [29–31] . However, the response of the threads differs from a Mullins material in that in that upon reloading for a new cycle, the loading path is distinct from the previous unloading path. The modulus increases as compared to the unloading modulus, showing a recovery in mechanics. For this reason a

strictly Mullins material model did not suffice in predicting material behavior. Here, we used a 3 Yeoh Networks with Power-Law Flow and Mullins softening. This material model showed excellent agreement with experimental results. Although, this model provided a great fit for the composite material response it fails to account for changes in the material microstructure as it is purely phenomenological. Hence, it provides no insight in regard to the source of the mechanical behavior. Previous thread SAXS measurements have shown that there are changes in the thread microstructure with the thread exhibiting two distinct phases in the core microstructure during loading and unloading [4,27].

Krauss et. al demonstrated that when a thread is extended within the elastic regimes ($\varepsilon_{engineering}$ ~15% or, λ ~1.15) one phase in the microstructure is observed (phase I). After the strain exceeds ~15% and the thread enters the yield regime, two distinct SAXS reflections are observed simultaneously corresponding to two microstructure phases, phase I and phase II. Upon reaching a true strain of 40% ($\varepsilon_{engineering}$ ~ 50%) only phase II is observed. It must be noted that the phase II has a SAXS signature that is almost identical to that of phase I.

Although, this study was performed on one cycle it can be used it as a basis for explaining the underlying mechanisms of phase transitions, or structural rearrangement, during cyclic loading in the collagenous core. Using these data, we propose that upon initial loading the thread exhibits the majority of an austenite phase (phase I) in the preCol fibers, and thus a highly linear response. As the thread enters the yield regime the transition between the austenite (phase I) and martensitic (phase II) phase begins, and smoothly transitions up until the austenite phase is completely converted. During this transition, as proposed by Reinecke et. al, the phase transition occurs as a result of metal coordinate bonds breaking/reforming in

the Histidine rich domains as well as extension of the silk-like domains in the preCols. As the thread is unloaded back to its original length, for a single cycle, the silk-like domains recover, enabling them to behave once more as an elastic network [39]. Furthermore, some of the metal coordinate bonds recover, although likely to a different configuration [39]. When the thread is loaded again there is a recovery of phase I and of mechanical stiffness, causing an increase in modulus as compared to the unloading modulus of the previous cycle. This continues to occur for each cycle. Once the full transition from austenite to martensitic has happened, the preCols are completely extended and the load is applied to the polymeric backbone thus pulling on the bonds, this leads to the strain hardening observed in the last regime [40,41].

To account for the microstructural rearrangement occurring in the collagen core, a neo-Hookean base material model with two distinct phases is considered. This model was intended to provide insight into what occurs mechanically as two phases exist in the thread during cyclic loading. By assuming that the ratio between the two phases volume fraction differed during the loading and unloading during a cycle, we were able to predict hysteresis loops (Figure 5.6). The model shows good agreement with the type of behavior observed in the cyclic response of the threads. Although this model serves as an excellent starting point for modeling the hysteresis loops based on two microstructural phases, it lacks the super elastic response exhibited by distal threads. To build on this work, a different hyperelastic model such as a higher order Ogden model may serve to better predict the contributions from the core.

The cuticle has been measured to be up to 10 times stiffer than the core. Using a more conservative estimate of a cuticle stiffness 6 times that of the core, it becomes apparent that the cuticle can bear almost 50% of the total stress carried by the thread. Work by Holten-

Andersen[42] revealed the existence of microcracks in the cuticle. The numbers of cracks in the thread were observed to grow as threads were pulled to higher strains. Taking these findings into account we propose that the cuticle can extend to high strains as a result of microcracks. The microcracks in the system nucleate and grow in density but are non-propagating due to heterogeneous residual stress. The non-propagating microcracks reduce the stiffness of the cuticle, enabling it to strain to significantly high strains without failing in a brittle manner[43,44]. With the cuticle behaving more compliant, there then is a loss in modulus/mechanics that accompanies that of the collagenous core microstructural rearrangement.

5.6 References

[1] Bell, E., and Gosline, J., 1996, "Mechanical Design of Mussel Byssus: Material Yield Enhances Attachment Strength," Journal of Experimental Biology, **199**(4), pp. 1005–1017.

[2] Gosline, J., Lillie, M., Carrington, E., Guerette, P., Ortlepp, C., and Savage, K., 2002, "Elastic Proteins: Biological Roles and Mechanical Properties," Philosophical Transactions of the Royal Society of London. Series B: Biological Sciences, **357**(1418), pp. 121–132.

[3] Carrington, E., and Gosline, J. M., 2004, "Mechanical Design of Mussel Byssus: Load Cycle and Strain Rate Dependence," Am. Malacol. Bull., **18**.

[4] Krauss, S., Metzger, T. H., Fratzl, P., and Harrington, M. J., 2013, "Self-Repair of a Biological Fiber Guided by an Ordered Elastic Framework," Biomacromolecules, **14**(5), pp. 1520–1528.

[5] Harrington, M. J., and Waite, J. H., 2007, "Holdfast Heroics: Comparing the Molecular and Mechanical Properties of Mytilus Californianus Byssal Threads," Journal of Experimental Biology, **210**(24), pp. 4307–4318.

[6] Vaccaro, E., and Waite, J. H., 2001, "Yield and Post-Yield Behavior of Mussel Byssal Thread: A Self-Healing Biomolecular Material," Biomacromolecules, **2**(3), pp. 906–911.

[7] Harrington, M. J., Gupta, H. S., Fratzl, P., and Waite, J. H., 2009, "Collagen Insulated from Tensile Damage by Domains That Unfold Reversibly: In Situ X-Ray Investigation of Mechanical Yield and Damage Repair in the Mussel Byssus," Journal of Structural Biology, **167**(1), pp. 47–54.

[8] Hassenkam, T., Gutsmann, T., Hansma, P., Sagert, J., and Waite, J. H., 2004, "Giant Bent-Core Mesogens in the Thread Forming Process of Marine Mussels," Biomacromolecules, **5**(4), pp. 1351–1355.

[9] Brown, C. H., 1952, "Some Structural Proteins of Mytilus Edulis," Journal of Cell Science, **s3-93**(24), pp. 487–502.

[10] Holten-Andersen, N., Fantner, G. E., Hohlbauch, S., Waite, J. H., and Zok, F. W., 2007, "Protective Coatings on Extensible Biofibres," Nature Mater, **6**(9), pp. 669–672.

[11] Waite, J. H., Qin, X.-X., and Coyne, K. J., 1998, "The Peculiar Collagens of Mussel Byssus," Matrix Biology, **17**(2), pp. 93–106.

[12] Cohen, N., Waite, J. H., McMeeking, R. M., and Valentine, M. T., 2019, "Force Distribution and Multiscale Mechanics in the Mussel Byssus," Philosophical Transactions of the Royal Society B: Biological Sciences, **374**(1784), p. 20190202.

[13] Holten-Andersen, N., and Waite, J. H., 2008, "Mussel-Designed Protective Coatings for Compliant Substrates," J Dent Res, **87**(8), pp. 701–709.

[14] Holten-Andersen, N., Harrington, M. J., Birkedal, H., Lee, B. P., Messersmith, P. B., Lee, K. Y. C., and Waite, J. H., 2011, "PH-Induced Metal-Ligand Cross-Links Inspired by Mussel Yield Self-Healing Polymer Networks with near-Covalent Elastic Moduli," PNAS, **108**(7), pp. 2651–2655.

[15] Fullenkamp, D. E., He, L., Barrett, D. G., Burghardt, W. R., and Messersmith, P. B., 2013, "Mussel-Inspired Histidine-Based Transient Network Metal Coordination Hydrogels," Macromolecules, **46**(3), pp. 1167–1174.
[16] Lee, B. P., Messersmith, P. B., Israelachvili, J. N., and Waite, J. H., 2011, "Mussel-Inspired Adhesives and Coatings," Annual Review of Materials Research, **41**(1), pp. 99–132.
[17] Lee, H., Dellatore, S. M., Miller, W. M., and Messersmith, P. B., 2007, "Mussel-Inspired Surface Chemistry for Multifunctional Coatings," Science, **318**(5849), pp. 426–430.
[18] Krogsgaard, M., Nue, V., and Birkedal, H., 2016, "Mussel-Inspired Materials: Self-Healing through Coordination Chemistry," Chemistry – A European Journal, **22**(3), pp. 844–857.
[19] Zhang, X., Huang, Q., Deng, F., Huang, H., Wan, Q., Liu, M., and Wei, Y., 2017, "Mussel-Inspired Fabrication of Functional Materials and Their Environmental Applications: Progress and Prospects," Applied Materials Today, **7**, pp. 222–238.
[20] Mehdizadeh, M., Weng, H., Gyawali, D., Tang, L., and Yang, J., 2012, "Injectable Citrate-Based Mussel-Inspired Tissue Bioadhesives with High Wet Strength for Sutureless Wound Closure," Biomaterials, **33**(32), pp. 7972–7983.
[21] Li, L., Smitthipong, W., and Zeng, H., 2015, "Mussel-Inspired Hydrogels for Biomedical and Environmental Applications," Polymer Chemistry, **6**(3), pp. 353–358.
[22] Li, C.-H., Wang, C., Keplinger, C., Zuo, J.-L., Jin, L., Sun, Y., Zheng, P., Cao, Y., Lissel, F., Linder, C., You, X.-Z., and Bao, Z., 2016, "A Highly Stretchable Autonomous Self-Healing Elastomer," Nature Chemistry, **8**(6), pp. 618–624.
[23] Holten-Andersen, N., Zhao, H., and Waite, J. H., 2009, "Stiff Coatings on Compliant Biofibers: The Cuticle of Mytilus Californianus Byssal Threads," Biochemistry, **48**(12), pp. 2752–2759.
[24] Coyne, K. J., Qin, X.-X., and Waite, J. H., 1997, "Extensible Collagen in Mussel Byssus: A Natural Block Copolymer," Science, **277**(5333), pp. 1830–1832.
[25] Valois, E., Hoffman, C., Demartini, D. G., and Waite, J. H., 2019, "The Thiol-Rich Interlayer in the Shell/Core Architecture of Mussel Byssal Threads," Langmuir, **35**(48), pp. 15985–15991.
[26] Schmitt, C. N. Z., Politi, Y., Reinecke, A., and Harrington, M. J., 2015, "Role of Sacrificial Protein–Metal Bond Exchange in Mussel Byssal Thread Self-Healing," Biomacromolecules, **16**(9), pp. 2852–2861.
[27] Reinecke, A., Bertinetti, L., Fratzl, P., and Harrington, M. J., 2016, "Cooperative Behavior of a Sacrificial Bond Network and Elastic Framework in Providing Self-Healing Capacity in Mussel Byssal Threads," Journal of Structural Biology, **196**(3), pp. 329–339.
[28] Hagenau, A., Papadopoulos, P., Kremer, F., and Scheibel, T., 2011, "Mussel Collagen Molecules with Silk-like Domains as Load-Bearing Elements in Distal Byssal Threads," Journal of Structural Biology, **175**(3), pp. 339–347.
[29] Mullins, L., 1948, "Effect of Stretching on the Properties of Rubber," Rubber Chemistry and Technology, **21**(2), pp. 281–300.
[30] Mullins, L., 1969, "Softening of Rubber by Deformation," Rubber Chemistry and Technology, **42**(1), pp. 339–362.

[31] Mullins, L., and Tobin, N. R., 1957, "Theoretical Model for the Elastic Behavior of Filler-Reinforced Vulcanized Rubbers," Rubber Chemistry and Technology, **30**(2), pp. 555–571.
[32] Dorfmann, A., and Ogden, R. W., 2003, "A Pseudo-Elastic Model for Loading, Partial Unloading and Reloading of Particle-Reinforced Rubber," International Journal of Solids and Structures, **40**(11), pp. 2699–2714.
[33] Diani, J., Fayolle, B., and Gilormini, P., 2009, "A Review on the Mullins Effect," European Polymer Journal, **45**(3), pp. 601–612.
[34] Peña, E., and Doblaré, M., 2009, "An Anisotropic Pseudo-Elastic Approach for Modelling Mullins Effect in Fibrous Biological Materials," Mechanics Research Communications, **36**(7), pp. 784–790.
[35] Bueche, F., 1960, "Molecular Basis for the Mullins Effect," Journal of Applied Polymer Science, **4**(10), pp. 107–114.
[36] Auricchio, F., and Taylor, R. L., 1997, "Shape-Memory Alloys: Modelling and Numerical Simulations of the Finite-Strain Superelastic Behavior," Computer Methods in Applied Mechanics and Engineering, **143**(1), pp. 175–194.
[37] Duerig, T. W., Melton, K. N., and Stöckel, D., 2013, *Engineering Aspects of Shape Memory Alloys*, Butterworth-Heinemann.
[38] Kocáb, J., Kottner, R., and Kossa, A., 2019, "Characterization of a Cork-Rubber Composite Using Advanced Material Models," Materials Today: Proceedings, **12**, pp. 340–345.
[39] Reinecke, A., Bertinetti, L., Fratzl, P., and Harrington, M. J., 2016, "Cooperative Behavior of a Sacrificial Bond Network and Elastic Framework in Providing Self-Healing Capacity in Mussel Byssal Threads," Journal of Structural Biology, **196**(3), pp. 329–339.
[40] Meyers, M. A., and Chawla, K. K., *Mechanical Behavior of Materials*.
[41] Rubinstein, M., and Colby, R. H., 2003, *Polymer Physics*, OUP Oxford.
[42] Holten-Andersen, N., Fantner, G. E., Hohlbauch, S., Waite, J. H., and Zok, F. W., 2007, "Protective Coatings on Extensible Biofibres," Nature Mater, **6**(9), pp. 669–672.
[43] Budiansky, B., and O'connell, R. J., 1976, "Elastic Moduli of a Cracked Solid," International Journal of Solids and Structures, **12**(2), pp. 81–97.
[44] Charalambides, P. G., and McMeeking, R. M., 1988, "Near-Tip Mechanics of Stress-Induced Microcracking in Brittle Materials," Journal of the American Ceramic Society, **71**(6), pp. 465–472.

Chapter 6. Conclusion

*6.1 O*verview

For centuries mussels abilities to tenaciously attach themselves to surfaces in order to survive, have piqued the interest of humans [1–3]. They endure harsh underwater environments ranging from muddy waters to intertidal zones. Decades of research have revealed that individual fibers in their byssus are highly composite with an architecture spanning length scales from the macroscale to the nanoscale [4–13]. The plaque adheres individual threads to surfaces, while the threads are the elements essential for keeping mussels anchored, despite constant mechanical loading. This dissertation presents four studies dedicated to increasing our understanding of byssal threads and their architectures. I) Geometrical effects on mushroom-shaped structures inspired by mussel byssal threads: This study was intended to build on previous work dedicated to understanding the physical components affecting the adhesion of byssal threads [14]. II) Suction effects on the detachment of structures inspired by byssal threads: This work revealed that at the macroscopic scale vs. microscopic suction becomes an important element on the detachment of mushroom shaped structures. III) Viscoelastic study of distal threads: Here, we explored how protein domains unfold and reorganize to dissipate energy, resulting in stress relaxation. IV) A study of hysteresis loops observed in cyclic loading of distal threads: Lastly, we investigated hysteresis loops observed under cyclic loading of threads, assuming two distinct phases exist during cyclic loading.

6.2 Summary

6.2.1 Geometrical dependencies of mussel inspired adhesion

In this work, we utilized 3D printed molds to replicate geometrically complex structures inspired by mussel byssal threads [15]. Through experiments, we tested how casting and loading angles affect the detachment dynamics of these structures. We demonstrated the relevance of geometry in enhancing adhesion. We found that the optimal configuration for adhesive strength of the synthetic structures was when these structures were cast and pulled along the same angle. This led to defects originating at the center of the tip, thus requiring more energy in order to propagate. Imaging revealed that applying loads at angles other than the casting angle led to changes in the defect propagation at the tip:substrate interface. The changes in loading caused defect origination to shift to off center. It is likely that this caused the lower adhesive detachment forces observed. Furthermore, we explored how the addition of a rounded fillet where the stalk met the tip led to an increase in adhesive strength. This study identified geometrical features which improve the adhesive strength of mussel inspired structures. This work confirmed that mussels often deposit their byssal threads at optimal configurations for adhesive strength. By building on previous work dedicated to understanding the mechanism behind mushroom-shaped structure adhesion, we hope to provide guidance on optimal parameters that can be used for developing new structures that can be used for a range of engineering applications.

6.2.3 Suction-controlled detachment of mushroom-shaped adhesive structures

New insights were presented in this chapter on the contribution of suction to the attachment strength of mushroom-shaped structures [10]. The critical stress required to drive

defect propagation in the presence of trapped air at the interface was obtained as a function of the geometric, material, and interfacial properties of the system. A non-monotonic critical stress in the presence of suction was evidenced in the model and confirmed in experiment by observation of arrest as the defect reaches the flange region. In experiments the reduction in strength in the absence of a suction effect was shown to be ~ 60%, significantly higher than observed in previous studies which have showed effects < 25%. The model presented shows this is primarily the result of the larger width of the flanged tip relative to the stalk. The macroscopic length-scale of the structures, inspired by mussel byssal threads, may play a secondary role associated with a tendency for larger volume change and thus lower pressure in the defect. An asymptotic result for the critical stress in the limit that the defect is far outside of the stalk revealed a regime independent of the toughness of the interface, in which the strength was lowered by a factor of 1/2 than predicted by the balance of remote applied stress and net pressure inside of the defect. This was found to be the result of compressive tractions on the flange outside of the defect, which crucially have not been considered in the literature when approximating the effect of suction.

6.2.4 Viscoelastic analysis of mussel distal threads

This work presented new evidence on the viscoelastic properties of marine mussel byssal threads, and a mechanism for the viscous processes incurred during stress relaxation in the preCols was proposed. Evidently, as the silk-like domains were disrupted via urea treatments, there was a substantial reduction in stress relaxation. This led us to propose that a majority of the energy dissipation occurs in the silk-like domains via molecular rearrangement.

Furthermore, we propose that upon loading the collagen and His-rich domains extend. The load is then transferred from the His-domain to the silk-like domains causing these domains to rearrange and dissipate energy. For this reason, as the His domains were disrupted and no longer participated, the load was transferred directly to the silk-like domains leading to a higher degree of unfolding/rearrangement and hence more relaxation. Our studies were coupled with a 5^{th} order generalized Maxwell model, allowing us to suggest various mechanisms for individual domains. It was observed that across most treatments, maximum damping occurred at around 0.1Hz indicating *Mytilus californianus* distal threads are adaptively fit to withstand and dissipate energy at the same frequency as ambient wave motion [16]. Although this model was developed to describe the viscoelastic properties of mussel threads, the methodology described in this work can be applied to other highly composite biomaterials. This study has provided an alternative narrative to the mechanical response of distal threads incorporating viscoelastic effects.

6.2.5 Microstructure effects on hysteresis loops observed in distal threads

Work conducted on distal threads has largely focused on the mechanical properties of these fibers, with a focus on the elastic properties [17–23]. To supplement this research, the focus of this chapter was on understanding the relationship between the collagenous microstructure and the hysteresis loops observed as result of cyclic loading [18,20,24–30]. Tensile loading, and cyclic loading measurements reveal that threads exhibit three distinct domains in their mechanical response. An elastic regime, followed by a yield regime and lastly a strain hardening response. Based on earlier *in situ* SAXS of distal threads [25], we proposed

that the changes in the mechanical response are due to the transition between two microstructural phases in the collagenous core. A Neo-hookean based model which incorporated the two distinct phases was considered. This model predicted the stress strain relationship for a hysteresis loop assuming a transition between two microstructural phases. Lastly, we also propose that the loss in modulus of the final deformation regime, as compared to the initial elastic regime, is amplified by microcracks in the cuticle, which is estimated to bear half of the total stress in the thread [31]. It has been shown that these microcracks are arrested by granules in the matrix, and thus the non-propagating cracks reduce the stiffness of the cuticle and enable it to strain significantly without failing in a brittle manner [32,33].

6.3 Future Work

The research presented in this dissertation was conducted in an effort to increase our understanding of mussel byssus architecture, and microstructure-mechanical property relationships. The work on mussel inspired mushroom-shaped adhesives revealed the importance of geometry and scale on the adhesive strength of these synthetic structures. To expand our understanding for future work it will be essential to include other architectural components in synthetic structures. For example, the plaque exhibits a highly composite composition with a foam like microstructure [34]. To comprehend the mechanics behind byssal thread adhesion it is imperative this porous architecture be incorporated in the next generation of synthetic structures. Additionally, it would be of great interest to build synthetic structures that incorporate the DOPA adhesive protein which is abundant in the natural system [7,35]. This would allow researchers to test these structures in wet environments.

The thread microstructure to mechanical property relationship in distal threads continues to be an intriguing topic for scientist. Our work, built on many years of previous research, sheds light on the viscoelastic mechanisms employed by distal threads, a topic previously overlooked. Although we now have a better understanding of what occurs in the collagenous core during loading, there are many questions that remain and will need to be addressed in future research. Our results demonstrated that stress relaxation was reduced by treatment by as much as 50%. However, it is still unclear as to where the other sources of relaxation arise from. Possible mechanisms include relaxation in the cuticle and/or the thread matrix proteins [36]. Further studies are needed to dissect the participation of these components in this highly complex biopolymeric material.

Our work dedicated to predicting hysteresis loops in response to cyclic loading serves as an excellent starting point for building a constitutive model describing thread mechanics. It will be of upmost importance to introduce a higher order hyperelastic model, such as those of Ogden [37,38], to extend the initial treatment in this dissertation based on two microstructural phases that incorporates a recovery of mechanical stiffness after unloading. Such a model would more adequately predict the contribution from the core. Lastly, but just as important, will be a model for the relationship between the core and cuticle. The cuticle serves the important role of protecting the core from the environment, while also carrying as much axial load as the core [6,32]. Intermediate to the core and cuticle is a thiol-rich layer that is believed to mediate the contrast in modulus between the core and the cuticle during loading. To construct a constitutive model for the composite thread mechanics it will then be necessary to consider the cuticle mechanical response and the contribution of the thiol-rich layer.

6.4 References

[1] Van Der Feen, P. J., 1949, *Byssus*.

[2] Heide, A. de, 1683, *Anatome Mytuli*.

[3] Brown, C. H., 1952, "Some Structural Proteins of Mytilus Edulis," Journal of Cell Science, **s3-93**(24), pp. 487–502.

[4] Carrington, E., Waite, J. H., Sarà, G., and Sebens, K. P., 2015, "Mussels as a Model System for Integrative Ecomechanics," Annual Review of Marine Science, **7**(1), pp. 443–469.

[5] Holten-Andersen, N., and Waite, J. H., 2008, "Mussel-Designed Protective Coatings for Compliant Substrates," J Dent Res, **87**(8), pp. 701–709.

[6] Valois, E., Hoffman, C., Demartini, D. G., and Waite, J. H., 2019, "The Thiol-Rich Interlayer in the Shell/Core Architecture of Mussel Byssal Threads," Langmuir, **35**(48), pp. 15985–15991.

[7] Lee, B. P., Messersmith, P. B., Israelachvili, J. N., and Waite, J. H., 2011, "Mussel-Inspired Adhesives and Coatings," Annual Review of Materials Research, **41**(1), pp. 99–132.

[8] Waite, J. H., Andersen, N. H., Jewhurst, S., and Sun, C., 2005, "Mussel Adhesion: Finding the Tricks Worth Mimicking," The Journal of Adhesion, **81**(3–4), pp. 297–317.

[9] Dalsin, J. L., Hu, B.-H., Lee, B. P., and Messersmith, P. B., 2003, "Mussel Adhesive Protein Mimetic Polymers for the Preparation of Nonfouling Surfaces," J Am Chem Soc, **125**(14), pp. 4253–4258.

[10] Areyano, M., Booth, J. A., Brouwer, D., Gockowski, L. F., Valentine, M. T., and McMeeking, R. M., 2021, "Suction-Controlled Detachment of Mushroom-Shaped Adhesive Structures," Journal of Applied Mechanics, **88**(3).

[11] Waite, J. H., 2017, "Mussel Adhesion – Essential Footwork," J of Experimental Biology, **220**(4), pp. 517–530.

[12] Gosline, J., Lillie, M., Carrington, E., Guerette, P., Ortlepp, C., and Savage, K., 2002, "Elastic Proteins: Biological Roles and Mechanical Properties," Philosophical Transactions of the Royal Society of London. Series B: Biological Sciences, **357**(1418), pp. 121–132.

[13] Wilhelm, M. H., Filippidi, E., Waite, J. H., and Valentine, M. T., 2017, "Influence of Multi-Cycle Loading on the Structure and Mechanics of Marine Mussel Plaques," Soft Matter, **13**(40), pp. 7381–7388.

[14] Desmond, K. W., Zacchia, N. A., Waite, J. H., and Valentine, M. T., 2015, "Dynamics of Mussel Plaque Detachment," Soft Matter, **11**(34), pp. 6832–6839.

[15] Areyano, M., Gockowski, L., and Valentine, M. T., 2018, "Geometric Control of Adhesion Inspired by Mussel Plaque/Thread Structures," *Proceeding Adhesion Soceity Annual Meeeting*, San Diego, California.

[16] Beyene, A., and Wilson, J. H., 2006, "Comparison of Wave Energy Flux for Northern, Central, and Southern Coast of California Based on Long-Term Statistical Wave Data," Energy, **31**(12), pp. 1856–1869.

[17] Bell, E., and Gosline, J., 1996, "Mechanical Design of Mussel Byssus: Material Yield Enhances Attachment Strength," Journal of Experimental Biology, **199**(4), pp. 1005–1017.
[18] Vaccaro, E., and Waite, J. H., 2001, "Yield and Post-Yield Behavior of Mussel Byssal Thread: A Self-Healing Biomolecular Material," Biomacromolecules, **2**(3), pp. 906–911.
[19] Bailey, A. J., Macmillan, J., Shrewry, P. R., Tatham, A. S., Waite, J. H., Vaccaro, E., Sun, C., and Lucas, J. M., 2002, "Elastomeric Gradients: A Hedge against Stress Concentration in Marine Holdfasts?," Philosophical Transactions of the Royal Society of London. Series B: Biological Sciences, **357**(1418), pp. 143–153.
[20] Harrington, M. J., and Waite, J. H., 2007, "Holdfast Heroics: Comparing the Molecular and Mechanical Properties of Mytilus Californianus Byssal Threads," Journal of Experimental Biology, **210**(24), pp. 4307–4318.
[21] Pearce, T., and LaBarbera, M., 2009, "A Comparative Study of the Mechanical Properties of Mytilid Byssal Threads," Journal of Experimental Biology, **212**(10), pp. 1442–1448.
[22] Smeathers, J. E., and Vincent, J. F. V., 1979, "Mechanical Properties of Mussel Byssus Threads," Journal of Molluscan Studies, **45**(2), pp. 219–230.
[23] Cohen, N., Waite, J. H., McMeeking, R. M., and Valentine, M. T., 2019, "Force Distribution and Multiscale Mechanics in the Mussel Byssus," Philosophical Transactions of the Royal Society B: Biological Sciences, **374**(1784), p. 20190202.
[24] Hassenkam, T., Gutsmann, T., Hansma, P., Sagert, J., and Waite, J. H., 2004, "Giant Bent-Core Mesogens in the Thread Forming Process of Marine Mussels," Biomacromolecules, **5**(4), pp. 1351–1355.
[25] Krauss, S., Metzger, T. H., Fratzl, P., and Harrington, M. J., 2013, "Self-Repair of a Biological Fiber Guided by an Ordered Elastic Framework," Biomacromolecules, **14**(5), pp. 1520–1528.
[26] Arnold, A. A., Byette, F., Séguin-Heine, M.-O., LeBlanc, A., Sleno, L., Tremblay, R., Pellerin, C., and Marcotte, I., 2013, "Solid-State NMR Structure Determination of Whole Anchoring Threads from the Blue Mussel Mytilus Edulis," Biomacromolecules, **14**(1), pp. 132–141.
[27] Hagenau, A., Papadopoulos, P., Kremer, F., and Scheibel, T., 2011, "Mussel Collagen Molecules with Silk-like Domains as Load-Bearing Elements in Distal Byssal Threads," Journal of Structural Biology, **175**(3), pp. 339–347.
[28] Bertoldi, K., and Boyce, M. C., 2007, "Mechanics of the Hysteretic Large Strain Behavior of Mussel Byssus Threads," J Mater Sci, **42**(21), pp. 8943–8956.
[29] Hagenau, A., Scheidt, H. A., Serpell, L., Huster, D., and Scheibel, T., 2009, "Structural Analysis of Proteinaceous Components in Byssal Threads of the Mussel Mytilus Galloprovincialis," Macromolecular Bioscience, **9**(2), pp. 162–168.
[30] Brown, C. H., 1952, "Some Structural Proteins of Mytilus Edulis," Journal of Cell Science, **s3-93**(24), pp. 487–502.
[31] Budiansky, B., and O'connell, R. J., 1976, "Elastic Moduli of a Cracked Solid," International Journal of Solids and Structures, **12**(2), pp. 81–97.

[32] Holten-Andersen, N., Fantner, G. E., Hohlbauch, S., Waite, J. H., and Zok, F. W., 2007, "Protective Coatings on Extensible Biofibres," Nature Mater, **6**(9), pp. 669–672.
[33] Charalambides, P. G., and McMeeking, R. M., 1988, "Near-Tip Mechanics of Stress-Induced Microcracking in Brittle Materials," Journal of the American Ceramic Society, **71**(6), pp. 465–472.
[34] Filippidi, E., DeMartini, D. G., Molina, P. M. de, Danner, E. W., Kim, J., Helgeson, M. E., Waite, J. H., and Valentine, M. T., 2015, "The Microscopic Network Structure of Mussel (Mytilus) Adhesive Plaques," Journal of The Royal Society Interface, **12**(113), p. 20150827.
[35] Waite, J. H., 2002, "Adhesion à La Moule," Integr Comp Biol, **42**(6), pp. 1172–1180.
[36] Sagert, J., and Waite, J. H., 2009, "Hyperunstable Matrix Proteins in the Byssus of Mytilus Galloprovincialis," Journal of Experimental Biology, **212**(14), pp. 2224–2236.
[37] Ogden, R. W., 1997, *Non-Linear Elastic Deformations*, Courier Corporation.
[38] Ogden, R. W., and Hill, R., 1972, "Large Deformation Isotropic Elasticity – on the Correlation of Theory and Experiment for Incompressible Rubberlike Solids," Proceedings of the Royal Society of London. A. Mathematical and Physical Sciences, **326**(1567), pp. 565–584.

Appendix A: Experimental components for bioinspired structure adhesive testing

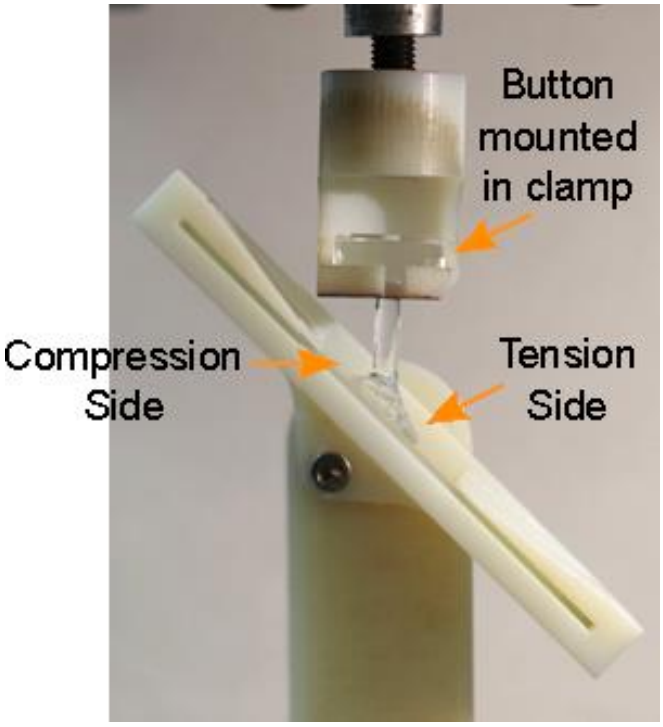

Figure A.1. Custom 3D printed stage which allows for varying pulling angles. Here, loading at 45º is shown.

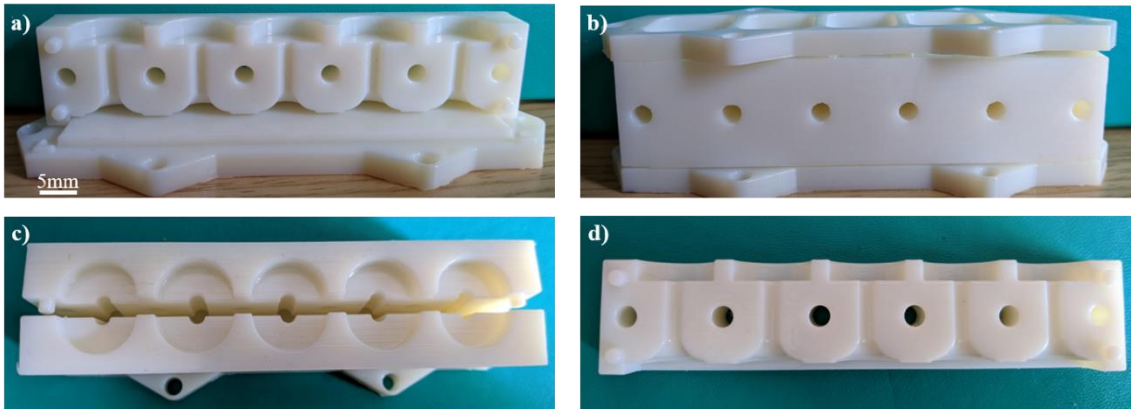

Figure A.2. Custom 3D printed mold used to batch manufacture five mushroom-shaped structures; (a) Bottom piece and one side of the identical halves, showing internal structure; (b) Fully assembled - molds are sealed with screws, washers, and wing nuts; (c) Top view of the molds showing the button region; (d) Side view of one of the identical halves. Angled structures used similar molds with variations in stalk angle.

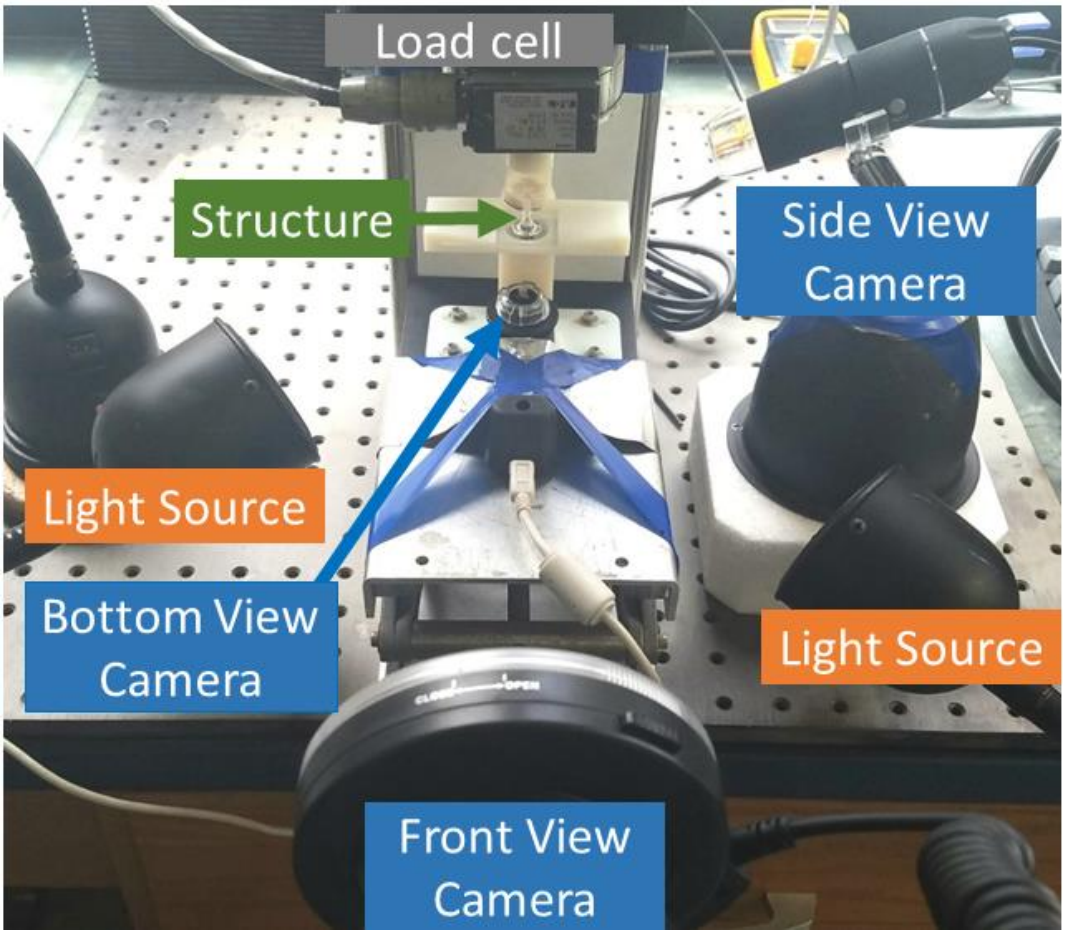

Figure A.3. Image of a tensile testing experimental set up, with a 90°/90° structure loaded. Two lighting sources and three cameras were incorporated to capture the dynamics of deformation of the structure as well as its detachment from the substrate. The printed clamps are screwed into the load cell (at top) and stage (at bottom), and the motor is positioned above the load cell (not in figure).

Appendix B: Experimental set up for Small Angle-X-Ray Scattering (SAXS) measurements

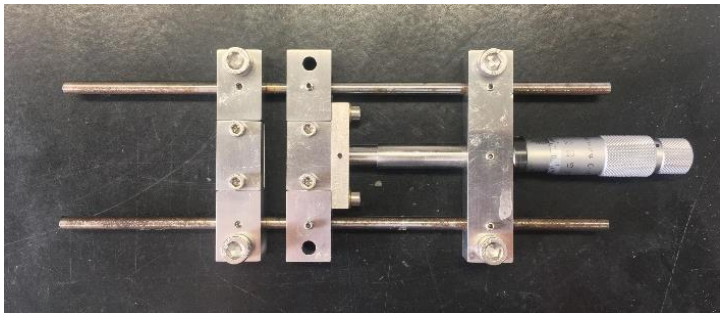

Figure B.1: Hand-held custom-built tensile tester. Samples are held between the two grips, which are tightened by hand with a hex key. Samples are held at a constant strain of 10%, and SAXS measurements are recorded every 20 seconds.